

ABSTRACT

YAO, SHANSHAN. Liquid Breakup and Atomization of Pressure Jet and Swirl Atomizers. (Under the direction of Dr. Tiegang Fang).

Liquid spray and atomization systems are widely used in industrial, commercial, and household applications. For example, pressure jet and swirl atomizer are found in liquid dispensing systems from fuel injectors in large scale power generation engines to small scale liquid sprayers, mainly due to their good atomization characteristics, low costs, and simple geometries. Therefore, it is of practical importance to understand the breakup and atomization processes in these systems.

The liquid-air interaction, surface tension, and viscous forces are the primary factors that govern the liquid breakup processes. The stability of the ejected liquid sheet from swirl atomizers plays an important role in spray development, liquid breakup, and atomization. Liquid properties directly influence the surface stability of liquid sheets, which consequently affects the downstream atomization quality. The effect of fluid viscosity and surface tension on spray structures, cone angle, and breakup length were studied experimentally in this work. High speed visualization was applied to capture the spray images. A MATLAB image processing program was developed to analyze the spray characteristics. The wave frequencies for fluids with a range of different viscosities were calculated by Fast Fourier Transform (FFT) in order to study the temporal wave propagation characteristics. A laser diffraction technique was used to measure the droplet size and its distribution at different locations along the spray developing trajectory. Results show that liquid viscosity plays an important role on the spray primary breakup process. Spray cone angle is found to decrease as the viscosity increases, while the breakup length gives an opposite trend. Fluid surface

tension is not a critical parameter that determines the primary breakup process, but it affects the downstream droplet size and distribution significantly, namely the secondary breakup or atomization process.

Liquid film thickness inside the swirl atomizer nozzle plays an important role in controlling the initial sheet thickness and primary breakup. In order to study the internal flow of swirl atomizers, a transparent swirl atomizer was designed. The liquid film thickness was measured using a high speed camera under different injection pressures. Fluids with different viscosities were applied to study their influences on the film thickness. Results show that higher pressures lead to thinner initial film thickness and as the viscosity increases, film thickness becomes thicker.

In addition, there are many practical processes involving liquid evaporation during the breakup and atomization process. In order to study the effect of evaporation on liquid jet breakup, experiments were conducted using circular and rectangular orifice nozzles under low pressures. Five ambient temperatures and ten injection pressures were used to study the liquid jet breakup length and wavelength on the jet surface. Correlations between non-dimensional number and liquid jet characteristics were developed. This work reveals that the ambient temperature has a strong influence on liquid jet breakup length under low jet velocity conditions. But as the jet velocity increases, its influence becomes weak. The surface wavelength was found in a linear relationship with jet velocity under different ambient temperatures.

In summary, the external and internal characteristics of low pressure jets and sprays were studied in this dissertation. The quantitative measurements contribute valuable

experiment data to support further understanding of the fundamental physical processes of liquid breakup and atomization. The results in this dissertation also provide more accurate initial inputs for spray model validations.

© Copyright 2013 by Shanshan Yao

All Rights Reserved

Liquid Breakup and Atomization of Pressure Jet and Swirl Atomizers

by
Shanshan Yao

A dissertation submitted to the Graduate Faculty of
North Carolina State University
in partial fulfillment of the
requirements for the degree of
Doctor of Philosophy

Mechanical Engineering

Raleigh, North Carolina

2013

APPROVED BY:

Dr. Tiegang Fang
Committee Chair

Dr. Jack Edwards

Dr. William Roberts

Dr. Xiaoning Jiang

DEDICATION

To my parents and my husband, Yu Shi

For their love and encourage

BIOGRAPHY

Shanshan Yao was born in Tianjin, China. As the only child in the family, she was raised with all the love from her parents. In 2003, she left home and went to Huazhong University of Science and Technology in Wuhan, China for her undergraduate study. She received her bachelor degree of engineering in energy and power engineering and a dual bachelor degree of art in English language in 2007 before coming to the NC states for Ph.D. study.

She joined Dr. Tiegang Fang's research group in the Department of Mechanical and Aerospace Engineering in August 2008. Her research projects are focused on liquid spray breakup and atomization. During her Ph.D. study, she designed and developed the experiment systems and studied the spray characteristics experimentally. She has gained a lot of training and experience in the process of solving challenging problems. She also practiced a half year internship with Cummins Emission Solutions in Madison, Wisconsin, where she gained valuable industrial experience.

After graduation, she will work as an engineer in oil industry and apply her knowledge and experience in the new position.

ACKNOWLEDGMENTS

I would like to express my sincere gratitude to my supervisor, Dr. Tiegang Fang, for letting me join his research group in 2008. I very much appreciate his expertise, understanding, and patience on coaching me during my Ph.D. study. Without his guidance and support, my research work would not have been possible.

I would like to express my gratitude to Dr. Xiaoning Jiang , Dr. William Roberts and Dr. Jack Edwards for taking the time to serve in my committee and their advices. I would like to thank Dr. Xiaoning Jiang for allowing me using his ultrasonic equipments to explore the feasibility of measuring the film thickness.

I am grateful to Mr. Rufus Richardson (Skip) and Mr. Rick Lamy for their support during my five years research. They always finished all the machine shop requests within a short time. This research cannot be finished without their help.

I am really glad that I had the opportunity to work with a lot of great people. I would like to thank Dr. Ji Zhang, Wei Jing, and Thomas Powell for their help on my research projects. Ji helped me a lot during my first year in Raleigh. Tommy assisted me on doing the experiment of film thickness measurement. Wei provided a lot of help on building the experiment facility. I really enjoy the time working with them.

Finally, I would to express my sincere appreciation to my parents for the support they have always provided me. Their unconditional love and encouragement support me to get through many difficult times. I must acknowledge my husband, Dr. Yu Shi. Without his love, encouragement, and support, I would not have finished my research and this dissertation.

After five years long-distance relationship and marriage, we will finally reunite and establish family in Oklahoma. I believe there will be a bright new life for us.

This research was supported in part by the MeadWestvaco Corporation, the NC Space Grant, and the Research and Innovation Seed Funding (RISF) Program at NC State University. The help of Mr. Keith Abbott, Mr. Douglas Dobbs, and Dr. Frederick Renk from MeadWestvaco on the setup of the trigger sprayer experiments is also greatly appreciated.

TABLE OF CONTENTS

LIST OF TABLES	x
LIST OF FIGURES	xi
1. INTRODUCTION	1
1.1. Motivation	1
1.2. Research objective and approaches.....	2
2. LITERATURE VIEW	6
2.1. Atomization process.....	6
2.1.1. Swirl atomizer.....	8
2.2. External spray characteristics.....	9
2.2.1. Spray pattern	10
2.2.2. Spray angle.....	10
2.2.3. Breakup length.....	11
2.3. Internal flow characteristics	12
2.3.1. Measurement methods of liquid film thickness	12
2.3.2. Conductance method.....	13
2.3.3. Optical method.....	13
2.3.4. Laser-induced fluorescence/ planar laser-induced fluorescence method.....	15
2.3.5. Ultrasonic methods	17
2.3.6. Capacitance methods	18
2.3.7. Liquid film thickness inside swirl atomizer.....	19
2.4. Droplet size and distribution	21
2.4.1. Measurement methods	22
2.4.2. Representative diameters	25
2.4.3. Mathematical distribution function.....	25
2.5. Instability of liquid jet.....	26
2.6. Instability of liquid sheet.....	28
2.6.1. Inviscid liquid sheet	29
2.6.2. Viscous liquid sheet	30
2.7. Evaporation effect	31

2.7.1. Drop evaporation.....	31
2.7.2. Liquid jet evaporation.....	32
2.8. Summary	37
2.9. Table and figures.....	39
3. EXPERIMENTAL SYSTEM AND METHOD	43
3.1. Optical measurement system.....	43
3.1.1. High speed camera.....	43
3.1.2. Backlit system.....	43
3.2. Data acquisition system.....	44
3.2.1. Sensors	44
3.2.2. Hardware and software configuration.....	44
3.3. Droplet size measurement system	44
3.4. Summary	46
3.5. Tables and figures	47
4. EXPERIMENTAL STUDY ON GLYCEROL-WATER MIXTURES	51
4.1. Introduction	51
4.2. Experimental Setup and Fluid Samples	54
4.2.1. Fluid Samples.....	55
4.3. Sensor data comparison.....	55
4.3.1. Displacement comparison.....	55
4.4. Spray spatial structure	56
4.5. Spray cone angle analysis	58
4.6. Instability of liquid sheet.....	60
4.6.1. Temporal structure comparison	60
4.6.2. Analysis of surface wave frequency	62
4.7. Droplet size distribution.....	64
4.8. Summary	67
4.9. Tables and figures	68
5. EXPERIMENTAL STUDY ON ETHANOL-WATER MIXTURES	99
5.1. Introduction	99
5.2. Experimental system and techniques	100

5.2.1. Experimental setup.....	100
5.2.2. Fluid samples.....	100
5.2.3. Spray visualization.....	101
5.2.4. Transient droplet size measurement.....	102
5.3. Near nozzle spray structure.....	103
5.4. Spray cone angle analysis.....	104
5.5. Breakup length analysis.....	105
5.6. Droplet size measurements.....	106
5.6.1. Percentiles parameter and Sauter Mean Diameter.....	106
5.6.2. Particle size distribution.....	108
5.7. Summary.....	109
5.8. Tables and figures.....	111
6. EXPERIMENT STUDY ON LIQUID FILM THICKNESS.....	124
6.1. Introduction.....	124
6.2. Mathematical equations.....	126
6.3. Experimental setup.....	127
6.3.1. Nozzle structure.....	128
6.3.2. Flow visualization.....	128
6.3.3. Experimental conditions.....	129
6.4. Results and discussions.....	130
6.4.1. Spray characteristics under steady state.....	130
6.4.2. Film thickness under different injection pressures.....	130
6.4.3. Film thickness for different viscosity fluids.....	132
6.4.4. Comparison between analytical equations and experiment.....	133
6.4.5. Effect of fluid properties.....	135
6.5. Summary.....	136
6.6. Tables and figures.....	138
7. EXPERIMENTAL STUDY ON EVAPORATION EFFECTS.....	148
7.1. Introduction.....	148
7.2. Experimental system.....	150
7.2.1. Experimental system setup.....	150
7.2.2. Nozzle Geometry.....	151

7.2.3. Spray visualization.....	151
7.3. Results and discussions	152
7.3.1. Mass flow rates measurement.....	152
7.3.2. Non-dimensional number.....	152
7.3.3. Breakup length analysis	154
7.3.4. Wave length analysis	156
7.4. Summary	157
7.5. Table and figures	159
8. CONCLUSIONS.....	174
8.1. Conclusions	174
8.2. Future work	177
REFERENCES	180

LIST OF TABLES

Table 4.1 The viscosity of glycerol-water fluid mixtures at 23 °C.....	68
Table 4.2 Mean value of the spray cone angles	68
Table 4.3 Specified time period of wave frequency for different fluids.....	69
Table 4.4 Refractive index for different fluid mixtures	69
Table 5.1.Fluid properties for ethanol-water mixtures at 21°C	111
Table 5.2 Average spray cone angles for ethanol-water mixtures.....	112
Table 5.3 Average breakup lengths for ethanol-water mixtures.....	112
Table 5.4 Average SMD over all locations.....	113
Table 6.1. Atomizer specifications	138
Table 6.2. Analytical and empirical equations for the sheet thickness	138
Table 7.1 Classification of jet breakup regimes.....	159
Table 7.2 Geometrical details of the orifices	159
Table 7.3 Physical properties under different temperatures	159
Table 7.4 Reynolds number for different flow conditions.....	160
Table 7.5 Weber number of liquid for different flow conditions	160
Table 7.6 Weber number of air for different flow conditions.....	160

LIST OF FIGURES

Figure 2.1 Schematic of the automated optical film thickness measurement system [30]	39
Figure 2.2 Theoretical schematic of the fluorescent dye technique [31]	39
Figure 2.3 Diagram of a flow loop [33]	40
Figure 2.4 Test section for PLIF measurements [33]	40
Figure 2.5 Schematic of the ultrasonic fluid thickness measurement system [36]	41
Figure 2.6 Schematic of the experimental apparatus for liquid film thickness [43]	41
Figure 2.7 Schematic of the experimental apparatus for evaporation jet analysis [76]	42
Figure 3.1 Standard flood illumination system used for backlit imaging [77]	47
Figure 3.2 Optimized lighting system [77]	47
Figure 3.3 Sensors installed on a trigger sprayer	48
Figure 3.4 Signal conditioning modules and data acquisition system	48
Figure 3.5 LabView interface	49
Figure 3.6 Measurement window of SprayTec software	49
Figure 3.7 Setup of droplet size measurement	50
Figure 3.8. Laser diffraction technology[47]	50
Figure 4.1 Schematic of the experimental setup	70
Figure 4.2 Transient dispensing piston displacements of different glycerol-water mixtures .	71
Figure 4.3 Start stage of spray development for different glycerol-water mixtures	72
Figure 4.4 Developed stage of spray development for different glycerol-water mixtures	73
Figure 4.5 The ending stage of spray development for different glycerol-water mixtures	74
Figure 4.6 Spray structure of highly viscous fluids	75

Figure 4.7 Global spray structure of the trigger spray and the calculated cone angle	75
Figure 4.8 (a)-(d) The image processing steps. (e) Clear surface profiles obtained	76
Figure 4.9 The transient changes of spray angle and mean value over time for 0% to 80% glycerol-water mixtures	77
Figure 4.10 The calculated spray angle and the error bars for glycerol-water mixtures	77
Figure 4.11 An example of spatiotemporal diagram for local frequency analysis	78
Figure 4.12 Spatiotemporal diagram at Location 1 for different fluids at starting, developed, and ending stage from the left to the right	78
Figure 4.13 Spatiotemporal diagram at Location 2 for different fluids at starting, developed, and ending stage from the left to the right	79
Figure 4.14 Spatiotemporal diagram at Location 3 for different fluids at starting, developed, and ending stage from the left to the right	80
Figure 4.15 Spatiotemporal diagram at Location 4 for different fluids at starting, developed, and ending stage from the left to the right	81
Figure 4.16 Discredited locations for surface wave analysis.....	82
Figure 4.17 Developed temporal structure for fluid mixtures with different viscosity	83
Figure 4.18. The spatiotemporal diagrams for different viscosity fluids at Location 6 at different time period	84
Figure 4.19 (a) A typical detected edge on the original image of 70% glycerol at Location 1 with a time period of 394.4~406ms (b) Fast Fourier Transformation to calculate wave frequency.....	84
Figure 4.20 Surface wave frequencies at different location for different time period.....	85

Figure 4.21 Wave frequency with standard deviation for the five repeatable measurements	86
Figure 4.22 $D_v(10)$ for different fluids at Location H7V0	87
Figure 4.23 $D_v(50)$ for different fluids at Location H7V0	87
Figure 4.24 $D_v(90)$ for different fluids at Location H7V0	88
Figure 4.25 SMD for different fluids at Location H7V0	88
Figure 4.26 The averaged SMD for different fluids at Location H7V0	89
Figure 4.27 The time-averaged droplet size distributions for different fluids at H7V0	90
Figure 4.28 The time-averaged droplet size distributions for different fluids at H9V0	93
Figure 4.29 The time-averaged SMD for different fluids at different locations from top to bottom: H7V0, H8V0, and H9V0	96
Figure 4.30 The time-averaged SMD for different fluids at different vertical locations.....	97
Figure 4.31 The averaged SMD over all the locations for different fluids.....	98
Figure 5.1 Starting stage of spray for different ethanol-water mixtures.....	114
Figure 5.2 Developed stage of spray for different ethanol-water mixtures	115
Figure 5.3 Ending stage of spray for different ethanol-water mixtures.....	116
Figure 5.4 Global spray structure of spray and the calculated spray cone angle.....	117
Figure 5.5 The average spray cone angle for different fluids and the error bars are based on 5 repeated runs	117
Figure 5.6 Calculation of the breakup length in a global near nozzle spray image	118
Figure 5.7 The average breakup length and the error bars for different fluids.....	118
Figure 5.8 Characteristic droplet diameters at different locations and their average values with error bars for different fluids: (a) D_v10 ; (b) D_v50 ; and (c) D_v90	119

Figure 5.9 The average SMD with error bars at different vertical locations: (a) 2.54cm from the axis; (b) 5.08cm from the axis; and (c) 7.62cm from the axis	120
Figure 5.10 The average SMD with error bars at different horizontal locations (a) and the average SMD over all locations (b)	121
Figure 5.11 The droplet size distribution at different vertical locations.....	122
Figure 5.12. The droplet size distribution at different horizontal locations (a) and the averaged particle size distribution over all locations (b)	123
Figure 6.1.Schematic of experimental setup.....	139
Figure 6.2 Geometry of the transparent swirl atomizer	140
Figure 6.3 Global spray structure and liquid film structure inside the nozzle.....	140
Figure 6.4 Experimental mass flow rates at different fluid pressures.....	141
Figure 6.5 Spray structure under different pressures for water and 40% glycerol/water mixtures.....	141
Figure 6.6 Spray cone angle under different injection pressures	142
Figure 6.7 Spray cone angle for different glycerol/water mixtures	142
Figure 6.8 Breakup lengths under different injection pressures	143
Figure 6.9 Breakup lengths for different glycerol-water mixtures	143
Figure 6.10 Liquid film images under different pressures for 30% glycerol/water mixture	144
Figure 6.11 Measured film thickness and fitting curves under different injection pressures	144
Figure 6.12 Liquid film images of liquid with different viscosity under 0.2Mpa	145
Figure 6.13 Measured film thickness and fitting curves for different glycerol-water mixtures	145

Figure 6.14 Comparison between measured liquid film thickness and estimated film thickness previous empirical equations of 70% glycerol-water mixture	146
Figure 6.15 Comparison between measured liquid film thickness and estimated film thickness previous empirical equations in 0.14Mpa	147
Figure 7.1 External flow structure of circular jet in different breakup regimes: (a) Rayleigh breakup regime. (b) First wind-induced breakup regime. (c) Second wind-induced breakup regime. (d) Atomization regime.....	161
Figure 7.2 Experiment setup of pressure injection system	162
Figure 7.3 Details of the plain-orifice nozzle	162
Figure 7.4 Mass flow rates of two liquid jets under different injection pressures.....	163
Figure 7.5 Evaporation rate for circular orifice nozzle.....	163
Figure 7.6 Evaporation rate for rectangular orifice nozzle	164
Figure 7.7 Reynolds number of liquid under different injection pressures	164
Figure 7.8 Weber number of air under different temperatures for circular jet	165
Figure 7.9 Weber number of air under different temperatures for rectangular jet	165
Figure 7.10 Transient images of circular jet under different pressures at 20°C	166
Figure 7.11 Transient images of circular jet under different pressures at 30°C	166
Figure 7.12 Transient images of circular jet under different pressures at 40°C	167
Figure 7.13 Transient images of circular jet under different pressures at 50°C	167
Figure 7.14 Transient images of circular jet under different pressures at 60°C	168
Figure 7.15 Breakup lengths under different temperatures for circular orifice nozzle.....	168
Figure 7.16 Transient images of rectangular jet under different pressures at 20°C.....	169

Figure 7.17 Transient images of rectangular jet under different pressures at 30°C.....	169
Figure 7.18 Transient images of rectangular jet under different pressures at 40°C.....	170
Figure 7.19 Transient images of rectangular jet under different pressures at 50°C.....	170
Figure 7.20 Transient images of rectangular jet under different pressures at 50°C.....	171
Figure 7.21 Breakup length change for rectangular orifice nozzle.....	171
Figure 7.22 Transient and averaged images of rectangular jet at 20 °C.....	172
Figure 7.23 Maximum wave length of rectangular orifice nozzle.....	173

1. INTRODUCTION

1.1. Motivation

Many industrial applications rely on spray systems to transform continuous liquid flow into discontinuous liquid droplets in order to effectively deliver the working fluid in a larger space and shorter time. These spray systems are found in but are not limited to spray drying [1], cooling [2, 3], painting, cleaning, drug delivery, internal combustion engines [4–6], aircraft turbine engines [7–9], sprinklers and fire suppression systems. The length scales of the formed droplets span from micrometers to centimeters. The time scales are from milliseconds to seconds in transient operations. Steady state operations are also normally found in spray systems. This variety results in a wide range of spray system designs. In addition to the spray system design, the characteristics of sprays are mainly governed by a few physical parameters, including spray injection pressure, ambient thermal conditions, such as pressure and temperature, and the physical and chemical properties of the working fluids.

As such, spray has been a century long research subject in the area of fluid dynamics. There are many pioneering works that have led to a general conclusion that the liquid surface instability plays a critical role on spray development, breakup, and atomization. Despite that have been many studies on the instabilities of the free non-swirling atomizers, investigations on spray structures and instabilities in swirling atomizers are still lacking and insufficient. Although swirling atomizers represent a simple spray system design. The characteristics of the resulted spray can nevertheless represent those found in complex spray systems. The

simplicity of the pressure swirl atomizer design also offers flexibility in terms of the experimental design. It is generally agreed that the in-nozzle flow characteristics are very influential to spray development. Compared to the relatively better understood surface instability, however, the influence of the upstream in-nozzle flow on the spray development is still being very actively explored mainly due to the lack of good experimental measurement approaches. With ever-increasing computing power, computational fluid dynamics (CFD) has become an indispensable tool to study spray and atomization phenomena. The high fidelity of the computer modeling relies on reliable quantitative experimental measurements. But such quantitative data are difficult to find, or if any, they usually subject to large uncertainties and are inconsistent in different literature.

All these facts have motivated the author's great interests in studying spray and atomization phenomena. Consequently, the author has conducted several research projects that were particularly designed to address the aforementioned problems. These projects also reveal that with the advancements in high speed image capture and the associated high quality image processing and analytic tools, quantitative measurements of spray characteristics can be achieved. The experimental approaches and results are reported in the rest of this thesis.

1.2. Research objective and approaches

As stated above, this work primarily focuses on experimental research. Spray characteristics and in-nozzle liquid film thickness are analyzed using image processing tools developed by the author. The measured data can be directly used to validate computational

models. Furthermore, Fast Fourier Transform (FFT) and non-dimensional analyses both lead to quantitative and conclusive results that can be used to compare similar experiments conducted by other research groups in a consistent manner. To describe the designed experimental projects and the associated outcomes, the thesis is organized as follows.

Chapter 2 reviews a number of research papers that are relevant to the present work. The chapter starts from introducing the definitions of the commonly used terminologies for spray characterization, including atomization, spray cone angle, breakup length, penetration, and film thickness. This is followed by a discussion on liquid instability and its effects on spray development. Several classical papers and their conclusions are also briefly discussed. The chapter includes some details on the experimental methods for droplet size and distribution measurements, as well as the underline principles of the experiment apparatus. Previous research on evaporating sprays is also a subject of the present chapter. Note that Chapter 2 is only a brief summary of several classic studies. More detailed reviews on the studies that are closely related to the author's research projects are provided in the introduction sections of Chapters 4 to 7.

Chapter 3 mainly describes the experimental equipments used in this study, including a high speed camera, data acquisition system, software environments, and spray droplet size measurement system. Detailed experimental setup and configurations are the subjects of Chapters 4 to 7 for different research projects.

Chapter 4 investigates the effect of liquid viscosity on spray characteristics in swirl atomizers. The fluid samples were made by blending water and glycerol in different ratios to

simulate fluids with different viscosities while keeping other physical properties relatively constant. This allows the experimental results mainly reflect the contributions due to liquid viscosity. The effects of liquid viscosity on the spray global structure and droplet size are discovered in this chapter.

Chapter 5 studies the effect of liquid surface tension on spray characteristics in swirl atomizers. Similar experimental approaches employed in Chapter 4 were used in the research project described in Chapter 5. But different from Chapter 4, the fluid mixtures were made by blending ethanol and water in different ratios to simulate fluids with different surface tension while keep other fluid properties relatively unchanged. In this way, the experimental measurements mainly reveal the contributions due to liquid surface tension. Conclusions are also made regarding to the relative importance of liquid viscosity and surface tension in different sprayer configurations in this chapter. However, evaporation of ethanol is found to influence the breakup and atomization process, which further motives the work in Chapter 7.

Chapter 6 mainly focuses on the study of liquid film thickness in spray nozzles. A transparent nozzle was designed in order to visualize the in-nozzle flow. Different from the previous two studies, the liquid flow and spray were maintained at steady state. The image processing methods used in Chapters 4 and 5 for transient spray characterization are modified in this chapter in order to capture the surface of the liquid film formed on the nozzle orifice wall. This is critical for reporting liquid film thickness accurately.

Chapter 7 explores the effect of ambient thermal conditions, specifically heating evaporation, on the primary breakup process of spray development. A heat source with

temperature control is used to provide proper thermal conditions. The main purpose of this project is to investigate whether the evaporation has an important impact on liquid jet breakup. If so, in which region the evaporation effect is the most influential. The two questions are addressed by using non-dimensional analysis on the measured data. Similar to Chapter 6, this study also works on steady state jets.

Chapter 8 highlights the important findings from the research projects conducted by the authors. The chapter also integrates the conclusions that have been drawn in Chapters 4 to 7. Based on the results and findings in this work, an outlook to the possible future directions is also provided.

2. LITERATURE VIEW

2.1. Atomization process

Atomization is the process in which a liquid jet or sheet is disintegrated by kinetic energy. It transforms bulk liquid into spray and other physical dispersions of small drops or droplets. The resultant suspension of fine droplets in a surrounding gas is termed spray, mist, or aerosol. This process can be created by exposing to high velocity air or gas, or as a result of mechanical energy applied externally through a rotating or vibrating device. Numerous spray devices have been developed and designed as atomizers or nozzles.

There are many industry spray applications, such as spray drying, spray cooling , and powdered metals in processing application; humidification and misting, evaporation and aeration in treatment application; surface treatment and spray painting in coating application; spray combustion used in oil burners, rocket, gas turbine, direct inject or port fuel injected engines.

Most practical atomization processes for normal liquids include: (a) pressure atomization, (b) two-fluid atomization, and (c) rotary atomization. Many other useful atomization processes for normal liquids have been developed for special applications, including: (a) effervescent atomization, (b) electrostatic atomization, (c) ultrasonic atomization, (d) whistle atomization, etc. These processes may be classified into two major categories in terms of the relative velocity between the liquid being atomized and the surrounding ambience. In the first category, a liquid with high velocity is discharged into a still or relatively slow-moving gas (air or other gases). Notable processes in this category

include pressure atomization and rotary atomization. In the second category, a relatively slow-moving liquid is exposed to a stream of gas with high velocity. Two-fluid atomization and whistle atomizers are usually considered to be the second category.

At a low injection pressure, the liquid emerges at a low velocity as a thin distorted pencil-shaped stream. For injection pressures in excess of the ambient pressure by approximately 150 kPa, the liquid issuing from the orifice forms a high velocity jet and disintegrates rapidly into droplets. Increasing the injection pressure can enhance the flow velocity of the liquid jet, leading to an increase in both the level of turbulence in the liquid jet and the aerodynamic drag forces exerted by the surrounding medium, and thereby promoting the disintegration of the liquid jet.

There are many high pressure nozzles used in combustion. They inject liquid fuels into diesel engines, spark ignition engines, gas turbines, rocket engines, and industrial furnaces. Most combustion systems require small fuel droplets to achieve high volumetric heat release rate, wide burning range, and low pollutant emissions. An effective atomization process increases the specific surface area of the injected fuel and thus enables high rate of mixing and evaporation. One of these high pressure atomizers is plain-orifice atomizers. They are widely used for injecting liquids into a flow stream of air or gas. The injection may occur in a co-flow, a counter-flow, or a cross-flow stream. The best known application of plain-orifice atomizers is diesel injectors. This type of injectors is designed to provide a pulsed or intermittent supply of fuel to the combustion chamber for each power stroke of the engine. As the air in the combustion chamber is compressed by the piston to a high pressure,

a very high pressure (>80 MPa) is required to allow the fuel to penetrate into the combustion chamber and disintegrate into a well-atomized spray. One of the limitations of plain-orifice atomizers is the narrow spray cone generated. For most practical applications, large spray cone angles are desirable. To achieve a wide spray cone, a pressure-swirl (simplex) atomizer can be used.

2.1.1. Swirl atomizer

A swirl atomizer (simplex) has a swirl chamber with a number of tangential inlets (holes or slots) and a circular outlet orifice. During the operation, a liquid is introduced into the swirl chamber through tangential ports and allowed to rotate. If the liquid pressure is sufficiently high, a high angular velocity is attained and an air-cored vortex is created. The swirling liquid then flows through the outlet of the swirl chamber and spreads out of the orifice under the action of both axial and radial forces, forming a tulip-shaped or conical sheet beneath the orifice. The sheet subsequently disintegrates into droplets. The liquid-air interaction, liquid surface tension and viscous forces are the primary factors governing the liquid breakup process.

There are two basic types of swirl atomizer. One is solid-cone spray atomizer in which the spray is comprised of drops that are distributed fairly uniformly throughout its volume. The other atomizer produces a hollow-cone spray in which most of the drops are concentrated at the outer edge of a conical spray pattern. The liquid emerges from the discharge orifice as an annular sheet, then spreads radially outward to form a hollow conical spray.

Various hollow-cone swirl atomizers have been developed for combustion applications. In these atomizers, swirl chambers may have conical slots, helical slots or tangential slots. Using thin, removable swirl plates to cut or stamp the swirl chamber entry ports leads to economies of the atomization systems if spray uniformity is not a primary concern. Large simplex atomizers have found applications in utility boilers and industrial furnaces. Zhao et al. [10] concluded that swirl atomizers have been dominantly used in direct injection (DI) gasoline engines because of the enhanced atomization characteristics through the breakup of a conical liquid film, which is initially formed inside the nozzle. Zhao et al. [11] also summarized the researches on DI gasoline engines and revealed that the DI gasoline engines require a well-atomized and well-stratified mixture near the spark plug.

2.2. External spray characteristics

The spray characteristics of the swirl atomizer, such as spray cone angle, breakup length, spatial velocity distribution, spray robustness and static air pressure inside the spray, should be controllable. There have been many researches related to the swirl spray development and atomization process. Lefebvre [12] reviewed studies about the swirl spray development concerning the effect of nozzle geometry and injector operating conditions, and the experimental and computational analyses were developed based on this review [13–15]. Furthermore, many breakup models for liquid sheets have been suggested [16, 17] and the linear instability analyses are based on these models to explore the atomization process of swirl spray. These characteristics are reviewed in the following sections.

2.2.1. Spray pattern

Spray pattern (mass distribution) is an important parameter that affects combustion efficiency and pollutant formation. Studies on spray pattern are useful in identifying the uniformities of spray. Cohen and Rosfiord [18] and Santolaya [19] studied the spray pattern resulting from swirl atomizers and concluded that the regime of spray evolution dictates the mass distribution. It was found that under low flow rate conditions the spray was a collapsed single and coarse jet with the maximum mass flux in the center. At higher flow rates the spray revealed a well-developed and symmetric hollow-cone structure. Santolaya et al. [20] found a sharp rise in the axial volumetric flux along the radial direction, which indicates liquid distribution in an annular region and formed a fully developed hollow cone. The maximum axial flux was found to decrease with increasing pressure due to the progressive spatial distribution of the liquid droplets.

2.2.2. Spray angle

Spray angle is an important characteristic to describe spray performance. Spray angle is usually defined as the angle formed by two straight lines drawn from the discharge orifice to the spray contours at a specific distance from the atomizer face. The spray angles produced by swirl atomizer are important in many applications. In combustion systems, spray angle has a strong effect on ignition performance, flame blowout limits, and the pollutant emissions of unburned hydrocarbons and smoke. Normally, a wider spray angle leads to improved atomization quality and better fuel-air mixing. While narrow spray angles can reduce spray impingement, it also reduce the covering area. Spray angle cannot be inferred precisely

without an experimental investigation into the specific configuration. Several studies have shown that the nozzle dimension and fluid properties have large impacts on spray angle. Chen [21] found that the spray angle increases continuously at low injection pressure and reaches a maximum at high injection pressures (0.34Mpa to 1.72Mpa). Ramamurthi and Tharakan [22] found that increasing swirl number leads to an increase in the spray angle in an experimental study. Spray angles produced by higher swirl number atomizers are found almost independent of injection pressures. Jeng et al. studied the liquid sheet emanating from simplex fuel nozzle using both computational and experimental methods. They found an increase in the length/diameter ratio of the final discharge orifice reduces the spray cone angle. They also revealed that liquid viscosity reduces the spray cone angle quantitatively [23].

2.2.3. Breakup length

Breakup length is the length of continuous portion of jet measured from nozzle exit to the point (location) where breakup occurs. In pressure swirl atomizers, breakup length is defined as the distance from nozzle exit to the point where the first ligament detaches from the liquid sheet. Arai and Hashimoto [24] studied the breakup length of liquid sheets using optical measurements. They found that the breakup length decreases with increasing relative velocity between the air and the liquid. They also found that breakup length increases as the liquid sheet velocity increases or as the liquid viscosity decreases. Kim et al. [25] showed that the aerodynamic force significantly affects the breakup of the swirling liquid sheets. The breakup length decreases with increasing aerodynamic force as the ambient gas density and Weber number increase.

2.3. Internal flow characteristics

Film thickness is the thickness of an annular liquid sheet as it discharges from the atomizer. In pressure swirl atomizers, the liquid emerges from the nozzle as a thin conical sheet that rapidly attenuates as it spreads radially outward. The liquid sheet further disintegrates into ligaments and then drops. In pressure swirl atomizers, the thickness of the liquid film in the final nozzle exit is directly related to the area of the air core. It has been recognized that the thickness of the annular liquid film produced at the nozzle exit has a critical effect on the mean drop size of the spray [25]. Rizk and Lefebvre [26] used a theoretical approach to investigate the internal flow characteristics of swirl atomizers. They studied the effects of atomizer dimensions and operating conditions on spray cone angle, velocity, and the film thickness of the annular liquid film formed at the discharge orifice. Their theory and experiment both indicate that a higher pressure drop produces a thinner liquid sheet. Increasing the inlet area raises the flow rate through the nozzle, which results in a thicker film.

2.3.1. Measurement methods of liquid film thickness

The characterization of the thin liquid film in the orifice is important to many applications, such as in steam power generation, oil delivery and refinement, chemical processing, and refrigeration systems. Accurate measurements of the thickness of the thin liquid films are crucial to study the heat and mass transfer characteristics in these applications.

Many methods for measuring the thickness of thin liquid films have been developed.

These measurement techniques can be categorized into intrusive and non-intrusive measurements. The intrusive methods, including electrical conductance techniques, and the non-intrusive methods, including optical, laser-induced fluorescence, ultrasonic and capacitance techniques, are reviewed in this section.

2.3.2. Conductance method

The use of contact needles and parallel-wire probes are currently the most popular method to measure the liquid film thickness. The method uses the conductance probes to correlate the film thickness to the electrical resistance between two electrodes. Brown et al. [27] used this method to measure the liquid film thickness in a gas-liquid flow. The conductance between two electrodes immersed in an electrolyte reaches a constant value and the phase of the impedance goes to zero when the frequency of the applied ac signals is sufficiently high. Then, the conductance between the two parallel-wire probes varies linearly with the film thickness. However, this conductance method has several drawbacks. Because the probes are inserted into the liquid film, they may disturb the film flow and produce vortex shedding, which leads to vibration of the probes. This causes fluctuations in the electrical resistance and therefore produces noise in the output signals. In addition, when the liquid thickness decreases in a wavy film, a higher liquid thickness may be obtained and a certain amount of lag may be introduced in the probe dynamic response. Another restriction of the conductance method is that it only calibrates steady state flows, but in reality transient flows may not have the same characteristics of the steady-state cases.

2.3.3. Optical method

Optical methods used to measure liquid film thickness include but are not limited to laser scattering and laser shadow methods. Both of these methods use a single light source. With the laser scattering technique, the measured liquid with seeded particles is illuminated. The amount of the light scattered by the particles depends on the film thickness.

Salazar and Marschall [28] used a laser beam to illuminate a liquid seeded with latex particles in their study. The light intensity scattered from the liquid film was measured using photodiodes. The laser shadow technique illuminates the liquid interface where the laser is both reflected and refracted. A variation in the light intensity is created and measurable. This method was employed by Zhang et al. [29] who measured the thickness of falling liquid films between 0.4mm and 0.9mm. In their experiments, a laser light sheet was reflected and refracted by a liquid film, which generated a shadow region. The liquid film thickness was determined by measuring the light intensity using camera and photodiode. The variation of the amplitude of the film waves can be measured from the output of the photodiode. The average film thickness can be measured from pictures of the shadow using computer aided image analysis. Compared to the popular conductance probe method, the optical method has the advantages of convenience, noninvasiveness, higher spatial and temporal resolution, and smaller hysteresis. More importantly, it does not disturb the liquid surface.

Shedd and Newell [30] developed a nonintrusive, automated, and optical film thickness measurement technique which can be used for a wide range of fluids and flow measurements, as shown in Figure 2.1. In this method, the light is reflected from the surface

of a liquid film flowing over a transparent wall. The reflected light generates an image on the outside of the wall which is captured and digitized using a charge coupled device (CCD) camera. The image is processed to determine the positions of the reflected light rays with which the film thickness is calculated. An automated calibration procedure allows for the determination of the necessary physical parameters. The advantage of this method is the index of refraction of the test fluid or the test section wall need not be known.

2.3.4. Laser-induced fluorescence/ planar laser-induced fluorescence method

Another optical method is to trace fluorescent dye in liquids. The fluorescent dye presents at a known concentration in the liquid forming the film and emits visible light when it absorbs UV light. Figure 2.2 shows that the visible light is captured by a camera and the varying intensity of the fluorescence signal is recorded across the whole area of interest. Smart and Ford developed a correlation between the brightness of the fluorescent film and the film thickness [31]. And the brightness was represented in grey level in the film visualization. They first discussed the principle of this method in 1974. They also used it to measure the thickness of the lubricant films on a rotating cylinder. The test lubricants were either naturally fluorescent or doped with fluorescent dye. Because the limitation of their apparatus, they could only determine the thickness at a single spot. Makarytchev et al. measured the thickness of liquid films flowing on a rotating conical surface [32]. Their experiments were performed with a strongly fluorescent dye with emission at a wavelength of 521 nm and the film thicknesses between 0.05mm and 1.5 mm were measured. Calibration of the measuring system was performed with stationary liquid films of known thickness.

Using digital methods to capture and analyze optical images have largely improved the reliability and repeatability of laser-induced fluorescence methods. For example, Schubring et al. developed a planar laser-induced fluorescence method to determine the film thickness distributions in upward vertical annular flows [33], as shown in Figure 2.3 and Figure 2.4. An advantage of this method is that the variation of the film thickness can be determined instantaneously over a wide area on the optical images. The fluorescence intensity increases with liquid film thickness at a fixed dye concentration. Therefore, it is possible to calibrate the light intensity change by viewing the film at the wavelength of the fluorescence related to the film thickness.

Comparing to the conductance method, optical and laser-induced fluorescence techniques have several major advantages:

- 1) It is able to visualize the thin film of annular flow based on the produced images. Conductance probes produce no data beyond a time-series of conductivity or a related parameter.

- 2) Unlike the implicitly spatially-average conductance probe data, high axial resolution can be obtained in images.

- 3) Small scale measurements are impossible with conductance probe, while optical and laser-induced fluorescence techniques can detect very small amplitude between the base films. Flow waves can be observed directly from the images.

- 4) With enhancement of the quantification of errors and improvement of image

processing algorithms, the processed results can be compared to raw images in optical methods. However, with the conductance probe method, it is not easy to identify the errors in the results and is not possible to reprocess the data.

5) Optical and laser-induced fluorescence are non-intrusive methods. They do not require the installation of a probe into the flow. Thus they do not disturb the film flow and produce vortex that may possibly lead to erroneous results.

However, careful calibration and accurate images processing are very important in order to achieve acceptable precisions using optical methods.

2.3.5. Ultrasonic methods

The propagation of sound has been used as a diagnostic tool to measure and characterize a variety of thin layers and films, such as oil films on lubricated components and thin plates of polymers. Many of these investigations are conducted by examining the reflection of an ultrasonic pulse generated and received by the same transducer in a normal-incidence fashion. The film thicknesses are determined using both time domain and Fourier analysis techniques.

The ultrasonic technique has been applied successfully to several different film configurations. These include both static and growing non-condensing films, a non-condensing film with surface waves. The ultrasonic technique for liquid film layer thickness measurement usually uses the impulse-induced resonance method. High frequency acoustic waves are attenuated and reflected at discontinuities in a medium at a liquid-gas or liquid-

solid boundary. The transit time of a pulse is used to measure the film thickness. As a result, such technique is applicable to a large range of film thicknesses.

Chang et al. first showed that an ultrasonic transducer can be used to measure film thickness [34]. They reported the use of an ultrasonic transducer to identify the flow regimes in two-phase flows in 1982. Lu et al. used an ultrasonic transducer to measure the condensate film thickness on the horizontal lower surface of a rectangular duct [35]. The liquid film thickness was determined from the product of the transit time and the sound velocity in the liquid phase. With such measurements at five different locations on the condensing surface, both the local and average convective heat transfer coefficients were obtained.

Chen et al. developed a pulse-echo ultrasonic system to measure the thickness of condensate liquid films in real time [36], as shown in Figure 2.5. The reflected energy due to the broadband ultrasonic pulse falls in equally spaced narrowband frequency ranges where the spacing depends on the film thickness. Because the echo received by the transducer from the copper/liquid interface is much larger than the filtered signal of interest from the fluid layer, the signal must be normalized by subtracting the effect of the copper/liquid interface echo before this analysis can be performed.

2.3.6. Capacitance methods

The capacitance method, as a low-cost and high precision non-contact measurement method has been used to measure film thickness by Klausner et al. [37] and Thorncroft and Klausner [2.29]. When an alternating voltage is applied between two opposed conducting plates, a capacitance is measurable and depends on the dielectric constant of the medium

between the plates and the distance between the plates. So the value of the capacitance directly indicates the film thickness. This method requires electrical isolation of the contact elements, otherwise it would give a composite film thickness value over the whole surface. It also requires the positioning and alignment of small surface-mounted sensors.

2.3.7. Liquid film thickness inside swirl atomizer

Among the discussed methods, the electric conductivity method and photography technique have been dominantly employed for the liquid film thickness measurement in swirl atomizers. In the conductance method, an electric potential is applied to the electrodes which enclose the test liquid film and the current between them is measured. Because the conductivity is correlated to the film thickness, the resulted current or voltage can therefore be used to quantify the film thickness. Suyari and Lefebvre used this method in a film thickness measurement inside an atomizer [39]. They produced flow water through the atomizer and measured the electrical conductance. The conductivity of water between the two electrodes is known. This measurement provided a direct indication of the average liquid thickness in the flow path between the two electrodes. The system was calibrated by flowing water through the nozzle and measuring electrical conductance with a plastic rod of low electrical conductivity inserted along the axis of the nozzle discharge orifice. By repeating this measurement with rods of different diameter, a calibration curve was obtained to correlate the voltmeter reading to the film thickness.

Kim et al. used a similar electrical conductance method to study the effect of geometric parameters on the liquid film thickness and air core formation in a swirl injector

[40]. However, they designed a transparent injector that enables them to visualize the in-nozzle flow and to reveal the relation between variations of the air core in the swirl chamber and the liquid film thickness. This provides a more accurate measurement technique to calibrate various liquid film thicknesses. In their experiment, the injector parts were changeable in order to investigate the variation of liquid film thickness with the geometric parameters of the injector.

However, it is noted that the electrical conductance method is intrusive and is only suitable for conducting liquids. Consequently, most of the experiments using the electric conductivity method were performed in large nozzles due to the difficulty in electrode installation within the very limited in-nozzle space.

The spray structure outside the nozzle orifice is relatively easy to measure but the air core inside the swirl chamber and liquid film thickness inside the nozzle orifice are more difficult to visualize. The application of optical methods requires either that one of the contact elements is transparent or that it contains a transparent window. In the direct photography, the error associated with different refractive indices of transparent nozzle, liquid and air, was not considered in previous studies [41, 42]. This uncertainty in the liquid film measurement should be reduced by error analysis. Moon et al. used the direct photography method to measure the liquid film thickness inside transparent nozzles using a pulsed light source [43], as shown in Figure 2.6. The back-illumination technique was adopted in order to capture the microscopic images of the film flow inside the nozzle. A CCD camera was used to capture the back-illuminated images. A pulsed light was projected

to the very small area of the film flow inside the nozzle and a copper diffuser was installed to distribute the light uniformly. The error in liquid film thickness measurement was estimated and then corrected based on the geometric optics.

Instead of measuring the liquid film directly, many researchers also designed experiments with indirect methods to measure the air core diameter. In these experiments, the liquid film thickness was determined by the air core formed in the swirl chamber because the difference between the measured air core diameter and the nozzle orifice diameter is equal to twice of the film thickness assuming the symmetry. Kutty used an indirect measurement method to study the influence of liquid pressure on air core size[44].

The images of the upstream liquid through the nozzle orifice were recorded by a camera. A transparent window at the rear of the swirl chamber was installed in order to achieve enough illumination. The air core diameters were then measured by enlarging them in a microfilm reader.

2.4. Droplet size and distribution

Spray is considered as a collection of drops immersed in gas phase. Most atomizers generate drops in the range from a few micrometers up to around 500 micrometers. Droplet size is one of the most important parameters to evaluate spray atomization quality. For example, in most combustion systems, reduction in drop size leads to higher volumetric heat release rates, a wider burning range, and lower pollutant emissions. In other applications, however, small droplets must be avoided because their settling velocity is low and, under certain meteorological conditions, they can drift too far downwind. Drop sizes are also

important in spray drying and must be closely controlled to achieve the desired rates of heat and mass transfer.

2.4.1. Measurement methods

There are numerous methods applied in measuring droplet size and distribution, and they can be divided into three categories: mechanical, electrical and optical methods. The mechanical methods involve the collection of a spray sample on a solid surface or in the cell containing a specific liquid. After that, the sizes of the droplet impressions are measured by using photograph, or with the aid of microscope. This method is simple and has many variations, and now been replaced by photographic and optical methods.

Electrical methods basically measure droplet size distribution via detection and analysis of electronic pulses produced by spray. Charged wire and hot wire are two normally used techniques. Charged wire method uses the principle that a droplet impinges on an electrically charged wire, and the droplet size has a relation of the amount of charge it removes. Gardiner [45] pointed out that the limitation of the charged wire probe depends on a combination of electrical conductivity of liquid and the droplet flux. A liquid with lower conductivity produce pulses of longer duration, and result in higher probability of counting errors. The hot wire method is based on the principle that when a liquid droplet attached to a heated wire, and the local cooling by the drop reduces the resistance in proportion to the droplet size. This method also has many limitations. It can only measure large drops under low flow speed, as a result of drop shattering on the wire. Also the liquid residue on the wire will affect calibration.

Optical measurement can be divided into imaging and non-imaging methods. The imaging methods usually use high speed photography and holography, but have the limitation of detectable droplet sizes due to the resolution of high speed camera. Non-imaging methods can be divided into two classes. One is counting droplet size individually, while the other is measuring large number of droplets simultaneously. Each method has its own advantages and limitations, but the most important advantage is that the optical methods do not need the insertion of a physical probe into the spray.

High-speed visualization is often used to provide instantaneous images of the drops in a spray for subsequent counting or analysis. The method is nonintrusive, but cannot show the temporal distribution of the drop size directly. The spatial distribution of drop sizes taken by instantaneous images can be converted into the true temporal distribution by multiplying the number of droplets in any given size range by the average velocity for that size range.

Another mostly used method for measuring droplet size and distribution is single particle counters, which measure individual particles or drops that pass through a focused laser beam. The size of the measurement volume sets the limitation on the drop number densities, which is controlled by the diameter of the focused beam, the f number of the receiver lens, lens angle to the transmitted beam, and the aperture of the photodetector. Bachalo described the theory of dual-beam light scattering that the spatial frequency of the scattered interference fringe pattern is inversely related to the droplet diameter [46]. He then derived a method using pairs of detectors at fixed spacing in the image of the interface or fringe pattern. The measurement is relatively unaffected by the random beam attenuations

provided the signal to noise ratio is sufficient. The instrument response is linear over the entire working range and has a large dynamic size range. The method has been implemented into a phase Doppler particle analyzer (PDPA). The various mean sizes, mass flux, number density, and mean velocity can all be measured using PDPA.

2.4.1.1. *Light diffraction technique*

The theory for the scattering properties of particles of arbitrary size and arbitrary refractive index occurring in polydispersion of finite optical depth was first derived by Dobbins [47]. For a polydisperse system, the radiant intensity $I(\theta)$ scattered at a small angle θ from the forward direction due to an incident planar wave of irradiance E_0 can be written as

$$\frac{I(\theta)}{E_0} = \frac{D^2}{16} \left\{ \alpha^2 \left[\frac{2J_1(\alpha\theta)}{\alpha\theta} \right]^2 + \left[\frac{4m^2}{(m^2 - 1)(m + 1)} \right]^2 + 1 \right\} \quad (2-1)$$

where E_0 is incident irradiance, $I(\theta)$ is radiant intensity, θ is scattering angle, α is size number $\pi d / \lambda$, where λ is the wavelength of incident light, m is refractive index, J_1 is Bessel function of first kind of order unity.

The normalized integrated intensity of forward-scattered light, $I(\theta)$, due to a polydispersion of relatively large particles is

$$I(\theta) = \frac{\int_0^\infty \left[\frac{2J_1(\alpha\theta)}{\alpha\theta} \right]^2 N_r(D) D^4 dD}{\int_0^\infty N_r(D) D^4 dD} \quad (2-2)$$

where the integral of over a given diameter interval represents the probability of occurrence of particles within the specified interval.

2.4.2. Representative diameters

Droplet diameter is a very important parameter to describe a spray. The mean droplet size and size distribution depend on many variables, such as operation conditions, liquid properties, and nozzle geometry. A high injection pressure, low ambient pressure and/or small orifice diameter lead to small droplet sizes. The concept of the mean diameter has been generalized and its notation standardized by Mugele and Evans [48].

$$(D_{ab})^{a-b} = \frac{\int_{D_0}^{D_m} D^a (dN / dD) dD}{\int_{D_0}^{D_m} D^b (dN / dD) dD} \quad 2.4-3$$

where a and b can take on any values corresponding to the effect investigated, and the sum a+b is the order of the mean diameter. Equation (2-3) represents a relationship between the angular distribution of scattered light and the particle size distribution. For example, D_{10} is the linear average value of all the drops in the spray; Sauter mean diameter(SMD) D_{32} is the diameter of a drop whose ratio of volume to surface area is the same as that of the entire spray.

2.4.3. Mathematical distribution function

Because the graphical representation of drop size distribution is not easily related to experimental results, many researchers have attempted to replace it with mathematical expression. Many droplet size distributions in random droplets follow the mathematical functions such as normal, log-normal, Nukiyama-Tanasawa, Rosin-Rammler, and upper-limit distributions. These mathematical expressions can provide satisfactory fits to the drop size data and allow extrapolation to drop size outside the range of measured values.

2.5. Instability of liquid jet

The spray characteristics discussed in the previous sections, such as spray angle, the spray drop size, and the jet breakup length, have been related to the instability mechanism. The instability and breakup of liquid jets into drops has been a subject of interest for more than 100 years. A liquid jet emanating from a nozzle into an ambient gas may breakup into small drops when it is subjected to disturbances. These disturbances may be in the form of surface displacement, pressure or velocity fluctuations in the supply system or on the jet surface, as well as fluctuations in liquid properties such as viscosity

and surface tension due to variation in thermal conditions. Pressure disturbances are normally attributed to sound waves on the jet. Surface disturbances can be created using a piezoelectric transducer at the nozzle which contracts and expands periodically by applying a periodic voltage on it. Velocity disturbances can be applied by using an oscillating flow. Temperature disturbances can be introduced by applying a periodic heating on a jet. Temperature changes the liquid surface tension, which affects the capillary action of the jet. Disturbances introduced by adding surfactants to the liquid jet are similar to the effect due to temperature.

A classical study of the instability of liquid jets was published in the seminal works by Rayleigh [49]. With the assumption of an inviscid liquid, he obtained an equation for the growth rate of a given axisymmetric surface disturbance by equating the potential and kinetic energies computed for the flow. Furthermore, with the hypothesis that the disturbance with the maximum growth rate would lead to the breakup of the jet, he obtained an expression for the resulting droplet size assuming that it would be of the order of the wavelength of this disturbance.

After numerous experimental investigations and the qualitative descriptions obtained from the linear stability theory, the disintegration of a liquid jet can be classified into distinct regimes of breakup. The different regimes are characterized by the appearance of the jet depending upon the operating conditions. The regimes are due to the action of dominant forces on the jet, leading to its breakup, and it is important that these forces can be identified in order to explain the breakup mechanism in each regime. As reviewed by Grant and Middleman, four different breakup regimes were defined depending on the interaction of the liquid inertia, surface tension, and aerodynamic forces acting on the jet [50]. In order to form a jet, the liquid must have sufficient momentum else it is discharged in the form of dripping drops. Once the initial momentum is gained, the jet breakup length increases linearly with the jet velocity. This linear variation of the breakup length with jet velocity corresponds to the Rayleigh jet breakup mechanism. This is caused by the growth of asymmetric oscillations on the jet surface, induced by surface tension. Drop diameters exceed the jet diameter as predicted by Rayleigh. Thereafter, the curve reaches a peak and then decreases. This regime is termed as the first-wind induced regime. Here, the surface tension effect is augmented by the relative velocity between the jet and the ambient gas, which produces a static pressure distribution across the jet, thereby accelerating the break up process. Similar to Rayleigh breakup regime, the breakup takes place in many jet diameters downstream of the nozzle.

For higher jet velocities, the nature of the breakup curve remains controversial. According to Haenlein, the breakup curve remains constant or decreases slightly with increasing velocity and then it abruptly reduces to near zero [51]. These two behaviors of the breakup curve indicate existence of two distinct regimes in the jet breakup. According to

Reitz and Bracco [52], at sufficiently high jet velocities, jet surface disruption occurs prior to the jet core. Hence, they defined two different breakup lengths, the intact surface length and the intact core length, to clearly demarcate the two phenomena. In Rayleigh and first wind-induced regimes, the jet breaks simultaneously over the entire cross section and hence, the two lengths coincide. In the high jet velocity regime, where the jet disruption initiates at the surface and eventually reaches the core, the intact surface length is different from the intact-core length. This regime is called the second wind-induced regime. Owing to high relative velocity between the jet and the ambient gas, the jet is subjected to short wavelength and thus, high energy surface waves. This wave growth is opposed by the surface tension. Jet disintegrates several diameters downstream the nozzle and the average drop diameter is much smaller than the jet diameter. The regime where the intact surface length becomes zero is identified as the atomization regime. The breakup curve follows the trend suggested by Haenlein [51] that the breakup length drops to zero. Here, the jet disrupts completely at the liquid-gas interface and the drops formed are much smaller than the jet diameter. So far, the disruption of the jet at higher jet velocities has been attributed to the effect of surrounding gas.

2.6. Instability of liquid sheet

In many spray nozzles, the bulk liquid is first transformed into a liquid sheet prior to the atomization process. The liquid sheet exiting a nozzle may experience certain oscillations, which result in the formation of liquid ligaments. The ligaments are then broken into small droplets, forming the spray. The spray droplet sizes are generally in the same order of the

liquid sheet thickness. Therefore, by forming a thin liquid sheet one can generate small droplets. Liquid sheet instability is due to the interaction between the liquid and its surrounding fluid. When the amplitude of a perturbation grows and reaches a critical value, the sheet is disintegrated forming liquid ligaments. The linear and nonlinear instability of an inviscid and viscous liquid sheet are discussed in this section.

There have been many studies on the temporal and spatial instability of liquid sheet. Among these, Dombrowski and his coworkers conducted extensive studies on the factors influencing the breakup of sheets and obtained information on the wave motions of high velocity sheets [53–56]. More recent analyses are provided by Senecal et al. [57], and Rangel and Sirignano [58].

In a two-dimensional liquid sheet, the sheet instability is mainly due to the aerodynamic interactions between the liquid and its surrounding gas. Contrary to the cylindrical liquid jets, surface tension forces tend to stabilize a planar liquid sheet. Generally, two modes of oscillations are considered: symmetric and antisymmetric. In the symmetric mode, also referred to as the dilational mode or varicose wave, the middle plane is undisturbed. In the antisymmetric mode, also referred to as sinuous wave, the free surfaces move in the same direction and with the same magnitude. Squire [59] and Hagerty and Shea [60] showed that for the inviscid sheets, the antisymmetric mode is the dominant mode of disturbance.

2.6.1. Inviscid liquid sheet

Sirignano and Mehring provided the growth rates for various wave numbers for both

sinuous (antisymmetric) and dilational (symmetric) waves, as well as for different Weber numbers and density ratios [61]. Their results also showed that the varicose mode is more unstable for density ratios near unity. It is clear that for the low Weber number case, the growth of sinuous waves dominate the growth of varicose waves due to the higher growth rates throughout the range of instability.

Dombrowski and John combined a linear model for temporal instability and a sheet breakup model for an inviscid liquid sheet in a quiescent inviscid gas, to predict the ligament and droplet sizes after breakup [56]. Their study showed that symmetrical waves are mainly responsible for ligaments break down.

Ibrahim developed a power series mathematical solution for the problem of instability of an inviscid liquid sheet of parabolic velocity profile emanated from a nozzle into an inviscid gas [62]. The results show that for both antisymmetrical and symmetrical disturbances departure from uniformity of the velocity profile causes the instability to be reduced. It has been suggested that jet instability may be affected by the relaxation of the velocity profile that takes place once the liquid exits the nozzle and is no longer constrained by its wall.

2.6.2. Viscous liquid sheet

Linear instability analysis of viscous liquid sheet is not found as many inviscid liquids as in previous literature. Senecal et al. concluded that liquid viscosity reduces both the maximum growth rate and the corresponding wave number [57]. In addition, the effect of viscosity is minimal for Squire's regime. A critical Weber number of $27/16$ was found, and

the fastest-growing waves are short waves. The inclusion of the viscous terms is necessary to accurately predict the wave growth of short waves. Also the wavelength is in the same order of the sheet half-thickness.

2.7. Evaporation effect

Evaporation is a phase transition process by which molecules in a liquid overcome their intermolecular attraction forces and escape into the surrounding gas environment. When heat is supplied to a liquid, its temperature, and hence the kinetic energy of the liquid molecules, are increased, which results in an increased evaporation activity. Also, a decrease in the ambient pressure increases the chances of the liquid molecules near the surface to overcome their intermolecular attraction potential, which results in an increased evaporation rate. In this exposition, the evaporation process is discussed from a continuum point of view using the conservation equations for mass, momentum and energy that take discontinuities in the density at the phase boundary into consideration. A comprehensive discussion of droplet vaporization can be found in the studies by Sirignano [63], Crowe et al. [64], and Sazhin [65].

2.7.1. Drop evaporation

The evaporation of drops in a spray involves heat and mass transfer processes. The heat for evaporation is transferred to the drop surface via conduction and convection from the surrounding hot gas. The vapor is transferred by convection and diffusion back into gas phase. The overall rate of evaporation depends on the pressure, temperature and the properties of the liquid and gas. Experimental observations in moderate pressure environments show that a drop is initially subject to a transient heating process until it

reaches steady-state vaporization. The latter is described by the well-known d-squared law, which gives the square of the drop diameter as a function of time, t , by the relation:

$$d^2(t) = d_0^2 - \beta_v t \quad (2-4)$$

where d is the drop diameter, d_0 is the initial diameter, and β_v is the evaporation coefficient.

2.7.2. Liquid jet evaporation

The breakup of a liquid jet is known to be affected by various disturbances such as the surface displacement, the pressure or velocity fluctuations in the supply system or on the jet surface, as well as the fluctuations such as temperature, viscosity, and surface tension on liquid properties. The instability and breakup of liquid jets into drops have been a subject of interest since the early nineteenth century and has continued to date [66–68]. However, these numerous studies focused on the instability of non-evaporating jets majorly. There are very limited studies addressing the instability of an evaporating jet, especially the effects on the primary breakup. This section reviews the previous studies on liquid jet breakup and instability under evaporating conditions.

The classical breakup of liquid jets is associated with Rayleigh's capillary instability which can be dated back to 1878. This is primarily due to axisymmetric capillary disturbances which grow temporally and lead to pinching of the jet into a regular row of droplets. In the Rayleigh regime which applies to low speed jet breakup, the drops are of the sizes comparable to the jet radius. When a liquid is ejected from the nozzle into an

unsaturated vapor pressure environment, the liquid flows can be treated as a superheated jet. The superheated interface between the liquid jet and its surrounding may also become unstable. This instability can greatly affect the hydrodynamic and thermal processes as well as the geometry of the jet.

The existing theoretical considerations for evaporating liquids, such as linear and nonlinear approximations provide us some thoughts of the possible mechanism responsible for the evaporation driven surface instabilities. It has been found that the most important element in the development of the instability is the variation in the mass flux caused by the local change in the temperature gradients at the surface. The vapor fluxes from the liquid crest when the first surface instability appears. The thermal boundary layer is stretched and decreased. And from the depression, the boundary layer is compressed and increased. At least three phenomena are considered as the possible causes responsible for the instability of the surface.

The first one is the vapor recoil mechanism, which results from the additional pressure generated by the vapor leaving the surface. The pressure pushes the liquid surface into the region of increased evaporation rate, thus the liquid is squeezed from original position into crests. The second mechanism is the moving interface. It results from the surface degradation. Rapid evaporation enhances the removal of liquid from the depressions which further increases their depth and amplifies the original disturbances. The last one is the Marangoni effect. The temperature difference between depressions and crests causes changes of the surface tension, which is a driving force for the liquid flow from the hot spots

(depressions) to the cold crests. Sultan et al. studied the stability of an evaporating thin liquid film on a solid substrate [69]. The stability depends only on two control parameters, the capillary and Marangoni numbers. The Marangoni effect is a destabilizing process whereas capillarity and evaporation are stabilizing processes.

Prosperetti and Plesset [70], and Higuera [71] studied the stability of an evaporating horizontal planar surface of superheated liquid with infinite depth. They assumed that the time scale for the development of the surface instability is much shorter than that for the evolution of the basic configuration. The basic state is then considered as quasi-steady. It was shown that in the absence of significant relative velocity between the liquid and the gas, the development of the instability is due to the effect of vaporization on the pressure field. The evaporation flux and pressure at the depressions were found to be higher than that at the crests so that the liquid was squeezed into the crests causing the crests to grow. They considered both transfer rates across the interface and diffusion of the vapor in the gas phase in order to predict the evaporation rate quantitatively.

Lian and Reitz studied the effect of vaporization on liquid jet atomization [72]. A linear stability analysis is presented for an evaporating jet. They focused on the stability of a liquid jet, where the jet velocity is higher than the jet surface regression rate. They made an assumption that the development of the surface hydrodynamic instability is much faster than the surface evolution due to the evaporation. Thus the breakup of the jet is dominated by the aerodynamic interaction between the liquid and gas at the interface, rather than by thermal instability as mentioned by Prosperetti et al. [70]. This allows the process to be considered as

quasi-steady, and the normal mode method for the steady basic solution is applicable as an approximation. They found that for low speed jets undergoing Rayleigh breakup, jet surface evaporation is a destabilizing factor. But for high speed atomizing, jets surface evaporation becomes a stabilizing factor. This is due to the fact that the evaporation flux distributions at the depressions and crests of the waves on the surface of the liquid jet are different for these two breakup regimes.

A dimensionless parameter Va was obtained by Lian and Reitz to represent the degree of surface evaporation [72]. A larger value of Va indicates a stronger evaporation. As Va increases, the growth rate of all the unstable waves increases indicating that the surface evaporation in the Rayleigh regime is a destabilizing factor. Interestingly, for high speed jets in the atomization regime, the effect of surface evaporation helps stabilizing the spray. A similar dual-behavior has been observed for the effect of surface tension in liquid sprays by Lin and Lian [73]. For low-speed jets, the mechanism of jet breakup is capillary pinching and the surface tension contributes to destabilizing spray. However, the strong aerodynamic interaction at the interface creates a rapid formation of small droplets in the high-speed jets. The surface tension force therefore becomes a stabilizing factor resisting the jet breakup.

Saroka et al. numerically investigated the temporal instability of an evaporating liquid jet by studying the effects of liquid Reynolds number, disturbance wave number, and the surface evaporation rate on the growth rate of the instability [74]. They compared the results with linear analytical solutions and showed that the evaporation increases the growth rate of instability. For small evaporation rates the swell grows in the same manner as that for the

non-evaporating case. As the evaporation rate increases, the evaporation mechanism begins to dominate. The jet breakup time and the main drop sizes both decrease. The results show that the main size decreases with decreasing Reynolds number and increasing wave number and evaporation rate. For large evaporation rates the main drops become very small or even completely eliminated. The evaporation rate propagation of the disturbance is no longer linear. Thus the linear analysis is not able to predict the growth accurately.

Despite the number of theoretical studies on instability of evaporating liquid film and jet, very few experiments have been conducted. Stability of evaporating surfaces strongly depends on vapor mass flux and surface temperature. Direct measurement of these values in a jet is rather difficult because intrusive probes cannot be used. For a droplet it is possible to measure its temperature using an indirect method to correlate its surface tension using the oscillating droplet method [75]. For a jet flow this method cannot be readily applied, and an appropriate evaporation model must be used to estimate it.

The combination of free-surface flow and heat and mass transfer equations results in a strong nonlinearity which is difficult to describe both theoretically and experimentally. In experiments the strong fluctuation of the breakup distance, which appears independently of external conditions and indicates the existence of such nonlinearity. In order to obtain a basic understanding of the evaporation process, Kowalewski et al. built an experimental apparatus and designed a novel measurement method to investigate the liquid evaporation from a small diameter liquid jet flowing into a low pressure chamber [76]. The process was visualized by CCD cameras. The scheme of the experimental apparatus is shown in Figure 2.7.

Experiments have been performed with pure ether or ethanol, and an equal volume mixture of the two. In the high-pressure neutral gas environment, the evaporation process is relatively slow, and it mainly controlled by the rate of vapor diffusion from the surface. The presence of external gas additionally affects the evaporation rate due to a lateral gas flow close to the nozzle. The growth rate of the instability waves may also be influenced by the aerodynamic effects at the surface. In a low pressure and rich vapor environment, the rate of evaporation is only limited by the gas-kinematic conditions at the surface. The influence of external gas on the surface instabilities is not expected to be significant. However, the initial evaporation rate near the outlet of the jet depends primarily on the heat flux at the surface.

The results of their observations indicate that the problem of evaporation induced instabilities of small liquid jets is very complex. Various forms of surface instability may appear at similar experimental conditions. Stable cylindrical jet can also be observed at low ambient pressures, which are more suitable for instabilities. In general, the higher the evaporation rate, the stronger the possibility of observing the first surface instabilities is. If this instability is large enough, the cylindrical jet shape becomes detached, and the theoretical models for regular surfaces can no longer be used.

2.8. Summary

With a thorough review of the previous literature, it is concluded that the transformation of bulk liquid into sprays and other physical dispersions of small drops in a gas phase is important in many industrial processes. In the past decades, there has been a tremendous interest in studying the science and applications of the atomization. This growth

of interest has driven a huge progress in spray measurement technology, as well as mathematical model developments for spray systems. It becomes more and more important for engineers to acquire a better understanding of the basic atomization process. It is also critical for engineers to have the capability to select the most suitable type of atomizer for any given application. And the effect of the liquid properties and operation conditions on the performance of atomizer should also be well characterized. These are the main subjects of the present work.

2.9. Table and figures

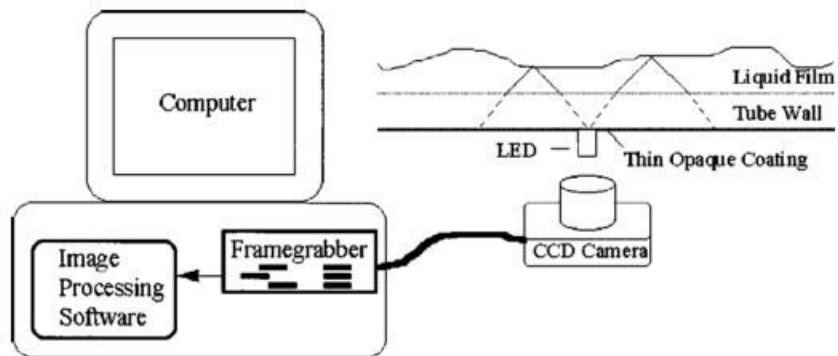


Figure 2.1 Schematic of the automated optical film thickness measurement system [30]

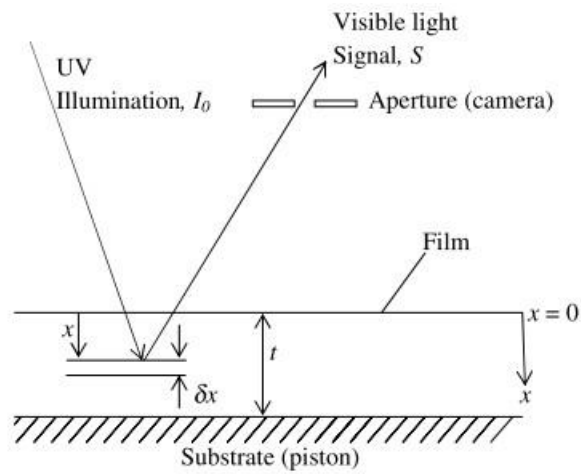


Figure 2.2 Theoretical schematic of the fluorescent dye technique [31]

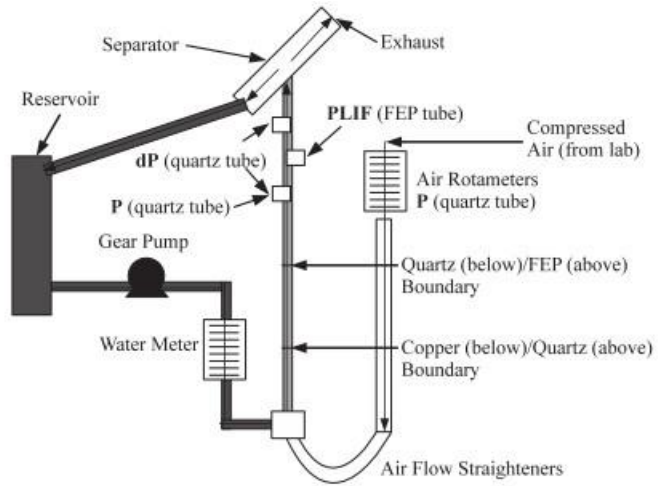


Figure 2.3 Diagram of a flow loop [33]

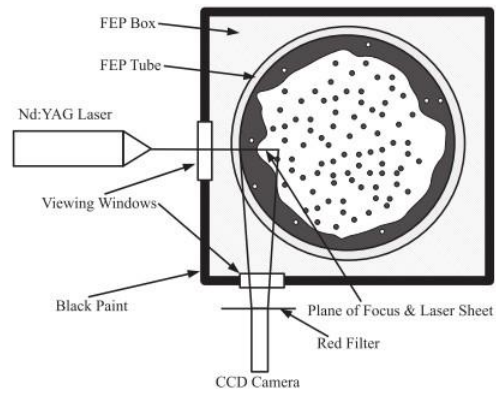


Figure 2.4 Test section for PLIF measurements [33]

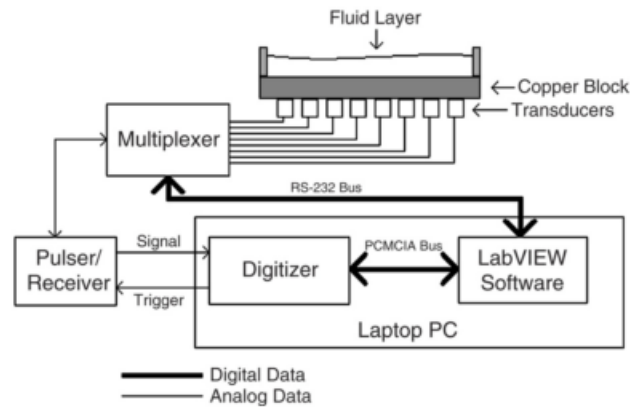


Figure 2.5 Schematic of the ultrasonic fluid thickness measurement system [36]

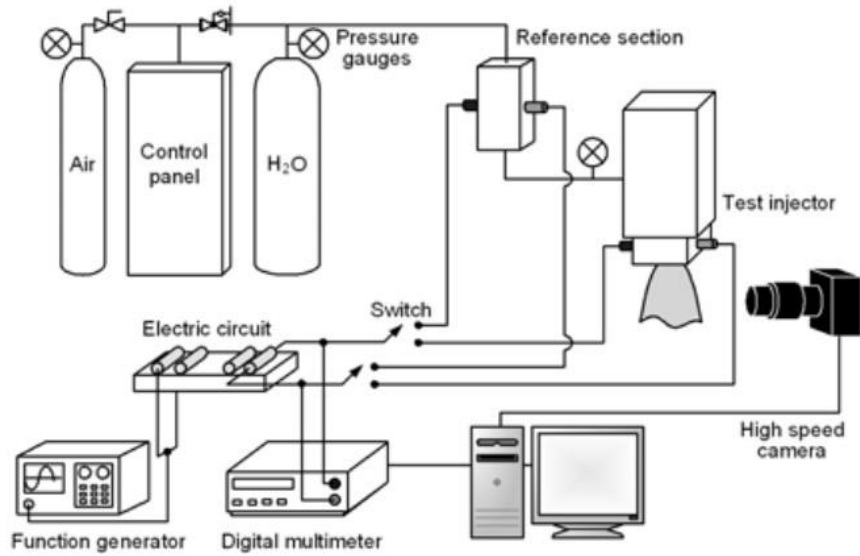


Figure 2.6 Schematic of the experimental apparatus for liquid film thickness [43]

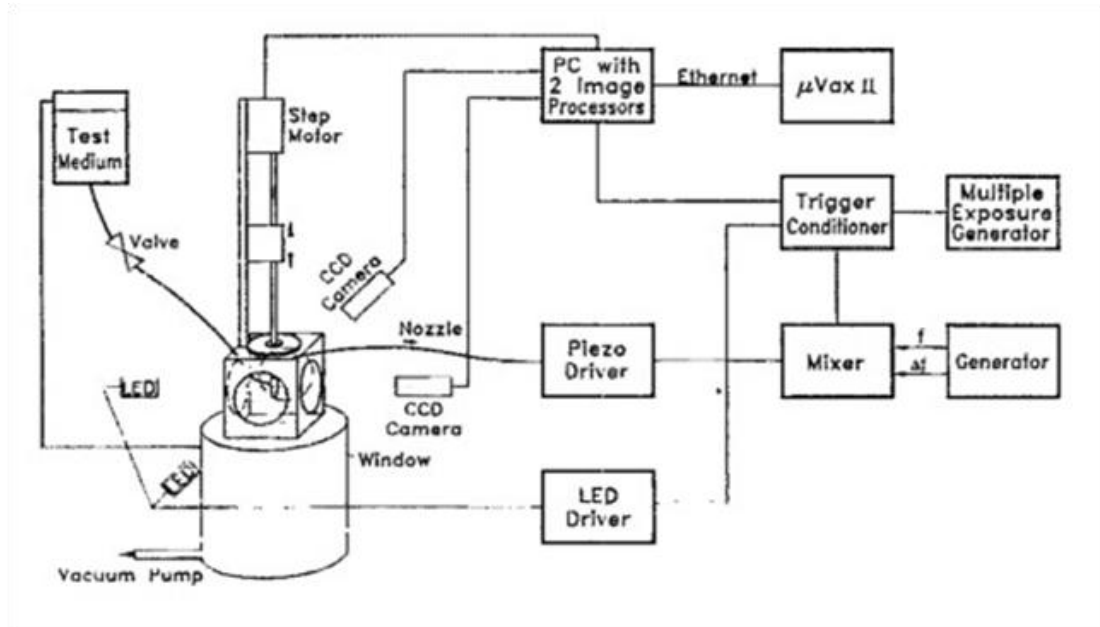


Figure 2.7 Schematic of the experimental apparatus for evaporation jet analysis [76]

3. EXPERIMENTAL SYSTEM AND METHOD

3.1. Optical measurement system

3.1.1. High speed camera

A high speed imaging technique was used to visualize the spatial spray structure in the near-nozzle region during the liquid dispensing process. Images of the near-nozzle region spray were acquired using a Phantom V4.3 digital high-speed CMOS video camera with a Nikon 50mm focal lens and a Nikon 60mm Micro lens. The high speed imaging process was synchronized with the dispensing process by using an external trigger signal from the trigger sprayer actuator. The camera resolution was adjusted to obtain a compromise between frame rate and image resolution. Different regions of interest were applied due to the various requirements over the course of the study. These include the near nozzle spray images used for cone angle calculation and the global nozzle spray images for breakup length and surface wave instability analysis.

3.1.2. Backlit system

A backlit system is critical for image quality, and further determines the accuracy of image processing results. As showed in Figure 3.1, a 1000W light source and a light diffuser were used at the backside of the spray to maintain the uniformity of the light illumination in order to capture high quality images. To get higher light collection efficiency, an optimized optical system for back-illuminated imaging was applied to low pressure jet [77]. As shown in Figure 3.2, an engineered diffuser is used to distribute an extended light source through a controlled range of angles, and a field lens is used to redirect the light to the camera.

3.2. Data acquisition system

3.2.1. Sensors

The transient data of the liquid pressure, the pressure forces on the piston, and the displacement of the dispensing piston are required to analyze the transient dispensing process of the pressure swirl atomizer. To accomplish the simultaneous measurement of the three important signals, three types of sensors were installed on the pressure atomizer. The sprayer was fitted with a displacement sensor and a pressure sensor, and the actuator arm was fitted with a torque sensor, as shown in Figure 3.3.

3.2.2. Hardware and software configuration

To synchronize the event and control data acquisition, an NI PCI-6013 board and two OMEGA OM2-162 boards were used. NI PCI-6013 is an analog-input multifunction DAQ (Data Acquisition) board. OMEGA OM2-162 is a complete signal conditioning system on a card designed for either half or full bridge transducers. It consists of a high performance instrumentation amplifier, a user adjustable active filter, high stability bridge supply and all of the required circuitry, trim pots, etc. A control box was customized to accommodate all the data communication interfaces and trigger signal, as shown in Figure 3.4. Amplify signal NI LabVIEW 8.5 was used to code and realize functions of the system. The interface of LabVIEW control panel is shown in Figure 3.5 for the measurement of the trigger sprayer.

3.3. Droplet size measurement system

Characterization of the droplet size and distribution is important to quantify the atomization quality of atomizers. The laser diffraction technique is useful for such

measurements, especially for the transient spray process in the present study. In this work, a laser diffraction technique was used to measure the droplet size and distribution for different fluids at different locations during the transient dispensing process. The equipment is a SprayTec[®] particle size analyzer from Malvern Instruments Inc., which is able to achieve up to 10kHz sampling rate for transient spray analysis. The SprayTec particle analyzer system was triggered by the triggering pulse from the actuator. A sampling rate of 5kHz for rapid measurement and the measuring duration of 1000ms were used in this work. The measurement window of Malvern SprayTec[®] is shown in Figure 3.6. The detectable droplet size range is from 0.1 μm to 900 μm .

The set up of droplet size measurement system is shown in Figure 3.7. In order to easily change the location of the laser beam relative to the sprayer nozzle, a translational stage was used. The whole spray actuation system was installed on the translational stage. For each fluid, nine locations were measured, including three locations in the horizontal direction, from 17.78 cm (7 inch) to 22.86 cm (9 inch) downstream of the nozzle with a step of 2.54 cm (1inch). Six positions tested in the vertical direction, from -7.62 cm (lower than nozzle) to 7.62 cm (high than the nozzle axis) with a step of 2.54 cm. There were 10 repeated runs for each fluid at each location.

As showed in Figure 3.8, the transmitter side generates a 1mm laser beam. When passing through a laser beam, the particles scatter light at different angles. The diffract angles are directly related to their sizes. As the particle size decreases, the observed scattering angle increases. The observed scattering intensity is also dependent on particle sizes. Thus, large

particles scatter light at narrow angles with high intensity. Small particles scatter at wider angles but with lower intensity. The focal plan with 36 detectors is in the receiver side. Based on the detectors' signal, transient droplet size and distribution can be measured.

3.4. Summary

The experiment facilities and technologies described in this chapter have facilitated this research work. Spray visualization technology was used to provide the instantaneous images of a spray, which were recorded for subsequent analysis. Laser diffraction technology was used in simultaneous measurements of droplet size and distribution, which can detect a wide range of drop size at a high data acquisition rate. The sensor signals were measured using data acquisition boards. The measurement process was controlled by a LabView code. The experiment setup for each research project will be described in more detail in the following individual chapters.

3.5. Tables and figures

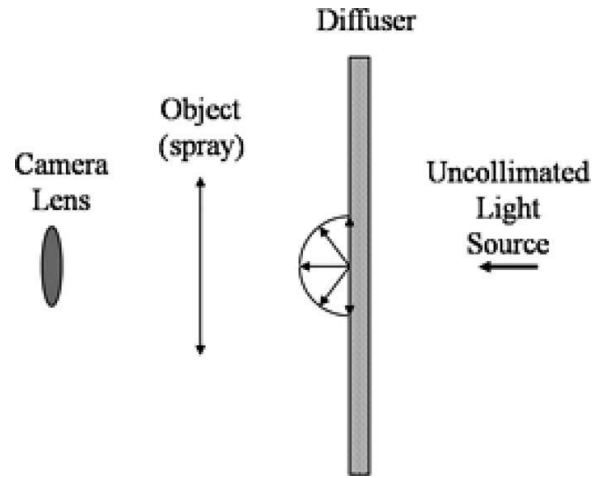


Figure 3.1 Standard flood illumination system used for backlit imaging [77]

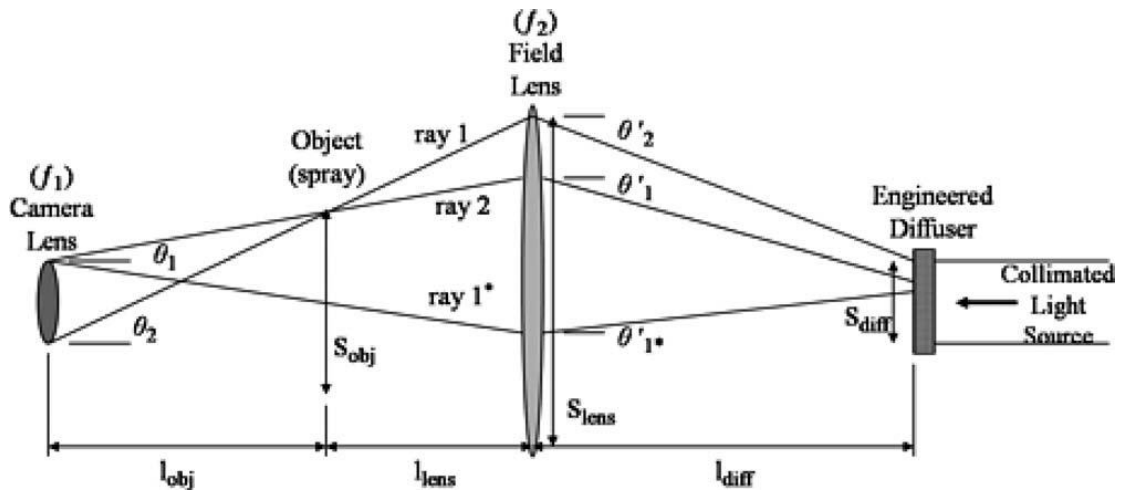


Figure 3.2 Optimized lighting system [77]



Figure 3.3 Sensors installed on a trigger sprayer

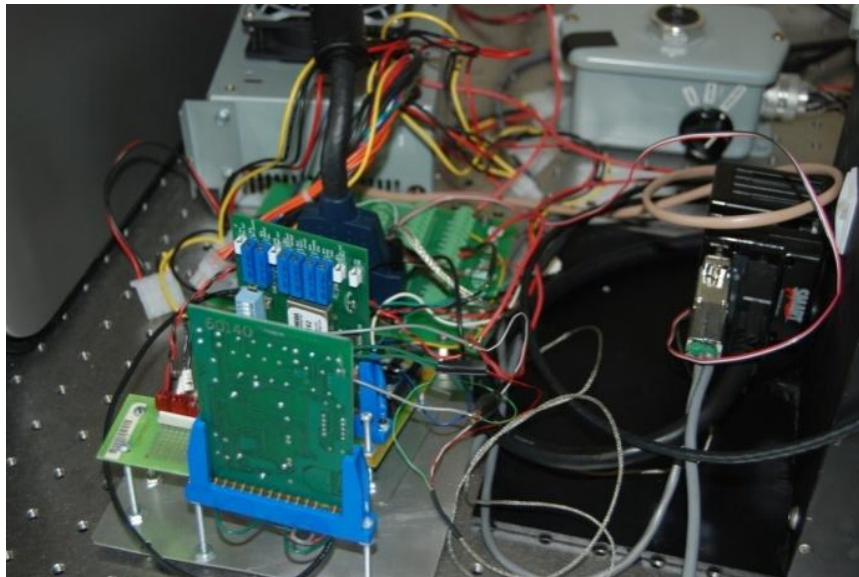


Figure 3.4 Signal conditioning modules and data acquisition system

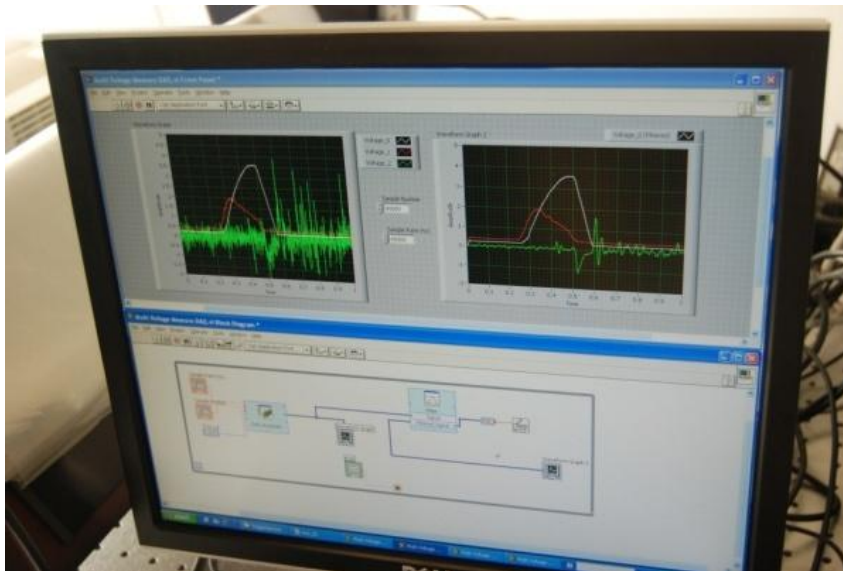


Figure 3.5 LabView interface

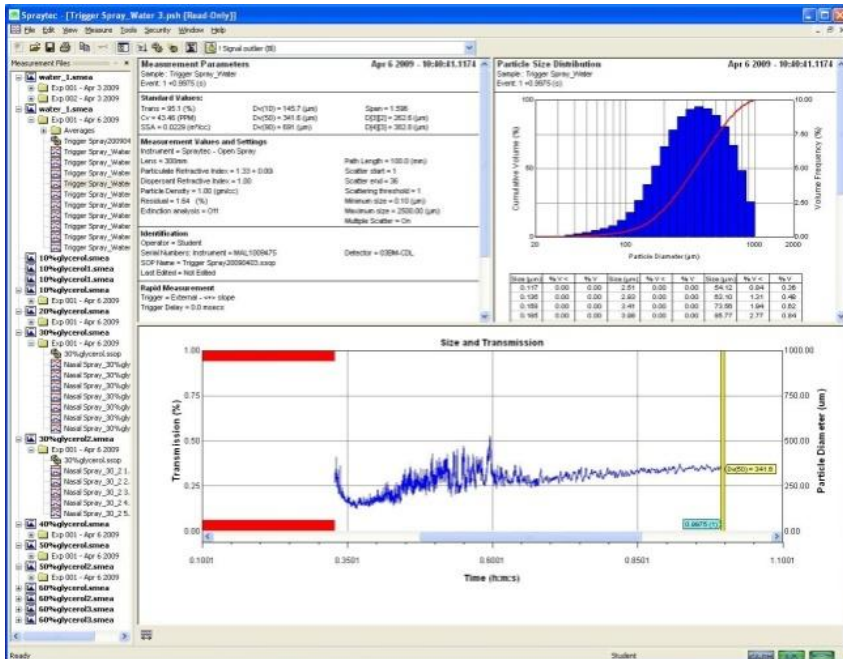


Figure 3.6 Measurement window of SprayTec software

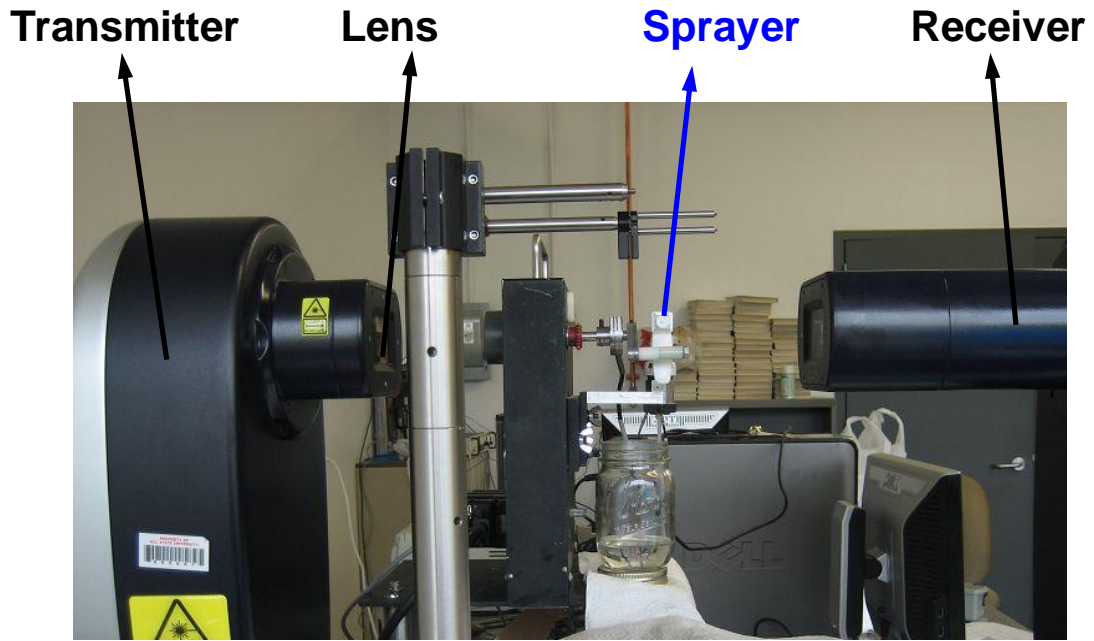


Figure 3.7 Setup of droplet size measurement

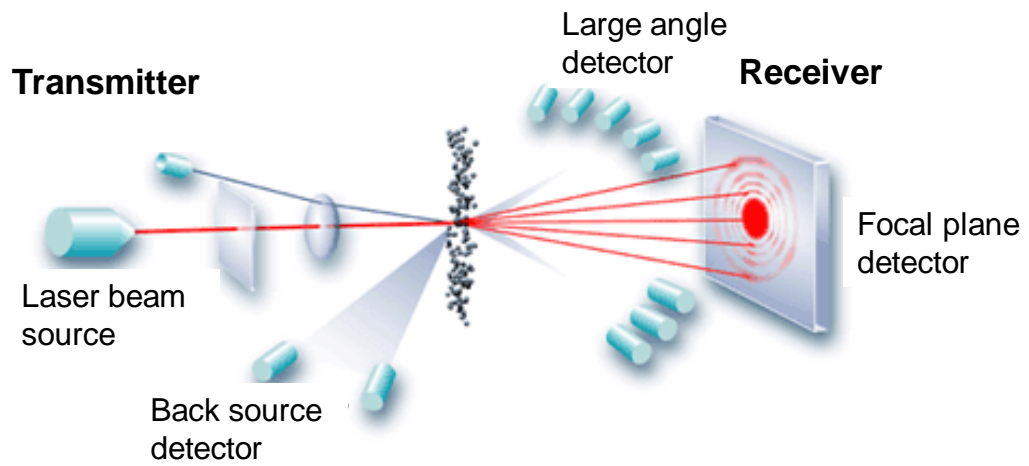


Figure 3.8. Laser diffraction technology[47]

4. EXPERIMENTAL STUDY ON GLYCEROL-WATER MIXTURES

4.1. Introduction

Liquid spray and atomization systems have been found in many applications, including processing industries (spray drying, spray cooling), coating applications (surface treatment, spray painting), combustion (burners, furnaces, internal combustion engines, jet engine, and rocket motors), and medical and printing applications. Pressure swirl atomizers are widely used in these devices, from fuel injection spray in power generation engines to various liquid dispensing sprayers used in packaging applications, due to their good atomization characteristics and geometrical simplicity. The operating principle of swirl atomizers relies on the conversion of pressure into kinetic energy to achieve a high relative velocity of the liquid with respect to the surrounding gas, by means of a nozzle. Thus, a swirling motion is imparted to the liquid so that under the action of the centrifugal force it spreads as a conical sheet as soon as it leaves the nozzle orifice. The importance of the hydrodynamic behavior of the flow within a swirl atomizer has been recognized and studied by many researchers in the past decades. Previous studies have analyzed experimentally and theoretically the characteristics of the complex internal flow of different atomizers [78, 79]. To understand the spray characteristics formed by swirl injectors, many investigations of fuel liquid sprays have been carried out using several measurement techniques, such as laser induced fluorescence (LIF) [80-81], Phase-Doppler Anemometer (PDA) [82-87], and a laser sheet method with a high-speed camera [88-93].

The stability of the ejected liquid sheet from swirl atomizers plays an important role on spray development, liquid breakup, and atomization. Despite the fact that there have been many studies on the spray instability of free non-swirling atomizers, investigations on spray structure and instability in swirling atomizers are still lacking. The instability causes the liquid sheet to break into ligaments, and subsequently into drops, in the form of a well-defined hollow cone spray. The atomization process which occurs in swirl injectors is driven not only by the liquid sheet breakup but also by the collision between droplets and the interaction between drops and the surrounding environment [94-96].

A pioneering work of classical studies on the instability of liquid jets was conducted by Rayleigh [49]. Squire provided a further understanding of the atomization process based on his instability analysis of liquid sheets [97]. Ponstein was among the pioneers who carried out an analysis of the stability of an annular swirling liquid sheet [98]. He derived the general dispersion relation for the growth of disturbances under the influence of potential liquid swirl flow and the uniform axial mean velocity. However, his research neglected the effects of viscosity and the presence of two phases. The liquid swirl with non-axisymmetric modes is more unstable than with the axisymmetric mode. There are complicated competitions among these forces which determine the stability of the liquid sheets. Extensive researches were conducted thereafter, for example by Taylor [99], Levich [100], Sterling and Sleicher [101], and Reitz and Bracco [102]. Forces such as the inertial force, surface tension, aerodynamic force, viscous force, and centrifugal force are all involved in the spray disintegration process. Some of these factors suppress the disintegration process while the others promoting it. It is

generally agreed that the aerodynamic instability of the liquid sheet is responsible for the disintegration process. The breakup phenomenon has been extensively studied, particularly in plane configurations. Lefebvre observed that a collapsed tulip-shape sheet changed to a diverging wavy sheet as the liquid injection pressure increased [103]. The effect of fluid properties on the sheet characteristics was also examined through experimental methods [104, 105]. It was demonstrated that increasing the viscosity or the surface tension of the liquid injected inhibits the growth of surface waves.

Liquid viscosity directly influences the surface stability of spray sheets, which consequently affects downstream atomization quality. Therefore, it is critical to understand its associated underlying mechanisms for both atomizer design and optimization. Although many researchers have done considerable experiments to study spray systems, the viscous flow characteristics in trigger sprayers need more investigation. For example, Liao et al. studied an inviscid and swirling annular liquid sheet in order to predict the performance of a constant pressure swirl atomizer [106]. However, it is very difficult to accurately predict the atomization quality based on the empirical equations for different atomizer designs and for viscous fluids, which renders design optimization impossible. Mehring and Sirignano analyzed the nonlinear distortion and breakup of a swirling axisymmetric thin inviscid liquid sheet and at zero gravity [61]. By comparing with an annular sheet which is stabilized by a constant gas-core pressure, they showed that it is the swirl that reduces breakup lengths and times. They also showed that liquid swirl can enhance wave growth of the unstable mode resulting in shorter breakup length.

The purpose of this study is to investigate the effects of fluid viscosity on the spray instability and disintegration process during the transient operation of a swirl atomizer in a trigger sprayer. To simulate fluids with a wide range of viscosities, water-glycerol mixtures were used as working fluids. A high-speed digital camera was used to visualize the near-nozzle spray structure. The digital images of the sprays were further processed to analyze the spray cone angle, spatial spray structure, and the temporal waves at the cone surface. In this chapter, experimental setup and sample fluid properties are first described. This is followed by a demonstration of spray images obtained from a variety of fluids with different viscosities. The wave frequencies for a range of different viscosity fluid are then calculated by Fast Fourier Transform (FFT) to show the temporal wave propagation characteristics. Finally, several conclusions are summarized based on the results and observations.

4.2. Experimental Setup and Fluid Samples

The experimental schematic is depicted in Figure 4.1. In order to acquire detailed information for the transient dispensing process of the pressure swirl atomizers in a trigger sprayer, the transient data of the displacement of the dispensing piston were measured. The pressure swirl atomizer is inside a trigger sprayer. The nozzle diameter is 1mm with three tangential inlets in the swirl chamber. An electronically controlled actuator was used to press the trigger of the sprayer to initiate the liquid dispensing process. The use of this actuator improves the repeatability of the present experimental study. In order to synchronize the displacement measurement with the high speed spray images, the high speed camera and the data acquisition system were triggered by a pulse from the sprayer actuator. The

displacement data were sampled with a rate of 40kHz. Near-nozzle region spray was visualized using the high speed digital camera (Phantom v4.3 from Vision Research Inc.) at a frame rate of 32000 frames/second with an exposure time of 7 microseconds and a resolution of 112×96 pixels. This visualized region corresponds to a near nozzle region of 9mm×7.7mm. The spray was illuminated by a 1000W stage light source.

4.2.1. Fluid Samples

The working fluids with different viscosities were prepared by mixing distilled water and glycerol with different volume ratios from 0% to 90% with a step of 10%. For the wave frequency analyses, 60% to 74% glycerol-water mixtures with a step-size of 2% were used, because preliminary experiments showed that it was difficult to calculate the wave frequency for fluids with glycerol outside of this range. The experiment temperature was maintained at the room temperature (74 °F = 23.3 °C). The fluid viscosity is listed in Table 4.1 for different mixtures. The surface tension of water and glycerol are close at the room temperature (water is 72mN/m and glycerol is 63mN/m). So it was determined that the surface tension of the working fluids mixture did not vary too much (as compared to the viscosity) with the glycerol ratio in different blends. It is seen in Table 4.1 that the viscosity of the liquid increases sharply when the percentage of glycerol in the mixture is high (e.g. >50%).

4.3. Sensor data comparison

4.3.1. Displacement comparison

The transient displacements of the dispensing piston for fluids of 0-80% glycerol are shown in Figure 4.2. The working process of trigger sprayer can be divided into three steps:

the initial dispensing process, the maximum dispensing stroke, and the piston release process. In Figure 4.2, it is observed that the trend of the displacement is very different for fluids with different viscosities. With the increase of viscosity, the evidence of a sharp drop and raise in the displacement curves becomes more obvious at the maximum stroke. Viscosity also affects the piston compression, release, and maximum stroke. Higher viscosity leads to smaller maximum dispensing stroke. The discharge valve opens later for more viscous fluid mixtures. The reason is that with higher in-chamber pressure the chamber expands with a smaller stroke. It is also seen in Figure 4.2 that the piston release process becomes slower for liquids with higher viscosity. This is due to the higher friction force during the piston release process. For a very viscous fluid such as 80% glycerol-water mixture, the piston dispensing curves show hesitation during the release process. Also for the initial stage, the pressure valve opens later for a higher viscosity fluid, which indicates that the pressure establishment in the dispensing chamber is later for a more viscous fluid.

4.4. Spray spatial structure

Because the near nozzle region is critical to the liquid atomization for the downstream sprays, the development processes of the sprays in this region were investigated in more detail from the spray images, namely the starting, developing, and ending stages, as shown in Figure 4.3 to Figure 4.5. In Figure 4.3, it can be seen that the spray structure is similar for 0 to 40% glycerol-water mixtures, but the structure dramatically changes for 50 to 90% glycerol-water mixtures. The cone of the spray for more viscous fluid is smaller than that of a less viscous fluid. For the 90% glycerol fluid, the breakup is very weak, which is due to the

effect of very high viscous force. And it is easy to understand that the initial dispensed liquid does not have enough momentum at the start stage, as shown in Figure 4.3.

The developing stage of the spray is illustrated in Figure 4.4. When the fluid leaves the nozzle, it forms a cone due to the swirl motion in the swirl chamber, and the surface wave starts to propagate and grow spatially and temporally. As the liquid sheet becomes thinner and the surface wave oscillation magnitude increases on the surface of the spray, the sheet begins to break up and atomize to small droplets. The spray breakup length is defined as the distance between the nozzle outlet and the initial breakup point of liquid sheet ligament. The breakup length is found to increase as the fluid viscosity increases. In other words, breakup becomes more difficult for high viscous flows. For the mixture with 90% glycerol, the fluid only forms a spinning jet or stream. It does not break up in the near-nozzle imaged region, which is quite different from that of the 80% glycerol-water mixture. These results indicate that viscosity plays an important role in determining the structure of the spray and the atomization of the liquid.

The spray images near the ending stage of the fluid dispensing for different fluids are shown in Figure 4.5. Near the end of the injection process, the cone continues to shrink and collapses back to an onion shade due to the low fluid velocity. This stage is mainly responsible for the poor atomization near the end of the spray. When the volume mixing ratio of glycerol is above 40%, the fluid does not break up due to the loss of the pressure and flow velocity. For 70-90% glycerol-water mixture, a fluid stream is observed at the end stage. The global spray structure evolution with time is further illustrated in Figure 4.6 for 80% and 90%

glycerol-water mixtures. For the mixture of 80% glycerol, the fluid dispensed out at the very beginning does not break up. As the spray develops, a cone is formed and instability begins to take place when the jet reaches a certain distance from nozzle. Beyond this distance, the fluid breaks up into large droplets. When the velocity is high enough, the large droplets break into smaller droplets. When the velocity is low, the large liquid blobs cannot be further atomized due to weak interaction with the ambient air. At the end stage of the spray development, triple-branched liquid sheets are observed. At this stage, again due to the lack of momentum, the fluid cannot form small droplets. For the mixture of 90% glycerol, an interesting phenomenon is that when the flow comes out from the nozzle outlet, it forms three liquid sheet branches moving downstream. This is similar to the end stage of 80% glycerol spray. During the dispensing process, the liquid comes out of the nozzle as a spinning stream.

4.5. Spray cone angle analysis

It is agreed that the combination of liquid inertia, surface tension and aerodynamic forces affects the liquid breakup. Liquid breakup characteristics such as the spray drop size, the breakup length, and the spray cone angle are related to the unstable wave growing process. The centrifugal force plays a role in the breakup mechanism in pressure swirl atomizers where liquid enters tangentially to create a swirling liquid sheet. These types of atomizers usually result in wider spray cone angles than those of plain-orifice nozzles.

The digital spray images were post-processed using MATLAB on a personal computer for the measurement of the spray cone angles. A representative spray cone angle of

a certain working fluid is demonstrated in Figure 4.7. Figure 4.8(a)-(d) demonstrate the image processing procedure. The first step is to adjust the image intensity values, and then to convert the intensity image to a binary image. Because in the experiments there exists an unavoidable reflected light that results in some dark areas (as seen in Figure 4.8(a)), these areas need to be filled. It is also necessary to crop the image to a specified rectangle near the nozzle region so that all the edges are within the images. Then, clear surface profiles can be obtained based on the gradient information, as shown in Figure 4.8(e).

The transient changes of the spray angle for each fluid sample (shown in Figure 4.9) are the averages of four individual measurements. Each cone angle line represents the mean value of twenty points over the time. The trend of the spray angle changing over the time is clear. It is observed that the spray cone angle forms the earliest for 0% glycerol-water and the last for 80% glycerol-water mixture. At the developed stage, the spray cone angles change slightly. As the time evolves, the cone angle becomes smaller due to the loss of momentum. For 0% glycerol, the cone angle does not drop sharply, compared to the other mixtures.

Figure 4.10 illustrates the mean spray cone angle as a function of the logarithm of the liquid viscosity. The error bars represent the standard deviation in the four repeated experimental observations. The mean values of the cone angles for the fluid samples are also provided in Table 4.2. As observed in Figure 4.10, the spray cone angle decreases as the liquid viscosity increases from 0% to 50% percent glycerol-water mixture. However, the cone angle only slightly decreases about 9 degree. This should not be unexpected, since it is seen that in Table 4.1 the liquid viscosity does not increase too much in this

range. However, for fluids with higher viscosity, such as from 60% to 70% glycerol, it is seen that the spray cone angle reduced dramatically compared with the less viscous fluid. For the most viscous fluid, 80% glycerol-water mixture, the cone angle is only about half of that of the pure water.

4.6. Instability of liquid sheet

4.6.1. Temporal structure comparison

For an unsteady spray from a swirl atomizer, the surface waves propagate and grow spatially with time, which are determined by the wave number and frequency in space and time, respectively. The liquid sheet breakup is controlled by both spatial and temporal instabilities. The wave propagation of a liquid sheet surface can be expressed by

$$D = M \times \exp[(i \times (kx + 2\pi ft))] \quad (4-1)$$

where D is the surface wave displacement, M is the surface wave magnitude, k is the wave number in space, i is the imagery unit with $i = \sqrt{-1}$, and f is the oscillation frequency in time. The surface wave propagation on the cone surface is very important in the spray breakup and atomization process. Temporal surface wave oscillation can be obtained by fixing a location and observing the wave change as a function of time. In this way, spatiotemporal diagrams can be obtained for frequency analysis. An example of the spatiotemporal diagram is shown in Figure 4.11. These spatiotemporal diagrams provide very important information for the cone surface displacement changing with time and therefore help to identify the spray development in time domain.

In order to show the temporal spray structure the spatiotemporal diagrams at different locations are shown in Figure 4.11. The distances from the left image edge for the four locations (No. 1 to No. 4) are 1mm, 4.17mm, 10mm, and 13.33mm. By comparing the structure at different locations, the wave propagation and growth along the cone surface can be clearly demonstrated.

These spatiotemporal diagrams at different spray stage for different fluids are shown in Figure 4.12 to Figure 4.15. The temporal spray structure offers important information of spray development in time. When spray reaches Location 1, fine droplets are generated for most of the fluids measured. The observed large liquid blobs on the head of the spray are due to the fluid staying in the nozzle. At the developed stage, the surface structure becomes smoother for more viscous fluids. The more fractured structure indicates better liquid breakup and atomization. Periodic fluid oscillation is observed for 70% and 80% fluids, indicating a dominating frequency propagating along the cone surface. Near the end of the spraying process, smaller droplets are observed for less viscous fluids. For 60-80% fluids, stream-like fluid blobs pass through Location 1. Compared to Location 1, Location 2 is more upstream and closer to the nozzle. For the starting stage, spray structure is similar to Location 1. During the developed stage, the spray temporal structure is also similar to Location 1, but the surface becomes less fractured in time as compared to Location 1. The spray dimension is slightly smaller than that of Location 1. At Location 3, the diameter becomes much smaller than that of Location 2. Early development is similar for all the measured fluid samples. The surface structure is quite rough but there is no void in the surface indicating no breakup at this location.

At the developed stage, the spray cone becomes smoother with a tubular structure in time compared to that of Location 2. The time tube diameter becomes smaller with the increase of viscosity. The oscillation magnitude is also smaller than that of Location 2. 70% and 80% glycerol-water mixtures show a very smooth structure with little oscillation. Location 4 shows the spray cone for a near-nozzle region. The head of the spray clearly indicates the large droplets during the starting of spraying due to fluids sitting in the nozzle. Near nozzle cone structure shows fewer disturbances on the surface with poorer breakup.

4.6.2. Analysis of surface wave frequency

As mentioned in Equation $D = M \times \exp[(i \times (kx + 2\pi ft))]$ (4-1) temporal surface wave oscillation can be obtained by fixing a location and observing the wave change as a function of time. In this way, spatiotemporal diagrams can be obtained for temporal frequency analysis. In this analysis, the location number increases in the picture from the left edge to the right, as illustrated in Figure 4.16. Twenty locations are analyzed to obtain the temporal oscillation. Locations 1 to 20 represent the distance from 0.45mm to 9mm from the left edge of the image to the nozzle outlet. The developed temporal spray structures of 0% to 80% glycerol-water mixture are showed in Figure 4.17. It can be clearly observed that the spray structure becomes smoother with the increase of the fluid viscosity. Because there is no regular surface wave structure observed for fluids with less than 60% glycerol, this study only focuses on more viscous fluids, from 62% to 72% glycerol-water mixtures.

The spatiotemporal diagrams for these experimental fluids are illustrated in Figure 4.18 at different times after the start of the dispensing process. It is seen that the surface wave characteristics can be clearly observed from the post-processed images. Since the liquid viscosity plays an important role on the spray atomization process and the surface wave growth rate, the figures are selected at different time periods for different viscous fluids investigated in the present work. Because this clearly observed wave only occurs at a certain time for a certain fluid. Table 4.3 summarizes the specified time corresponding to the spatiotemporal diagrams in Figure 4.18.

The method used to analyze the domain wave frequency on the spray cone surface is demonstrated in Figure 4.19. Once the wave edge is detected and transformed as a function of time, Fast Fourier Transform (FFT) was performed for this time function to calculate the fundamental frequency, which is scaled to the actual frequency. The image at Location 3 with a time period of 336.4ms to 348ms after the start of spray serves as a representative example to show how the edge is detected from a spatiotemporal diagram and how the function is constructed.

In Figure 4.20, 62% glycerol-water mixture is demonstrated as an example to show the relationship between the location and wave frequency. Five different time-period and ten locations were considered for this purpose. With the same viscosity, there is no change on wave frequency at different locations. The surface wave frequency decreases as the spray dispensing time increases, which indicates that waves with higher frequency are more influential on the instability at the early stage of spray dispensing and breakup processes.

Towards the end of the spray development, the wave frequency becomes small. There is an observable trend of surface wave frequency changing with time for fluids with different viscosities in Figure 4.21. Each frequency is an averaged value from ten different locations and five repeatable measurements. The regular surface wave occurs at the same time for different viscous fluids. As the viscosity decreases, the observed regular wave forms in a longer time. These results show that for a transient spray process, the surface wave instability depends on both the fluid properties and the physical dispensing process such as the fluid velocity and the chamber pressure. The instability of surface wave is critical to the atomization process. This also explains why it is easier for less viscous fluid to atomize when comparing with more viscous fluids of similar surface tension. The standard deviation of frequencies for each sample fluids in five repeatable measurements was found to be small, which proved the repeatability of the experiment.

4.7. Droplet size distribution

To investigate the atomization quality of trigger sprayers for fluids with different viscosities, the droplet size and size distribution were measured using a laser diffraction technique. For the measurements, fluids with 0-60% glycerol were used with a step of 10%. Fluids with higher glycerol concentration were not studied because these fluids could not generate enough atomization for the droplet size measurement. The standard operation procedure (SOP) for the SprayTec[®] system setup and measurement include 1) 5 KHz sampling rate for rapid measurement; 2) an external source trigger (the actuator); 3) 1000ms measuring duration; 4) 10 runs for each fluid at each location. For each fluid, 9 locations

were measured, including three locations in the horizontal direction, from 17.78 cm (7 inch) to 22.86 cm (9 inch) downstream from the nozzle with a step of 2.54 cm (1inch). Six positions tested in the vertical direction, from -7.62 cm (lower than nozzle) to 7.62 cm (high than nozzle axis) with a step of 2.54 cm (1inch). Since the refractive index of water ($n=1.33$) and glycerol ($n=1.47$) is different, an approximated linear formula was used to estimate the refractive index of the fluid mixtures,

$$n = \frac{n_1 V_1 + n_2 V_2}{V_1 + V_2} \quad (4-2)$$

The refractive indices for the mixtures are shown in Table 4.4. The SprayTec software can directly give the results of $Dv(10)$, $Dv(50)$, $Dv(90)$ and SMD (Sauter Mean Diameter, $D_{3,2}$). To illustrate the variation of droplet size with time, the time evolution of droplet sizes of $Dv(10)$, $Dv(50)$, $Dv(90)$, and SMD are discussed first using H7V0 (means horizontal 17.78cm and vertical 0 inch location) as an example, shown in Figure 4.22 to Figure 4.25. It is seen that these diameters change significantly with time. At the early stage and the ending stage, $Dv(10)$, $Dv(50)$, and SMD show large droplet diameters due to the observed poor atomization in the spray images. During the middle stage of the dispensing process, a local diameter peak is also observed. In general, higher viscosity fluids lead to higher values of $Dv(10)$ and $Dv(90)$. But SMD and $Dv(50)$ are quite similar for different fluids. The variation trend with time of $Dv(90)$ is very different from the other parameters. A general observation is that higher viscosity can lead to larger droplet size. The averaged SMD for different fluids at this location is shown in Figure 4.26. The time-averaged droplet

size distributions for different fluids at the location of H7V0 are shown in Figure 4.27. With the increase of fluid viscosity, the dominant diameter changes from a small value to a higher value. For some viscous fluids, a bi-mode size distribution is observed. This may explain that why the SMD increase with the increase of fluid viscosity. However, an important finding in the experiments is that the measured particle size and size distribution significantly depend on the location of the measurement. To illustrate this, the time-averaged particle size distributions and SMD data for different fluids at the Location H9V0 are shown in Figure 4.28. It is found that the size distribution has only one peak. This peak occurs at a larger diameter value than that of Location H7V0 for the same fluids. However, the averaged SMD shows very different trend. The SMD increases with viscosity for 0% to 30% glycerol-water fluids.

To compare the SMD at different locations, the data in the horizontal direction is shown in Figure 4.29 for Locations H7V0, H8V0 and H9V0. The trends for fluid viscosity effects on the SMD values are very different in these locations. However, for each fluid, it is seen that the droplet size first increases with the distance from the nozzle and then decreases. This is probably attributed to the collision among droplets, which can lead to droplet coalescence and secondary breakup. The dependence of SMD on vertical locations for different fluids is shown Figure 4.30. Again, at different locations, the effects of viscosity on the droplet size change significantly with locations. For the same fluid, it is seen that at a very high location, the droplet size is small near the edge of the spray plume. Then with the location moving down, the droplet size increases. And then it decreases again when the

location moving down further close to the other edge of the spray. These results reflect the complicated droplet interaction within the spray plume. With droplet collision, the initially atomized droplets can coalesce to form larger droplets in the downstream as the droplets travel. The averaged SMD over all locations for different fluids was illustrates in Figure 4.31.

4.8. Summary

In this chapter, the near nozzle region of a liquid spray from a swirl atomizer for fluids with different viscosities was investigated experimentally using a high speed camera with simultaneous measurement of the dispensing piston displacement. The results of displacement curves show significant effects of fluid viscosity on the transient liquid dispensing process. The spray cone angle was calculated for 0% to 80% glycerol-water mixtures to study the effects of fluid viscosities. Based on the experimental observations and calculated spray characteristics, it is confirmed that liquid viscosity has a significant effect on spray cone angle and breakup in swirl atomizers. Higher viscosity prevents fluid from forming a large cone, which results in smaller angles in the liquid cone formation. The breakup of high viscous fluid was found to be more difficult as compared to the less viscous fluid. The frequencies of the temporal waves at the spray cone surface were also calculated for the liquid mixtures with different viscosities. It was found that the wave frequency does not depend on the location on the liquid cone and the frequency decreases with time for all the fluids. Droplet size parameters and distribution in nine different locations were measured using laser diffraction technology.

4.9. Tables and figures

Table 4.1 The viscosity of glycerol-water fluid mixtures at 23 °C

Vol. Ratio of Glycerol	0%	10%	20%	30%	40%	50%	60%	70%	80%	90%
Viscosity (mPa-s)	0.94	1.31	1.89	2.85	4.53	7.83	13.87	29.94	79.49	251.84
Surface tension (mN/m)	72	71.14	70.28	69.42	68.56	67.7	66.84	65.98	65.12	64.26
Density (g/cm ³)	1	1.026	1.052	1.078	1.104	1.13	1.156	1.182	1.208	1.234

3

Table 4.2 Mean value of the spray cone angles

Vol. Ratio of Glycerol	Cone Angle (Degree)	Stand Deviation
0%	59.67	1.46
10%	56.39	0.74
20%	55.70	0.53
30%	55.17	0.74
40%	54.35	1.58
50%	50.74	2.19
60%	42.46	2.06
70%	40.98	0.73
80%	35.57	1.93

Table 4.3 Specified time period of wave frequency for different fluids

Vol. Ratio of Glycerol	Time period
60%	324.8ms - 464ms
62%	324.8ms - 464ms
64%	324.8ms - 464ms
66%	324.8ms - 452.4ms
68%	324.8ms - 429.2ms
70%	324.8ms - 394.4ms
72%	324.8ms - 371.2ms

Table 4.4 Refractive index for different fluid mixtures

Vol. Ratio of Glycerol	0%	10%	20%	30%	40%	50%	60%
Refractive index	1.33	1.344	1.358	1.372	1.386	1.4	1.414

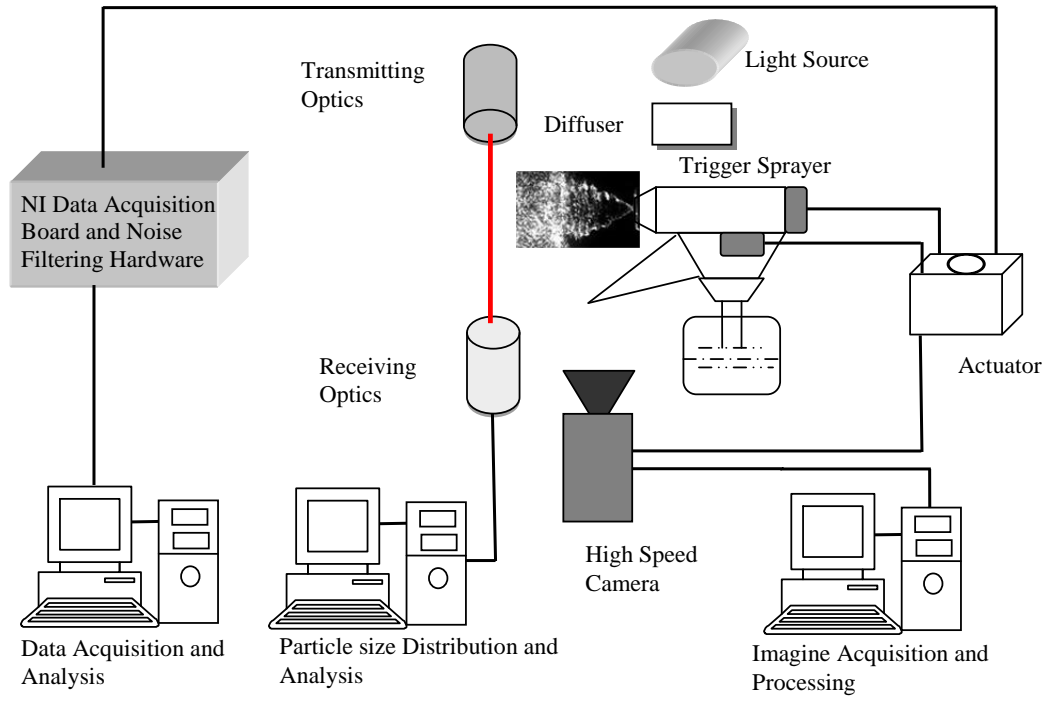


Figure 4.1 Schematic of the experimental setup

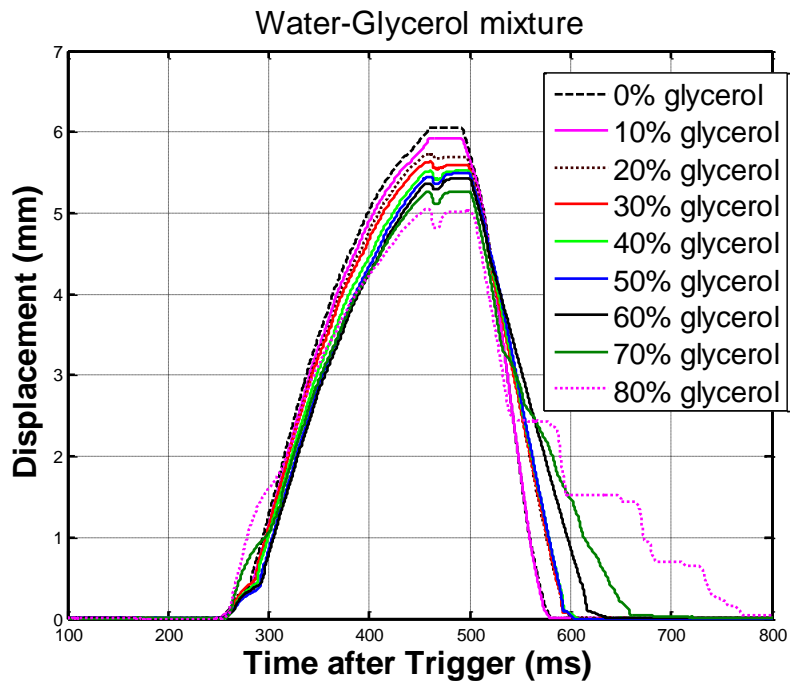


Figure 4.2 Transient dispensing piston displacements of different glycerol-water mixtures

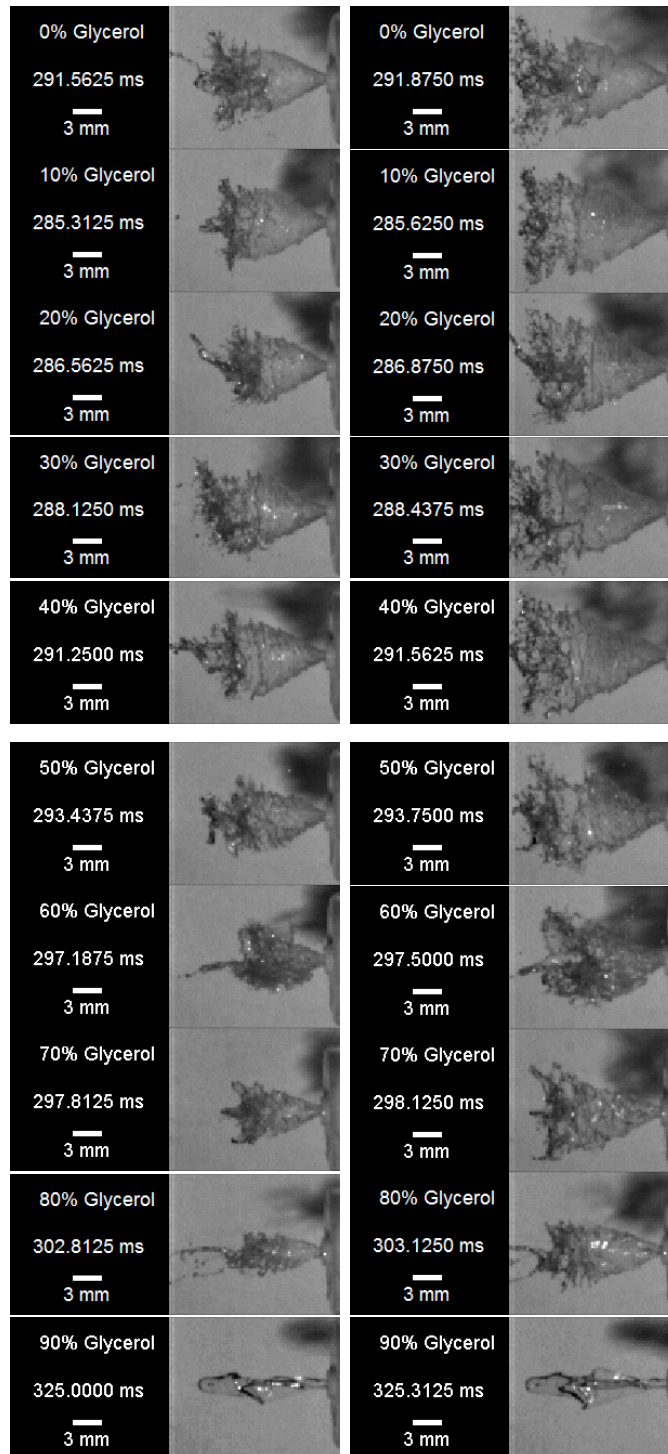


Figure 4.3 Start stage of spray development for different glycerol-water mixtures

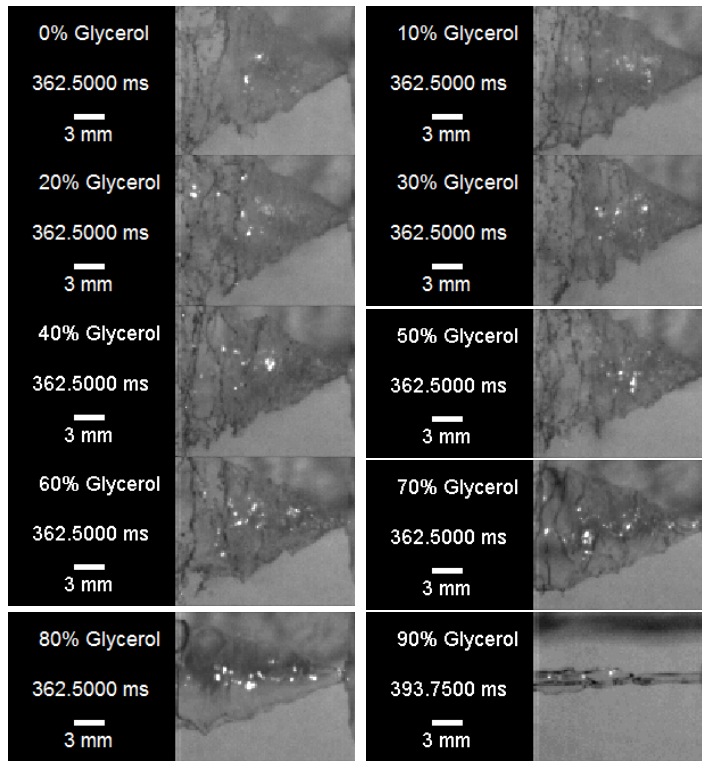


Figure 4.4 Developed stage of spray development for different glycerol-water mixtures

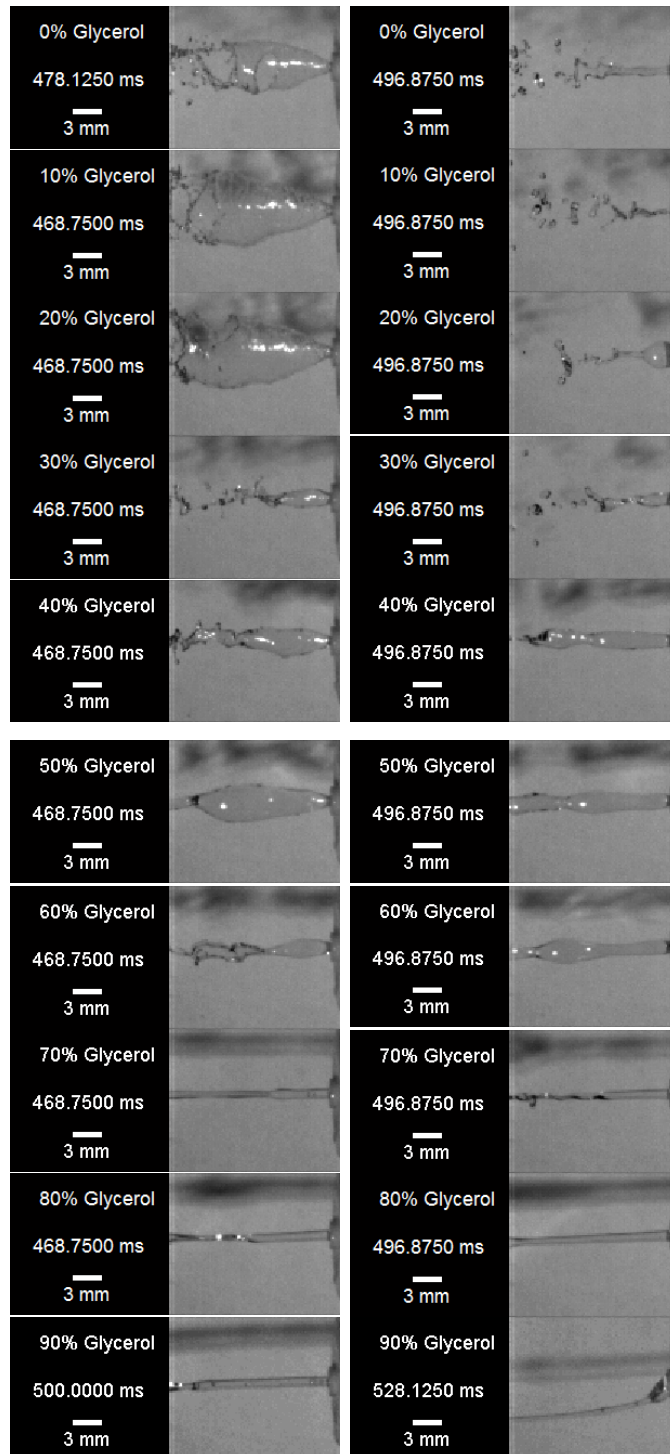


Figure 4.5 The ending stage of spray development for different glycerol-water mixtures

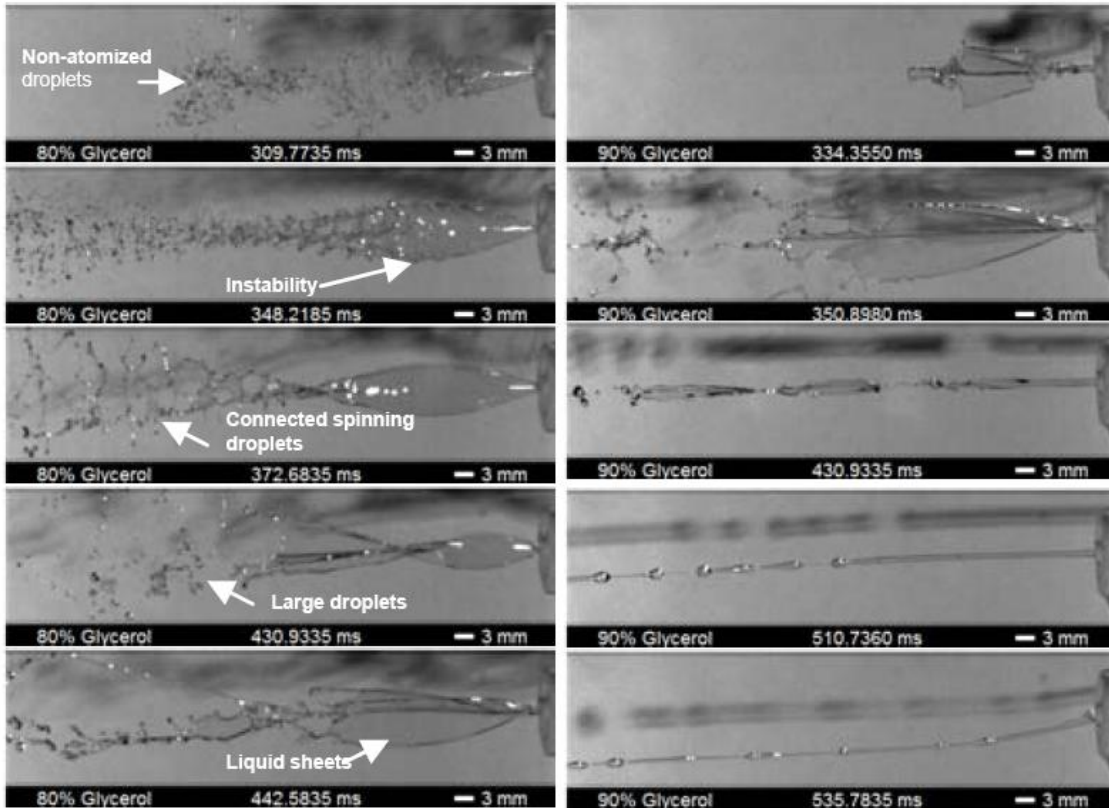


Figure 4.6 Spray structure of highly viscous fluids

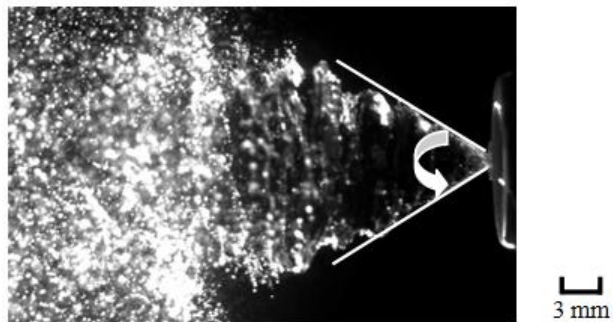


Figure 4.7 Global spray structure of the trigger spray and the calculated cone angle

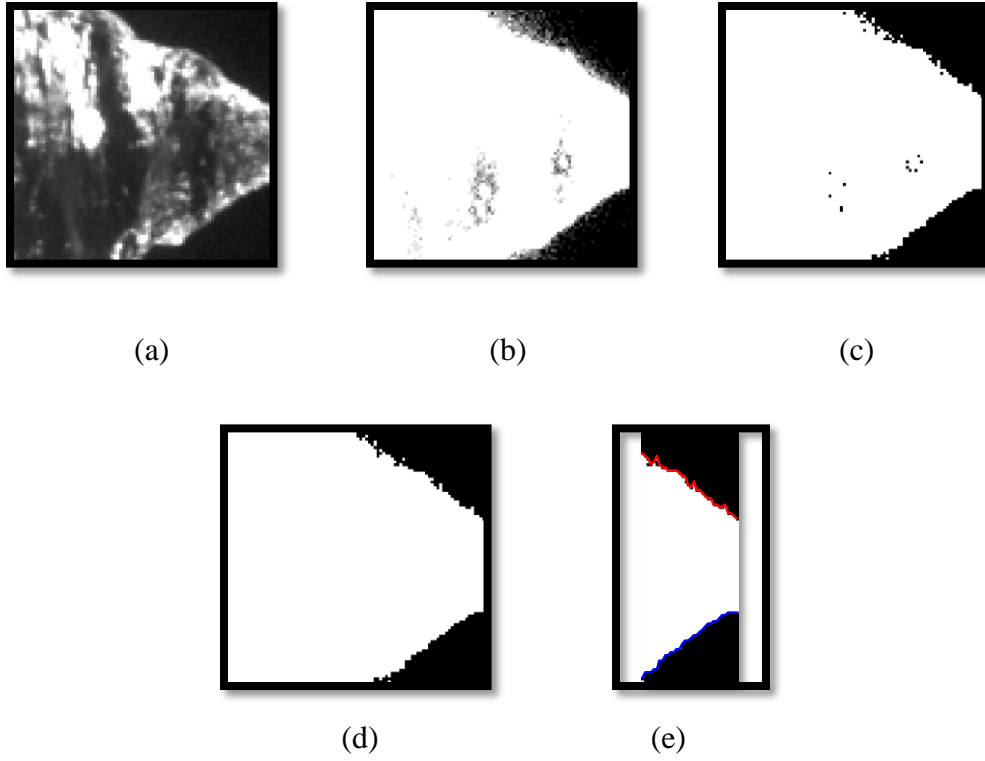


Figure 4.8 (a)-(d) The image processing steps. (e) Clear surface profiles obtained

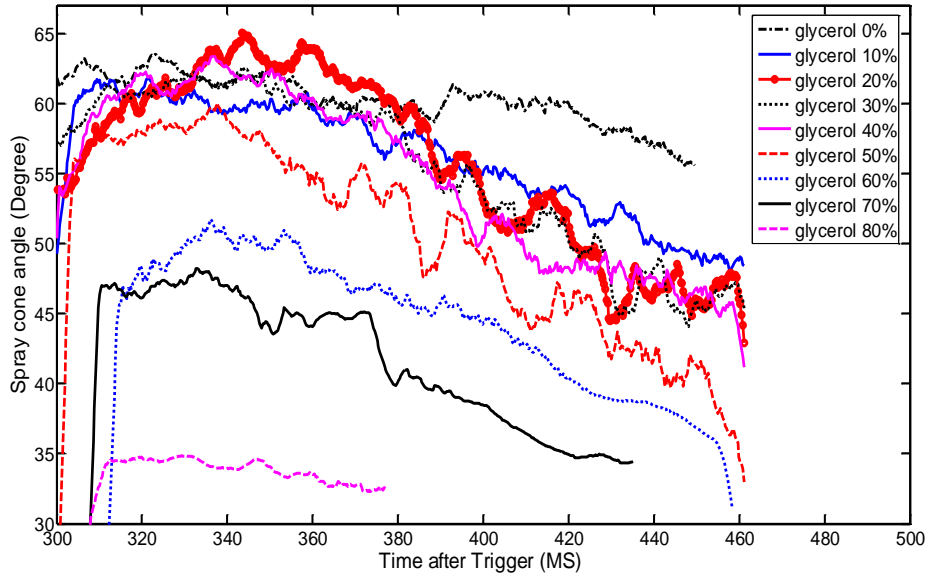


Figure 4.9 The transient changes of spray angle and mean value over time for 0% to 80% glycerol-water mixtures

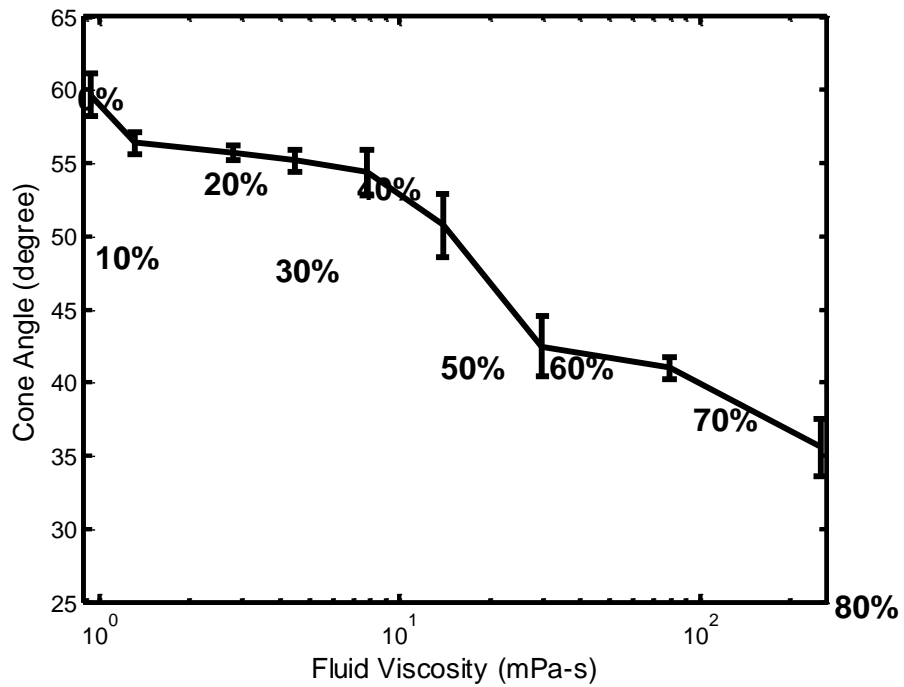


Figure 4.10 The calculated spray angle and the error bars for glycerol-water mixtures

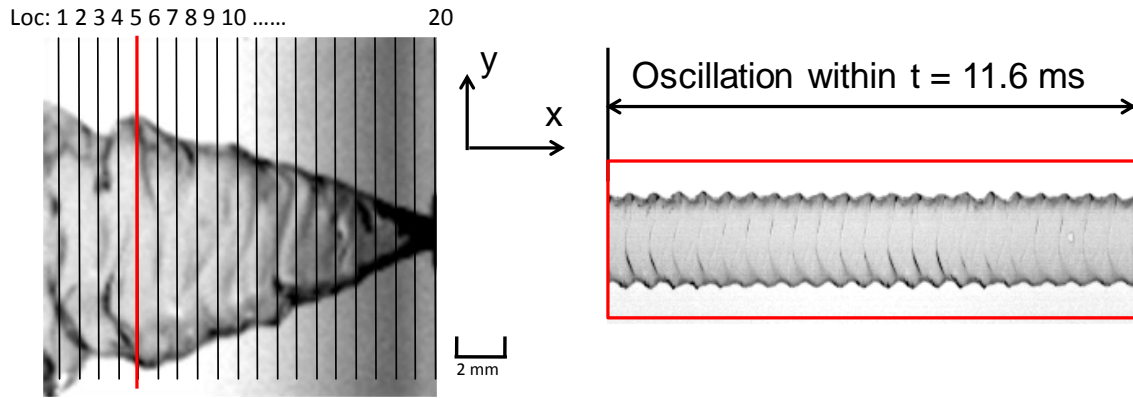


Figure 4.11 An example of spatiotemporal diagram for local frequency analysis

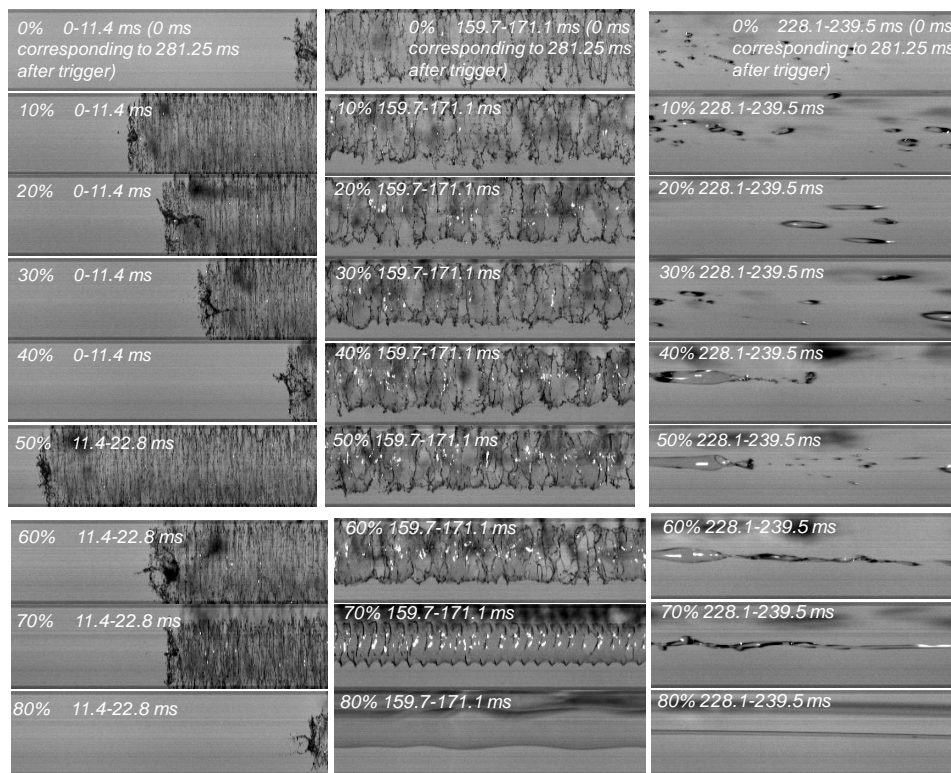


Figure 4.12 Spatiotemporal diagram at Location 1 for different fluids at starting, developed, and ending stage from the left to the right

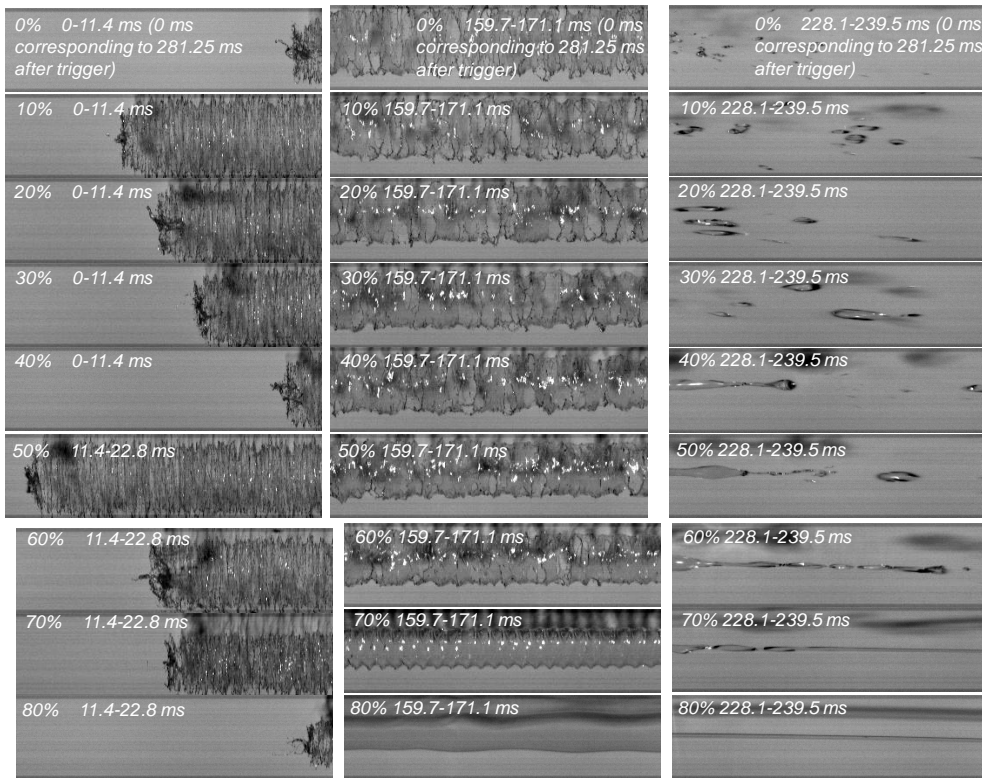


Figure 4.13 Spatiotemporal diagram at Location 2 for different fluids at starting, developed, and ending stage from the left to the right

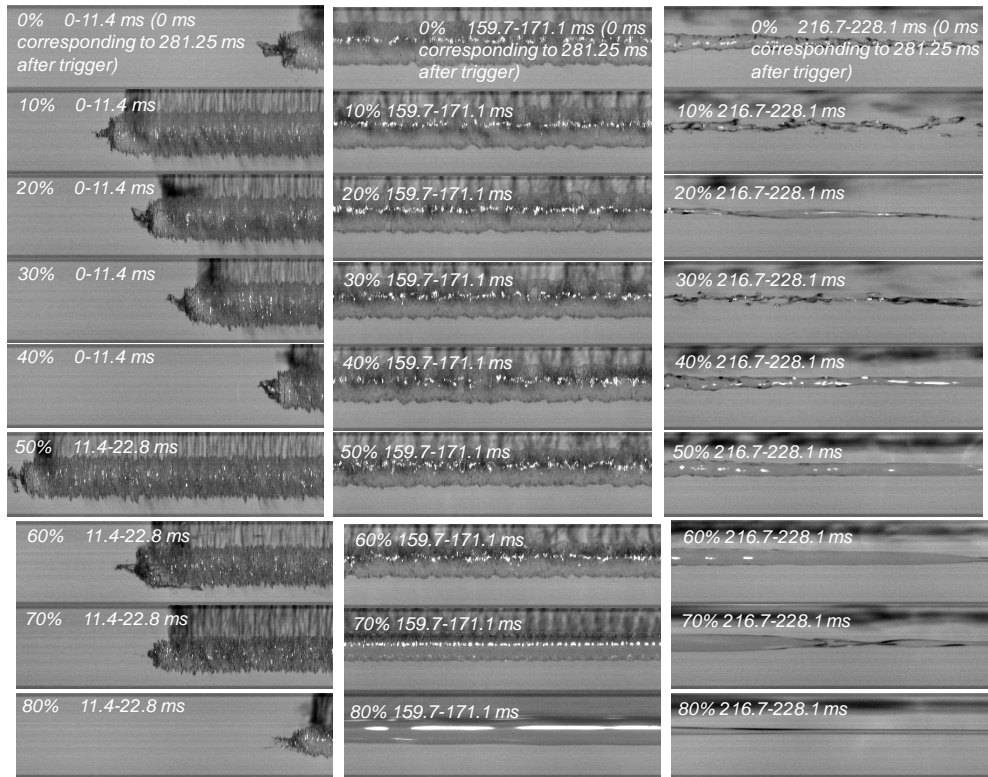


Figure 4.14 Spatiotemporal diagram at Location 3 for different fluids at starting, developed, and ending stage from the left to the right

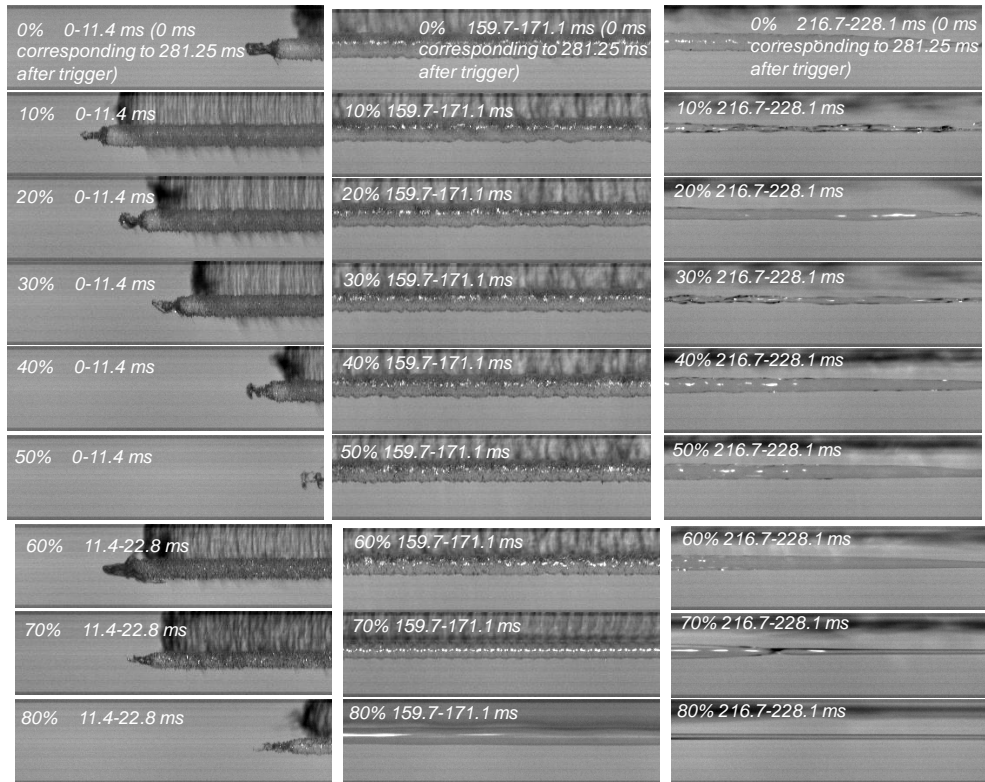


Figure 4.15 Spatiotemporal diagram at Location 4 for different fluids at starting, developed, and ending stage from the left to the right

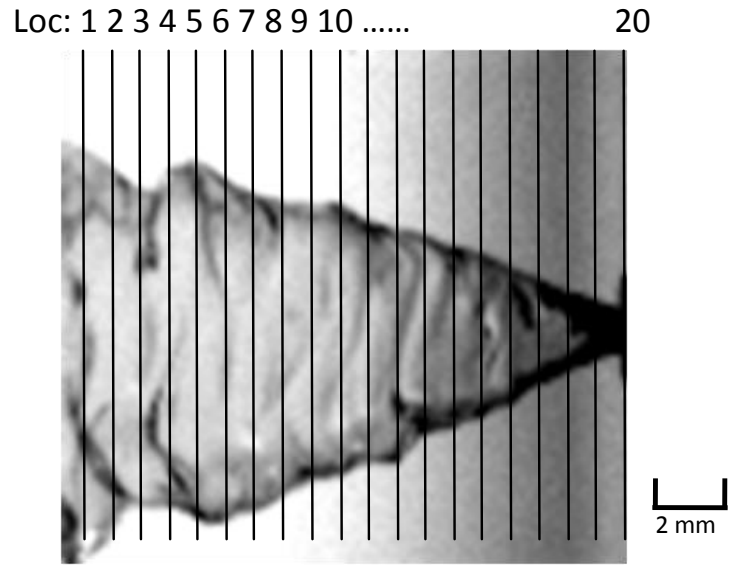


Figure 4.16 Discretized locations for surface wave analysis

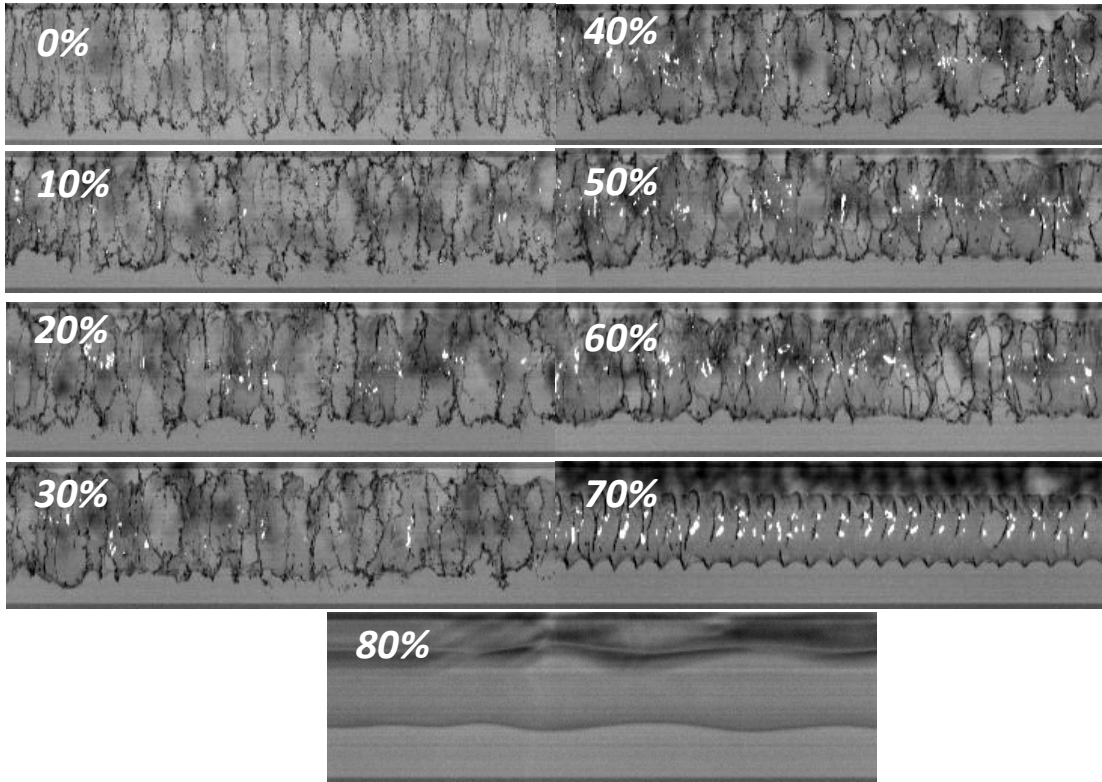


Figure 4.17 Developed temporal structure for fluid mixtures with different viscosity

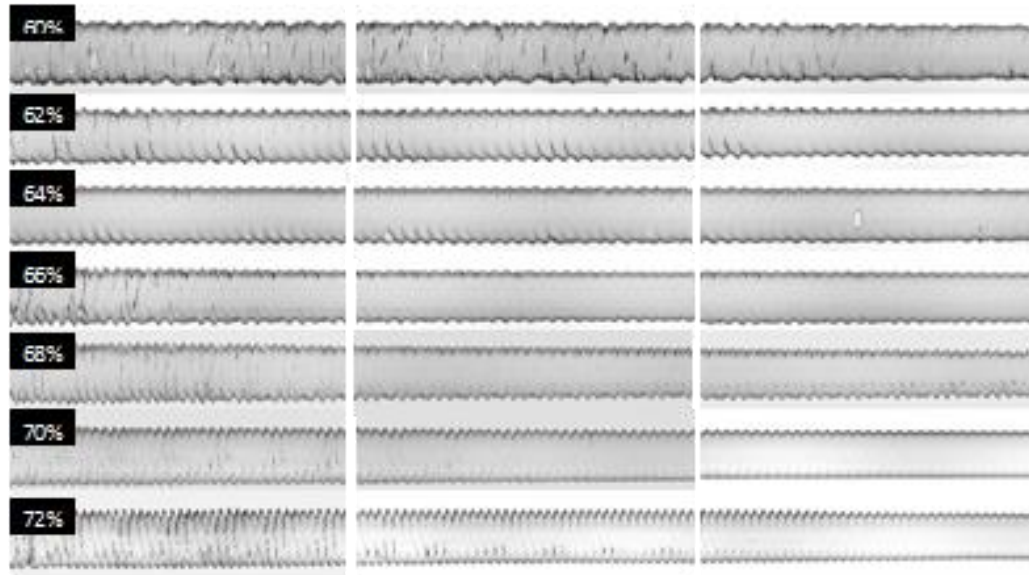


Figure 4.18. The spatiotemporal diagrams for different viscosity fluids at Location 6 at different time period

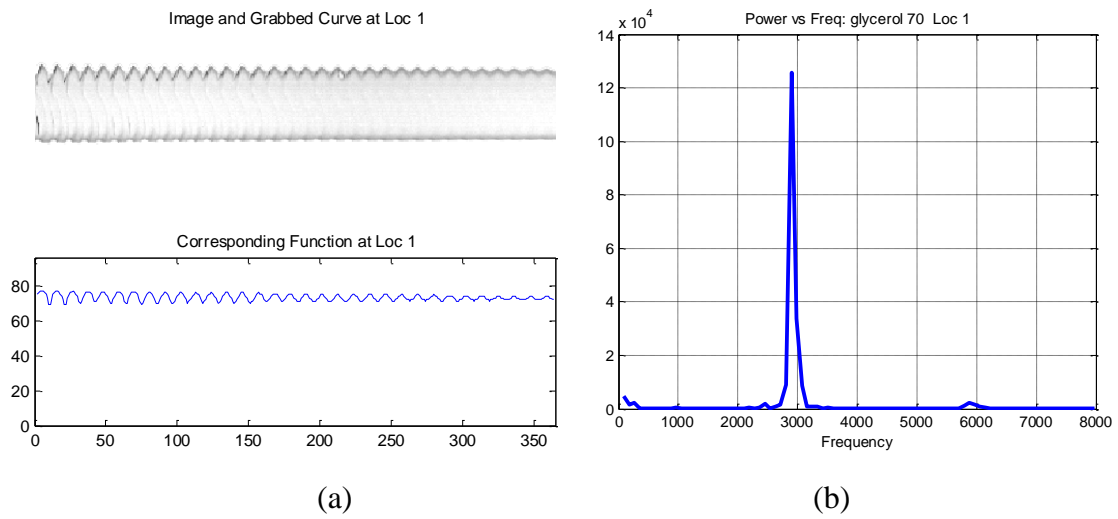


Figure 4.19 (a) A typical detected edge on the original image of 70% glycerol at Location 1 with a time period of 394.4~406ms (b) Fast Fourier Transformation to calculate wave frequency

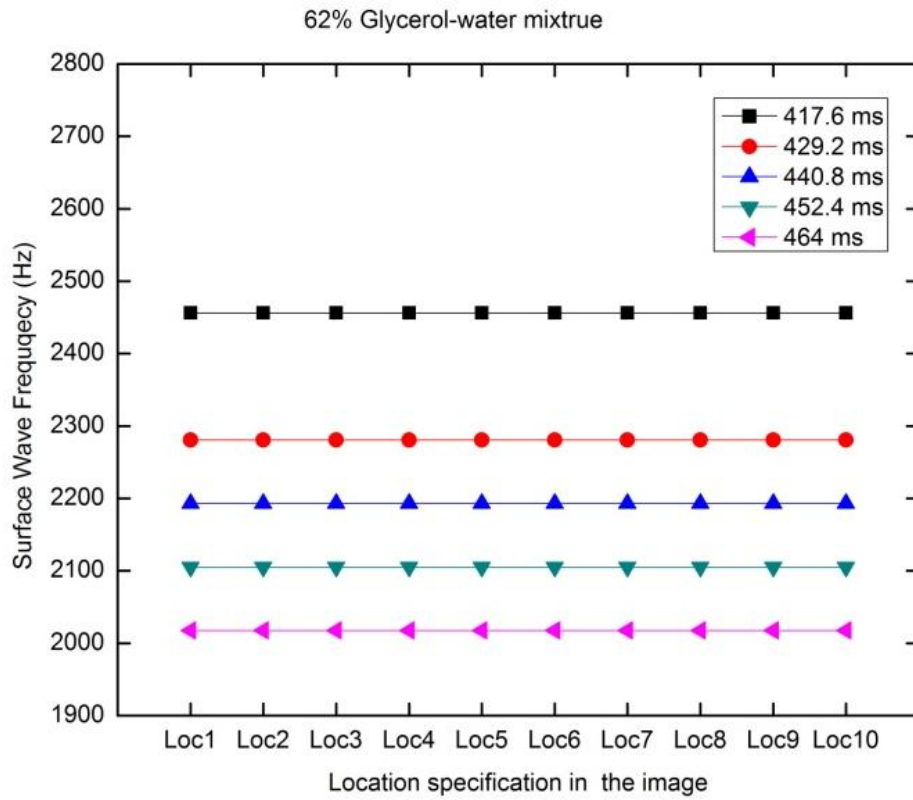


Figure 4.20 Surface wave frequencies at different location for different time period

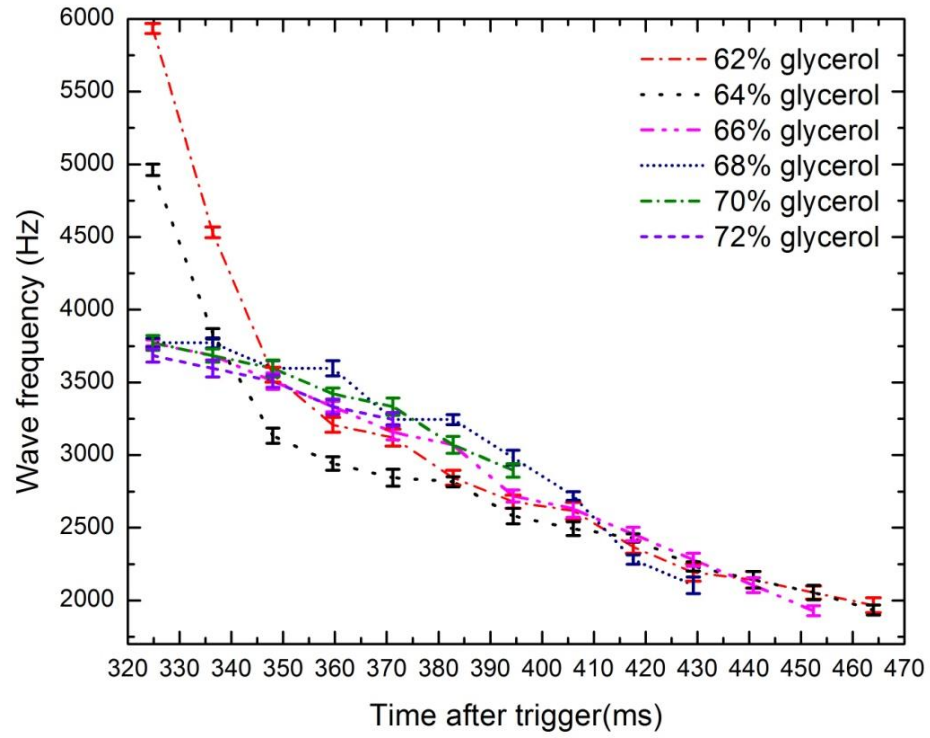


Figure 4.21 Wave frequency with standard deviation for the five repeatable measurements

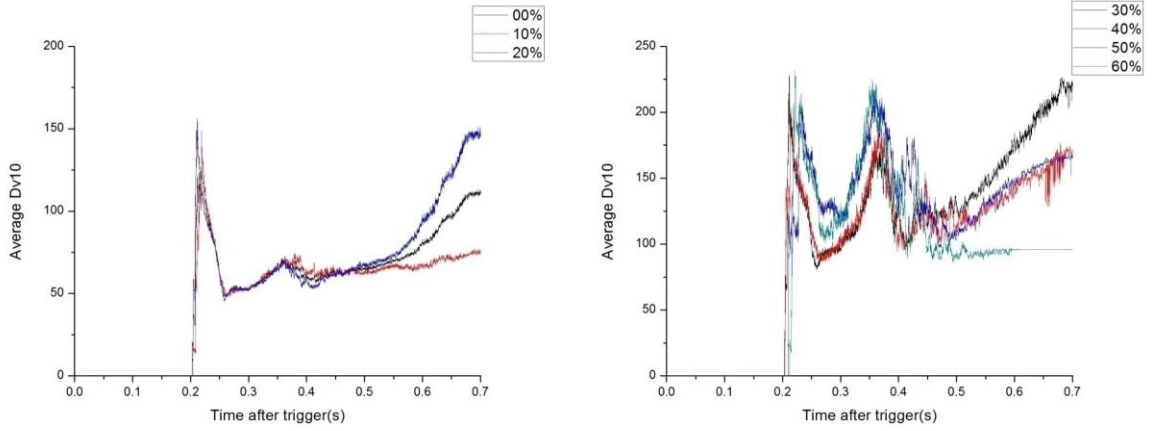


Figure 4.22 Dv(10) for different fluids at Location H7V0

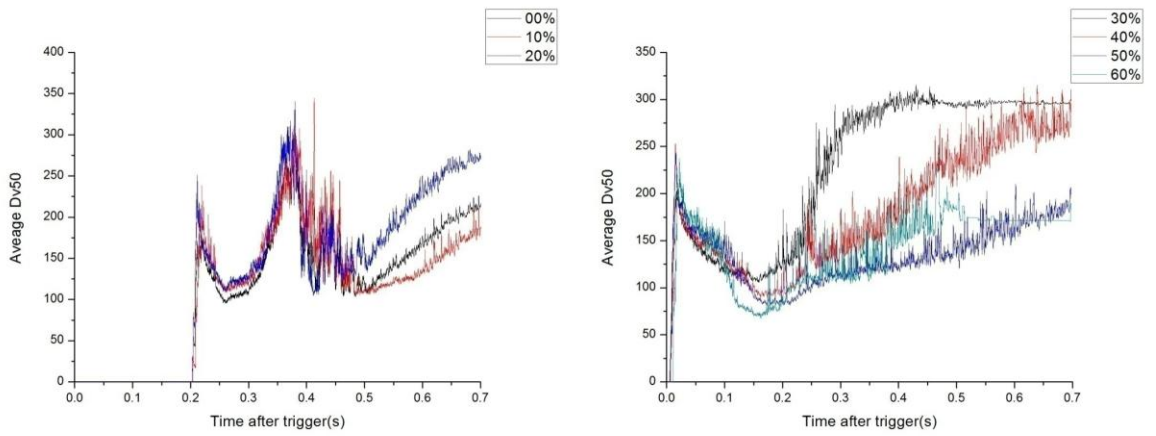


Figure 4.23 Dv(50) for different fluids at Location H7V0

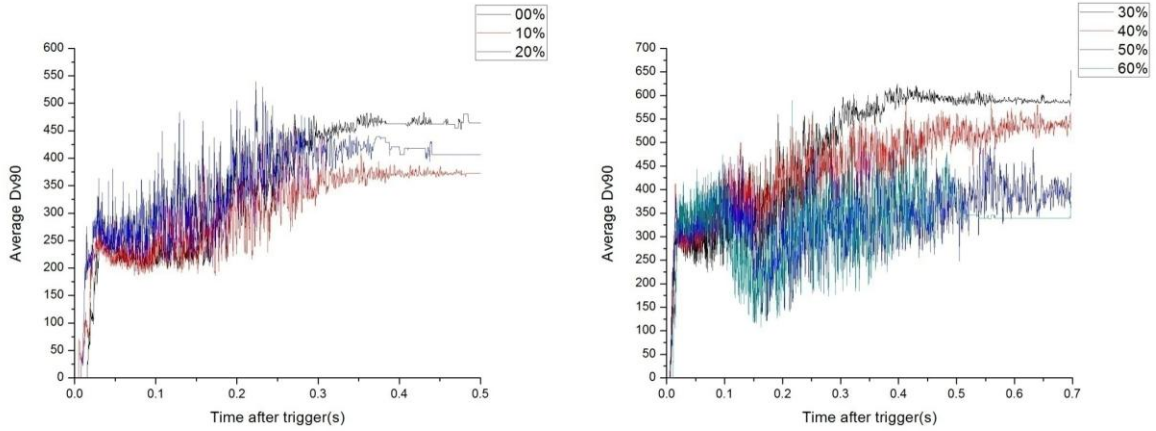


Figure 4.24 Dv(90) for different fluids at Location H7V0

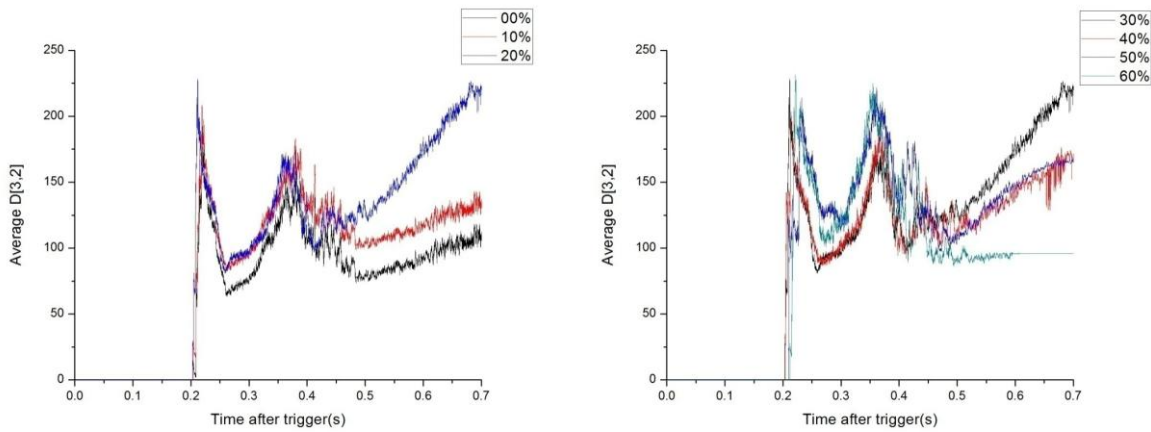


Figure 4.25 SMD for different fluids at Location H7V0

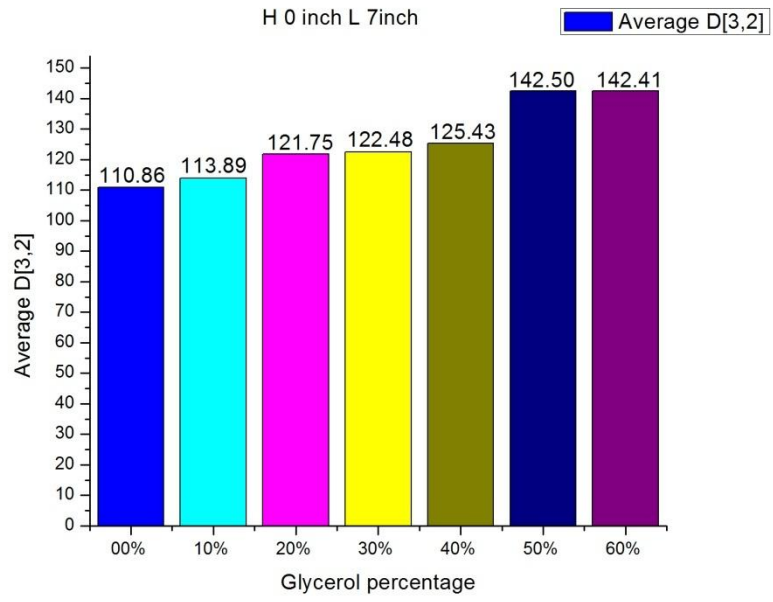
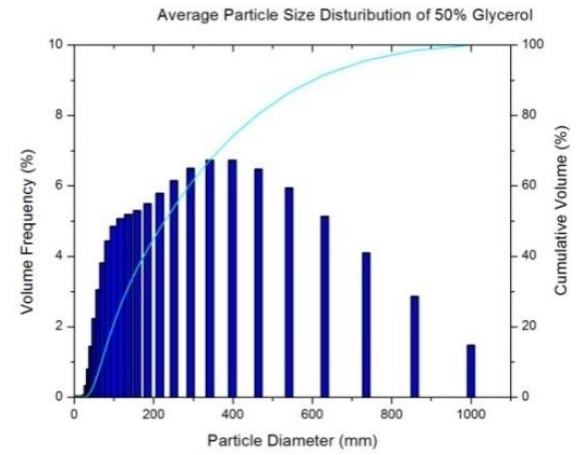
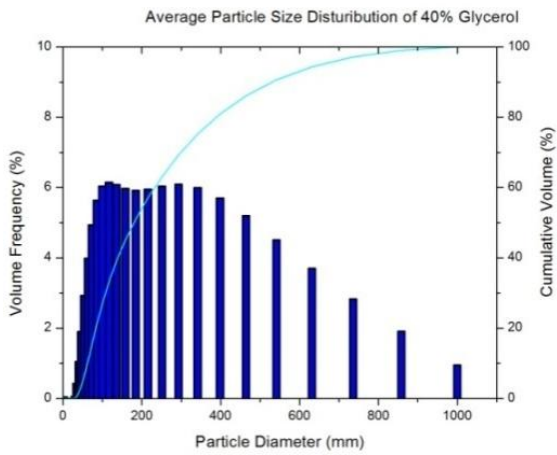
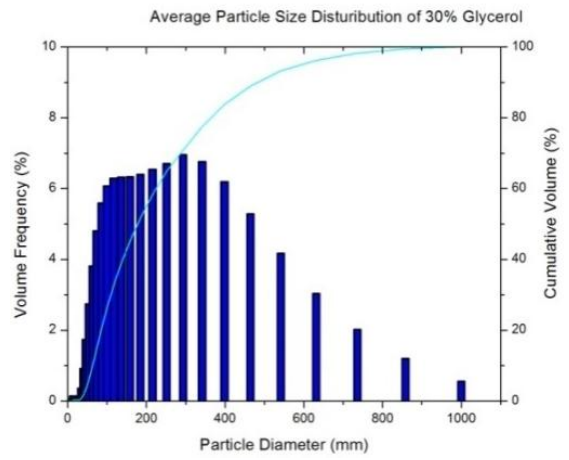
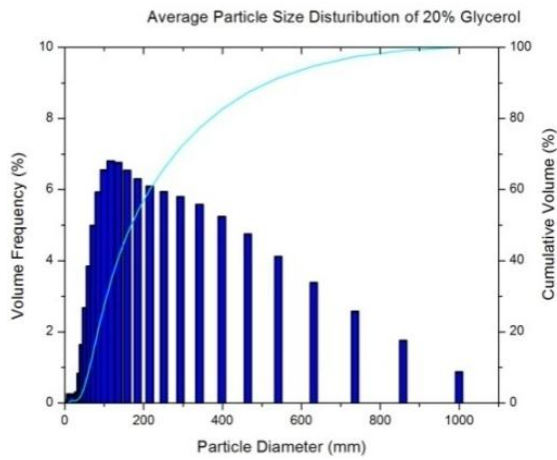
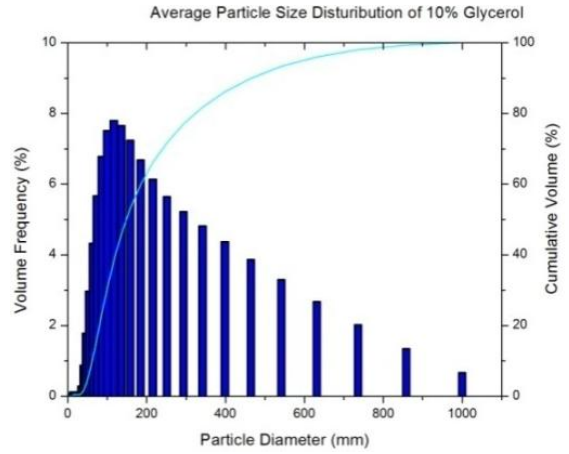
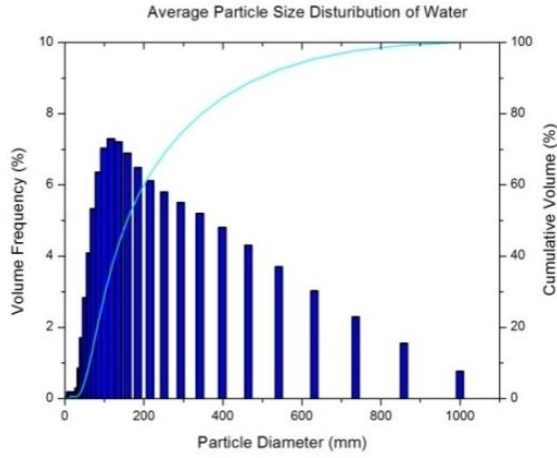


Figure 4.26 The averaged SMD for different fluids at Location H7V0

Figure 4.27 The time-averaged droplet size distributions for different fluids at H7V0



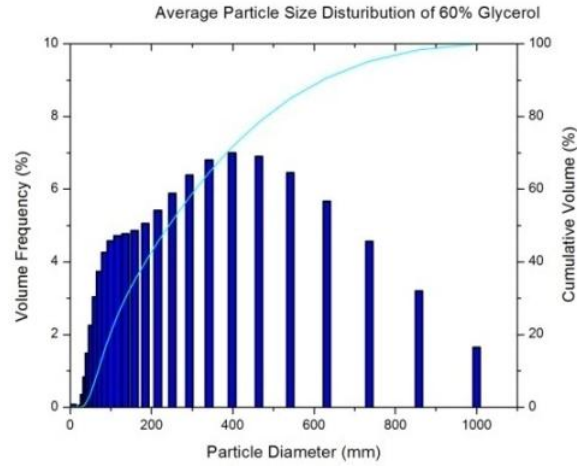
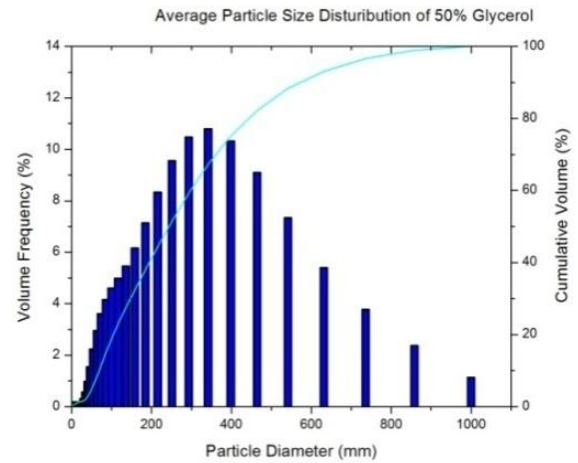
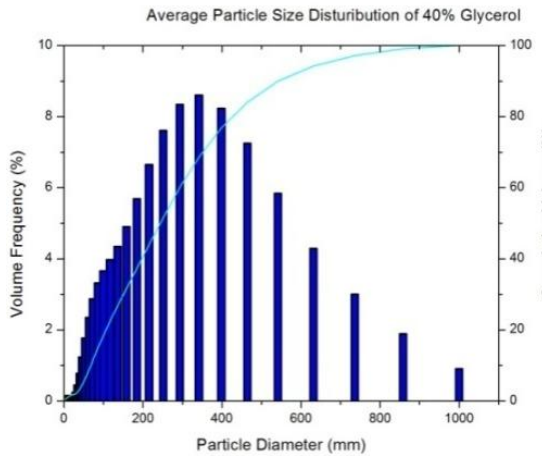
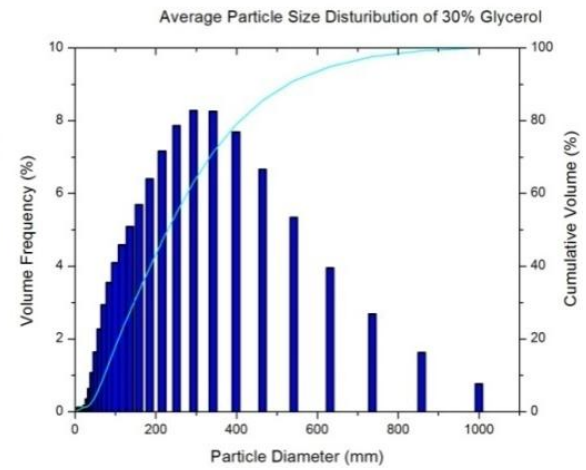
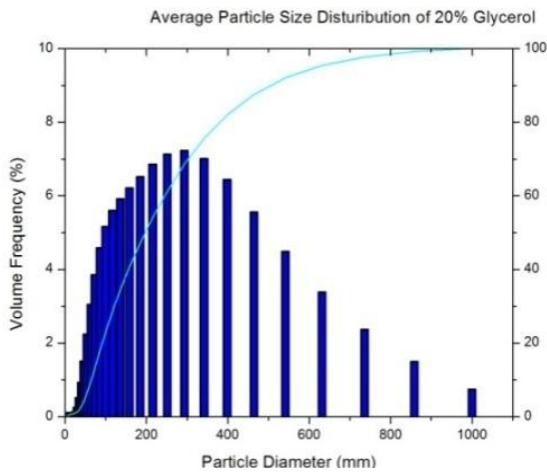
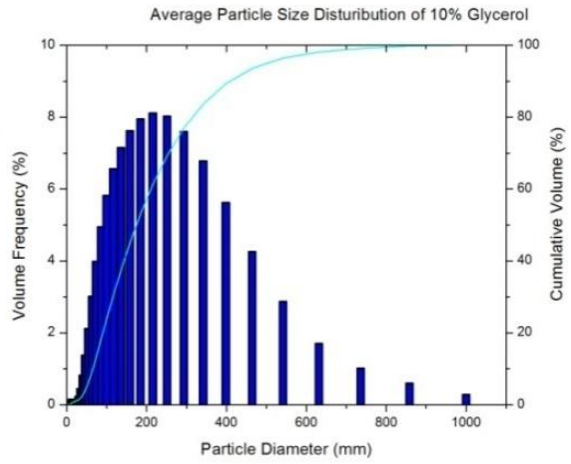
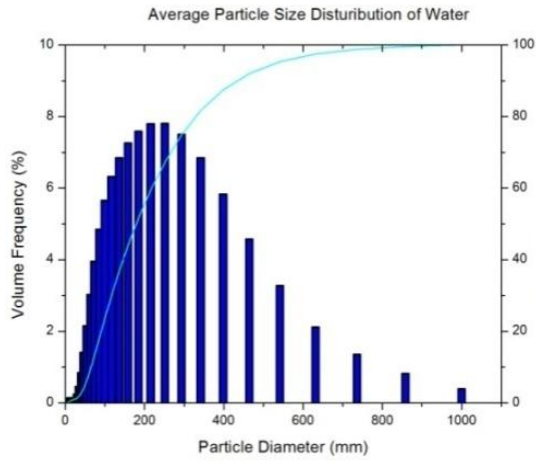
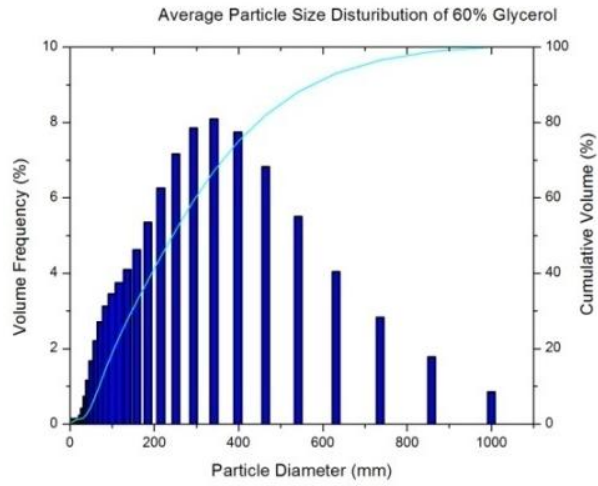


Figure 4.28 The time-averaged droplet size distributions for different fluids at H9V0





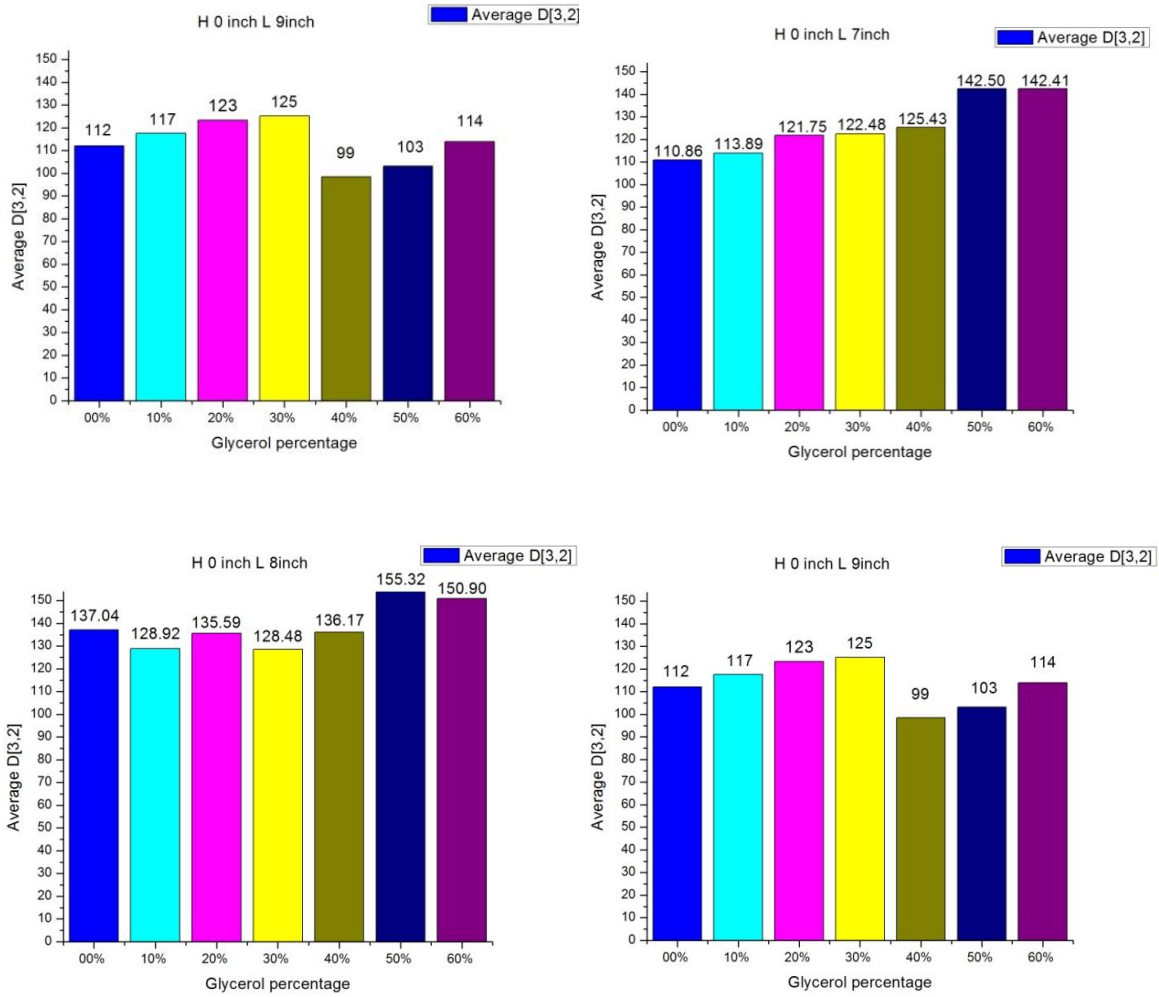


Figure 4.29 The time-averaged SMD for different fluids at different locations from top to bottom: H7V0, H8V0, and H9V0

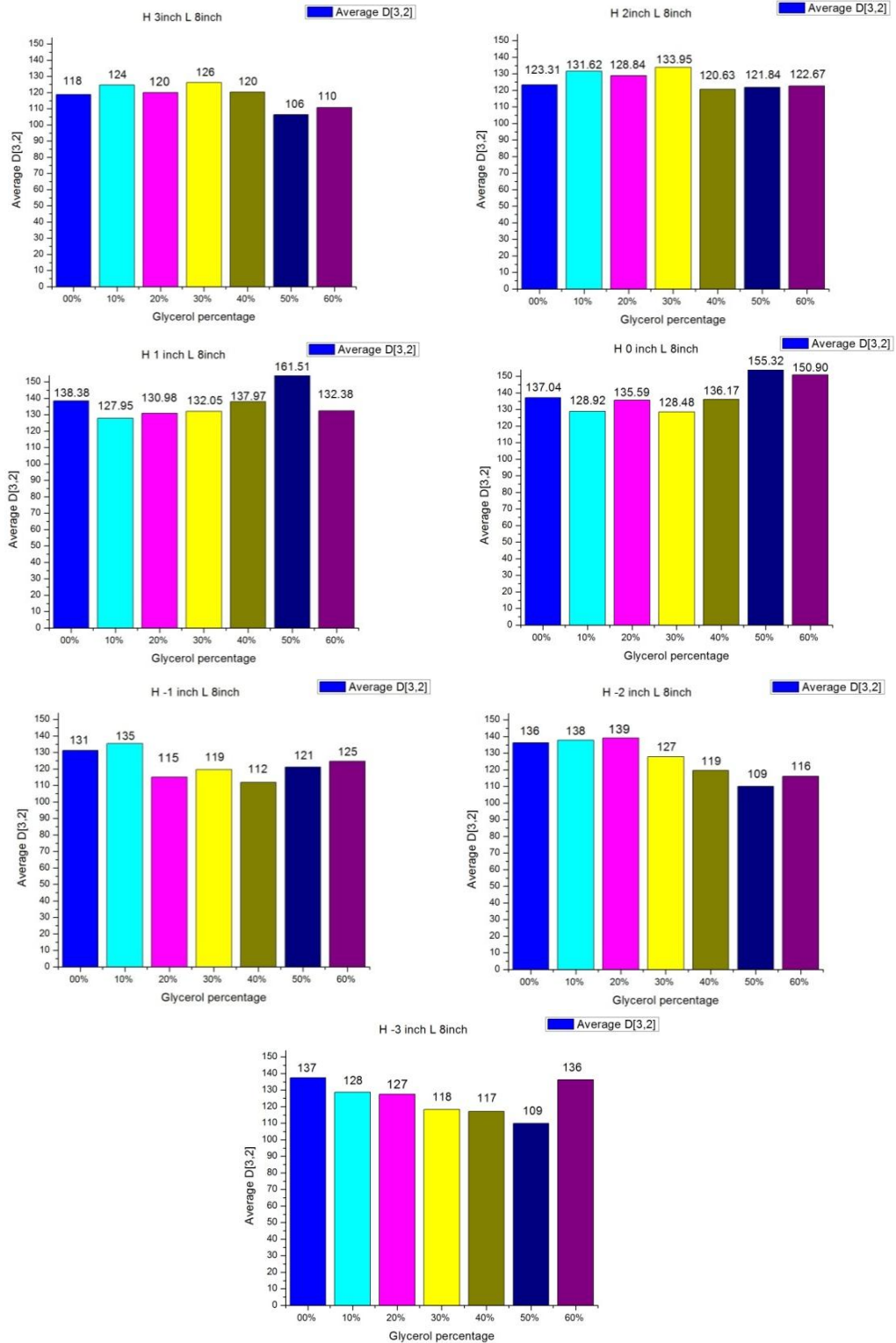


Figure 4.30 The time-averaged SMD for different fluids at different vertical locations

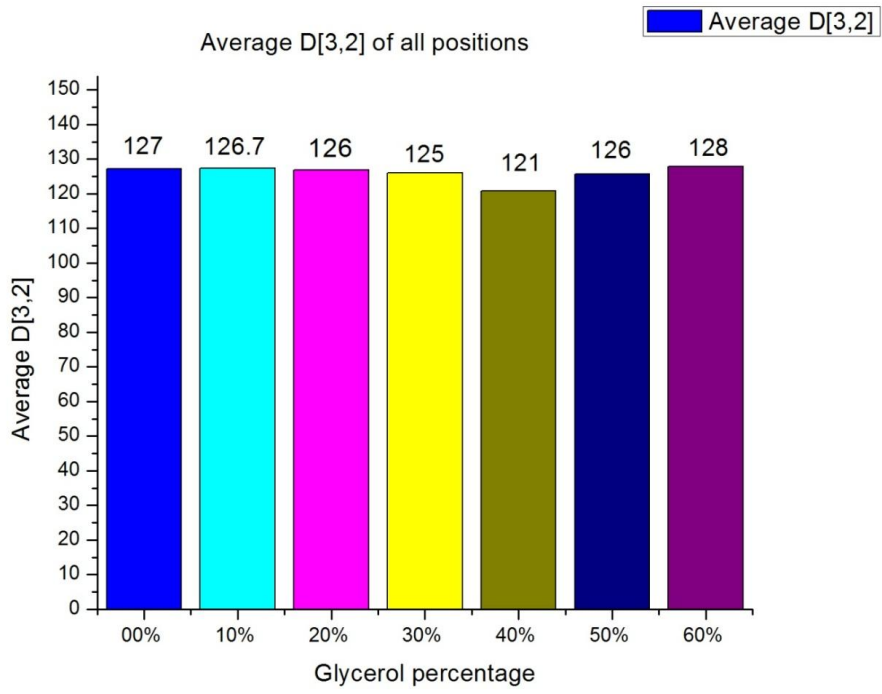


Figure 4.31 The averaged SMD over all the locations for different fluids

5. EXPERIMENTAL STUDY ON ETHANOL-WATER MIXTURES

5.1. Introduction

The key factors that affect the spray characteristics include the fluid viscosity, surface tension, and density. In the previous chapter, the effect of fluid viscosity on the spray structure, spatial and temporal instabilities on surface wave and droplet size were investigated. The spray cone angle was also studied using high speed imaging technology. The spray cone angle produced by pressure swirl atomizers is of particular importance in their applications to trigger sprayers, because the spray angle exercises a strong influence on atomization performance. During the transient fluid dispensing process from the appearance of liquid at the nozzle exit to the fully developed spray, the injected fluid accelerates from zero to its steady state velocity. Similar phenomena are seen during the spray shut-off process when the dispensing piston in the trigger sprayer reaches its maximum stroke. In the last chapter, spray cone angle and breakup length were considered as functions of liquid viscosity. Spray angle decreases as the liquid viscosity increases, while the breakup up length increases with viscosity. It was demonstrated that fluid viscosity has a significant influence on the near nozzle spray structure and breakup length.

The focus of this chapter is to provide a further understanding on surface tension effect using ethanol-water mixtures. These mixtures have very different surface tensions while with minor changes in viscosity and liquid density (Table 5.1). Due to the low boiling point of ethanol, it is expected that evaporation may also contribute to the breakup and atomization. Experiments were conducted to analyze the spray structure in the near nozzle

region using a high-speed camera. The near-nozzle and global spray structures were both visualized. The spray features, such as spray structure, cone angle, and breakup length were calculated and analyzed. Then the atomization of these sprays during the transient dispensing process was measured using a laser diffraction technique. The percentiles diameter parameters, Sauter Mean Diameter (SMD), and particle size distribution were measured and analyzed for the fluid mixtures at different spray locations.

5.2. Experimental system and techniques

5.2.1. Experimental setup

The same experimental setup in Figure 5.1 is used for this experiment. An electronically controlled actuator was used to press the trigger of a sprayer to initiate the liquid dispensing process. The use of the actuator improves the repeatability of the experiments. In order to synchronize the actuation process with the high speed imaging process, the high speed camera is controlled by a triggering pulse from the sprayer actuator. Similarly, the droplet size measurement system (SprayTec[®] from Malvern Instruments Inc.) is also triggered by the same pulse during the transient operation of the atomizer in the trigger sprayers. The pressure swirl atomizer inside the sprayers has a 1.0mm diameter nozzle and three tangential inlets in the swirl chamber.

5.2.2. Fluid samples

As mentioned before, the focus of this chapter is to investigate the effect of liquid surface tension on spray characteristics. As such, the working fluids with different surface tension values were prepared by mixing distilled water with ethanol at different volume

ratios from 0% to 100% by volume with a step of 10% (total 11 fluid mixtures). The experiment temperature was maintained at the room temperature (21 °C=294K). The fluid surface tension, viscosity, and density values are listed in Table 5.1 for the mixtures. Because the changes on fluids viscosities and density are relatively small, the effects of viscosity and density on the spray characteristics and atomization are expected to be minor. However, the surface tension of these mixtures covers a wide range from 72.75 mN/m to 22.27 mN/m. Therefore, its effect on the spray characteristics should be dominant.

5.2.3. Spray visualization

A high speed imaging technique was used to visualize the spatial spray structure in the near-nozzle region during the liquid dispensing process. Images of the near-nozzle region spray were acquired using a Phantom V4.3 digital high-speed CCD video camera. A 1000W light source and a light diffuser were used at the backside of the spray to maintain the uniformity of the light illumination. The high speed imaging process was synchronized with the dispensing process by an external trigger signal from the trigger sprayer actuator. The camera resolution was adjusted to obtain a compromise between frame rate and image resolution. Two sets of spray images were taken in this work. One set was the near nozzle spray images used for cone angle calculation. The other was a global nozzle spray images for breakup length measurement. The near nozzle spray images were captured with 32000 frames per second and an exposure time of 7 microseconds, which was short enough to “freeze” the transient spray motion. The image resolution was 112×96 pixels, corresponding to a near nozzle region of 9mm×7.7mm. The spray cone angle was calculated based on these

images. The global spray images were captured with 21000 frames per second and an exposure time of 6 microseconds. The image resolution was 112×192 pixels, corresponding to a near nozzle region of $9\text{mm} \times 15.4\text{mm}$. The breakup length was calculated based on the global spray images. There were five runs for each case.

5.2.4. Transient droplet size measurement

Characterization of the droplet size and distribution is important to quantify the atomization quality of atomizers. The laser diffraction technique is a useful technique for such measurements, especially for the transient spray process in the present study. In this work, a laser diffraction technique was used to measure the droplet size and its distribution for different fluids at different locations during the transient dispensing process. The equipment was a SprayTec[®] particle size analyzer from the Malvern Instruments Inc., which is able to achieve up to 10kHz sampling rate for transient spray analysis. The schematic of the measurement system is the same as illustrated in Figure 4.1. In order to easily change the location of the laser beam relative to the sprayer nozzle, a translational stage was used. The whole spray actuation system was installed on the translational stage. The SprayTec particle analyzer system was triggered by the triggering pulse from the actuator. A sampling rate of 5kHz was used for rapid measurement. The measuring duration was 1000ms. For each fluid, nine locations were measured, including three locations in the horizontal direction, from 17.78cm to 22.86cm downstream from the nozzle with a step of 2.54cm. Six positions tested in the vertical direction, from -7.62cm (lower than nozzle) to 7.62cm (high than nozzle axis) with a step of 2.54cm. There were 10 runs for each fluid at each location.

5.3. Near nozzle spray structure

Because the near nozzle region is critical to the liquid breakup and atomization for the downstream sprays, the development processes of the sprays in this region were investigated in more detail from the spray images, namely the starting, developing, and ending stages, as shown in Figure 5.1 to Figure 5.3. In Figure 5.1, it is found that the spray cone is relatively smooth for pure distilled water. More surface wave structures begin to appear on the spray cone with more ethanol in the mixtures. For the pure ethanol fluid, the breakup is very fast. Because of the lower surface tension, the pure ethanol liquid sheet can easily become unstable. It is also found in Figure 5.1 that, at the starting stage the initial dispensed liquid does not have enough momentum with large liquid blobs seen in the spray images. This is due to the fact that the liquid sitting in the nozzle does not experience an acceleration process and is pushed out of the nozzle as the dispensing process starts.

The developed stage of the spray is illustrated in Figure 5.2. When the fluid leaves the nozzle, it forms a cone due to the swirl motion in the nozzle. The surface wave starts to propagate and grow spatially and temporally. As the cone-shaped spray travels downstream, the liquid sheet becomes thinner and the surface wave oscillation magnitude increases on the spray surface. When the sheet becomes sufficiently thin, the sheet begins to break up into small fluid ligaments and atomize into small droplets. The spray breakup length, which is defined as the distance between the nozzle outlet and the initial surface breakup point, is found to decrease as the ethanol volume ratio increases. In other words, liquid breakup becomes easier for fluids with lower surface tension. There are more surface wave structures

occurring for a fluid mixture with more ethanol, which increases the instability of the liquid sheet. The spatial and temporal instabilities are more profound for the liquid with lower surface tension. So the liquid sheet is easier to breakup into ligament, which further breaks up into smaller droplets.

The spray images near the ending stage of the fluid dispensing process for different fluids are shown in Figure 5.3. Near the end of the fluid dispensing process, the spray cone continues to shrink and collapse back to an onion shape due to the lower fluid velocity. The onion shade spray leads to large droplets in this stage. This may be responsible for the poor atomization near the end of the spray. When the volume ratio of ethanol in the mixture is small, the spray cone is very smooth compared to the liquids with higher ethanol concentrations. The surface waves are still observable for liquids with low surface tension at the ending stage. This indicates they have the potential to further breakup.

5.4. Spray cone angle analysis

The spray cone angle was calculated based on the near nozzle spray images. Figure 5.4 demonstrates a representative spray cone angle of distilled water. The digital spray images were post-processed by a computer program for the computation of the spray cone angles. The time period used for cone angle calculation is from the initial dispensing process (at about 290ms) to the time when the piston reaches its maximum dispensing stroke (at about 460ms, when the fluid dispensing process is finished). The piston stays at its maximum stroke for a while and then the piston release process starts. There is no conical spray formed

after the fluid dispensing process is complete. The transient spray cone angle at each time was first calculated. Then the spray cone angle was averaged over the whole calculation period for each run. Figure 5.5 illustrates the average spray cone angles for different mixtures based on 5 repeated runs. The error bars represent the standard deviation over 5 repeated experiments. The averaged spray cone angle decreases as the liquid surface tension decrease from 0% to 100% ethanol in the mixtures. However, the cone angle only slightly decreases about 10.9 degree for the whole range as shown in Table 5.2 (from 57.71 degree for the pure water to 46.81 degrees for the pure ethanol). This indicates that liquid surface tension may have a minor effect on the formation of the near nozzle spray cone angle. As shown in the previous work [107], fluid viscosity plays an important role in controlling the fluid flow inside the swirl atomizer. The effect of surface tension becomes more profound only if there is interaction between the liquid and the ambient gas (namely air in this work). The spray cone angle at the exit of the nozzle is determined by the velocity components in the tangential and axial directions. The flow inside the nozzle before existing is only affected slightly by the introduction of the air core. Therefore, surface tension only has a minor effect in the near nozzle spray cone angle.

5.5. Breakup length analysis

The breakup length is measured as the length from the nozzle tip to the location where the first liquid ligament appears, as shown in Figure 5.6. The calculation is from the initial dispensing process (at about 290ms) to the time when the piston reaches its maximum dispensing stroke (at about 460ms when the fluid dispensing process is finished). During the

calculation period, the transient spray breakup length at each time was calculated. Then, the spray breakup length was averaged over the whole calculation period for each run.

Figure 5.7 shows the comparison of the measurements on spray breakup length for different fluid mixtures. Each result represents an average of 5 measurements with the standard deviation illustrated by the error bars. As the ethanol volume ratio increases, the breakup lengths become shorter from water to 50% ethanol-water mixture. For mixtures with even lower surface tension (i.e., higher ethanol volume ratio), the breakup lengths do not change too much. The values of the breakup length are listed in Table 5.3. It changes from 10.72 mm for pure water to 9.44 mm for pure ethanol. It is concluded that the surface tension may not have a significant effect on liquid breakup length. Similar phenomenon was also observed by Chinn [108]. When considering the air core in a swirl atomizer, the overall effect of surface tension on the size of the air core is minimal. The surface tension effects on the surface of the air core of a swirl atomizer can be safely be ignored. Thus the surface tension is not a critical factor on liquid breakup length comparing with liquid viscosity [109, 110]).

5.6. Droplet size measurements

5.6.1. Percentiles parameter and Sauter Mean Diameter

To illustrate the variation of droplet size, Figure 5.8 (a)-(c) show the averaged value of the droplet size with the percentiles parameters of $D_v(10)$, $D_v(50)$, and $D_v(90)$. $D_v(\#)$ means the particle size below which volume percentage (#) of the spray droplets. The notation of L_xH_y (x means horizontal distance from the nozzle in inch, y is the vertical

location in inch, and a negative value of y means the laser beam is below the nozzle axis) is used to show different locations between the nozzle tip and the laser beam in the figures. From Figure 5.8, it is seen that these diameters change with locations. But the trend is not very clear from the plots in Figure 5.8. The variations of $D_v(50)$ and $D_v(90)$ among different locations become smaller with increasing ethanol ratio. The average values of $D_v(10)$, $D_v(50)$, and $D_v(90)$ over different locations have a similar trend indicating that as the surface tension decreases their values become smaller. This means it is easier to breakup and atomize for liquid mixtures with lower surface tension.

The Sauter Mean Diameter (SMD) is the averaged values over 10 repeated runs. The comparison of different working fluids at different locations is shown in Figure 5.9 to Figure 5.10. The averaged SMD in the same horizontal location and different vertical locations is shown in Figure 5.9. The results demonstrate that SMD decreases with ethanol ratio increases. Relatively large droplets are observed at the L8H2 location for 0 to 30% fluid mixtures. For the same fluid, it is seen from the results that at a higher location (L8H3), the droplet size is small near the edge of the spray plume. With the location moving downwards, the droplet size increases, and then decreases again when the location moves down further close to the other edge of the spray plume (L8H3). These results again show complicated droplet interactions within the spray plume.

The dependence of SMD on horizontal locations for different fluids is shown in Figure 5.10. The droplet size changes with locations. The trends for fluid mixture effects on the SMD values are different at these locations. However, for each fluid, it is seen that the

average SMD value decreases with the increase in horizontal distance from L7H0 to L9H0. This is most likely affected by the collision among droplets in the upstream spray plume, which can lead to droplet coalescence. The values of the averaged SMD are listed in Table 5.4 and it changes from 125.7 μm for the pure water to 38.9 μm for the pure ethanol. The averaged SMD for different fluids clearly shows the effects of fluid properties on the atomization quality. For the pure ethanol fluid, the surface tension is much smaller than that of pure water. A linearly correlation between SMD and surface tension value was found for distilled water and ethanol. The SMD of ethanol is about one third of distilled water, and the surface tension value of distilled water is about three times of pure ethanol. In addition to the surface tension difference, another possible reason that causes the dramatic reduction in SMD is that the spray atomization process is transient. This transient process may result in droplets not having enough momentum to pass the laser beam and reduced the measured droplets numbers.

5.6.2. Particle size distribution

The particle size distribution with volume frequency is shown in Figure 5.11 and Figure 5.12 for different locations. The presented curves result from a mean value over 10 runs conducted for different working fluids. The particle size distributions at different vertical locations are compared in Figure 5.11. It is observed that for the same fluids, large droplets occur at the locations closer to the nozzle axis. Smaller particles are found at the locations further away from the nozzle axis in vertical direction. For fluids with lower surface tension, the peak values of the volume frequency shift toward smaller particle

diameters. The droplet size distributions in the spray plume appear relatively symmetric about the nozzle axis in the vertical direction. It can be seen that the variation of the measurement location affects the peak (maximum value) location in the particle size distribution curves, but the general shape of the curves do not change much with the location. It is found that the peak values of the particle size distribution curves shift to smaller diameter when the location moves away from the nozzle axis in the vertical direction.

Figure 5.12 illustrates the particle size distribution in different horizontal locations and the averaged particle size distributions over the 9 locations for all 11 fluid mixtures. As the location moves downstream, droplet size becomes smaller with less large particles shown in the size distributions. For the averaged particle size distribution over all locations (Figure 5.12 (b)), the peak location of the volume frequency percentage shifts for different fluid mixtures. With the increase in the volume ratio of ethanol, the large droplet distribution tails begin to disappear. The particle size distribution curves shift toward smaller droplet diameters. The effect of the gravity on the spray is also a possible cause that makes the particle size distribution sensitive to different locations.

5.7. Summary

In this chapter, the spray characteristics and atomization of a swirl atomizer were studied. Different fluids with very different liquid surface tension using ethanol-water mixtures (0-100% ethanol) were used as the sample fluids. The spray at near nozzle region was visualized by using a high speed camera. Particle size parameter and droplet size distribution were also measured for all the fluids at different locations within the spray plume

using a laser diffraction technique. The spray cone angle and breakup length were calculated for all the mixtures. Based on the experimental observations and calculated spray characteristics, it is found that surface tension does not have a major effect on spray cone angle and breakup length in swirl atomizers in the near nozzle region. Spray cone angle slightly decreases with the increase in ethanol volume ratio (about 10.9 degree decrease from pure water to pure ethanol). The breakup length is found to decrease slightly as ethanol volume ratio increases (about 1.28mm decrease from pure water to pure ethanol). However, surface tension has a significant effect on the particle size and distribution. The results show droplet size decreases with the increase of ethanol volume ratio. In addition, the location for size measurement also influences droplet size. Generally speaking, smaller droplet size is found for a location away from the nozzle axis in the vertical direction. In the horizontal direction, larger droplets are found for a location closer to the nozzle exit. Together with the conclusions drawn in the previous chapter, it is found that liquid viscosity has a significant impact on the primary breakup of spray ejected from swirl atomizer, but liquid surface tension is more influential to the secondary breakup of the spray.

5.8. Tables and figures

Table 5.1. Fluid properties for ethanol-water mixtures at 21°C

Vol. Ratio of Ethanol	0%	10%	20%	30%	40%	50%
Surface Tension (mN/m)	72.75	67.70	62.65	57.61	52.56	47.51
Viscosity (mPa-s)	0.937	0.951	0.964	0.978	0.992	1.006
Density (kg/m ³)	997	976.2	955.4	934.6	913.8	893
Vol. Ratio of Ethanol	60%	70%	80%	90%	100%	
Surface Tension (mN/m)	42.46	37.41	32.37	27.32	22.27	
Viscosity (mPa-s)	1.019	1.033	1.047	1.060	1.074	
Density (kg/m ³)	872.2	851.4	830.6	809.8	789	

Table 5.2 Average spray cone angles for ethanol-water mixtures

Vol. Ratio of Ethanol	0%	10%	20%	30%	40%	50%
Spray Cone angle (degree)	57.71	55.16	54.93	54.96	53.47	52.69
Standard deviation	0.45	1.20	0.40	0.53	0.63	0.45
Vol. Ratio of Ethanol	60%	70%	80%	90%	100%	
Spray Cone angle (degree)	51.01	49.41	47.80	47.60	46.81	
Standard deviation	1.24	0.82	0.40	1.43	0.63	

Table 5.3 Average breakup lengths for ethanol-water mixtures

Vol. Ratio of Ethanol	0%	10%	20%	30%	40%	50%
Breakup length (mm)	10.72	10.39	10.35	10.24	9.79	9.74
Standard deviation	0.59	0.51	0.57	0.41	0.47	0.52
Vol. Ratio of Ethanol	60%	70%	80%	90%	100%	
Breakup length (mm)	9.50	9.45	9.52	9.46	9.44	
Standard deviation	0.49	0.38	0.26	0.31	0.52	

Table 5.4 Average SMD over all locations

Vol. Ratio of Ethanol	0%	10%	20%	30%	40%	50%
SMD (μm)	125.7	118.6	112.1	97.2	85.7	77.4
Standard deviation (μm)	11.5	10.7	8.6	10.5	8.9	9.6
Vol. Ratio of Ethanol	60%	70%	80%	90%	100%	
SMD (μm)	71.3	69.2	59.3	50.1	38.9	
Standard deviation (μm)	9.3	9.4	9.1	8.3	7.5	

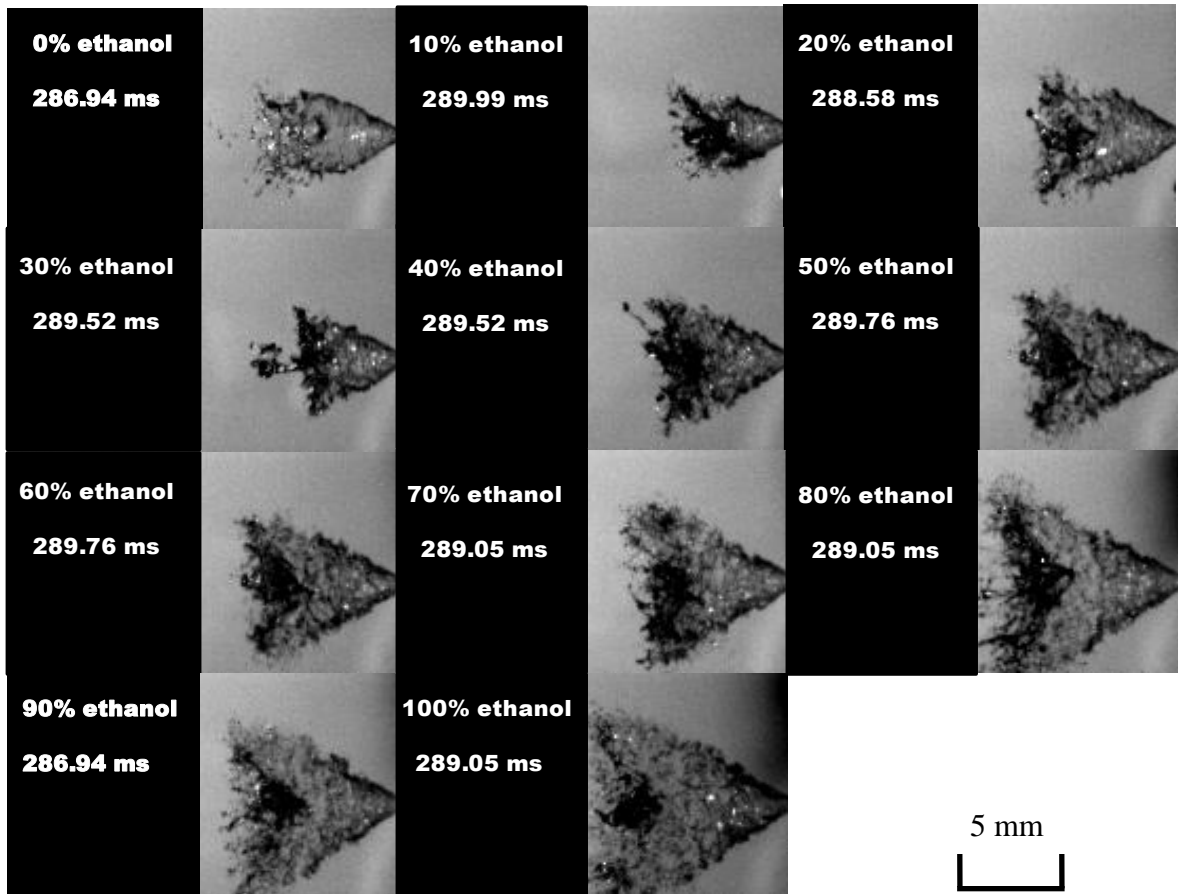


Figure 5.1 Starting stage of spray for different ethanol-water mixtures

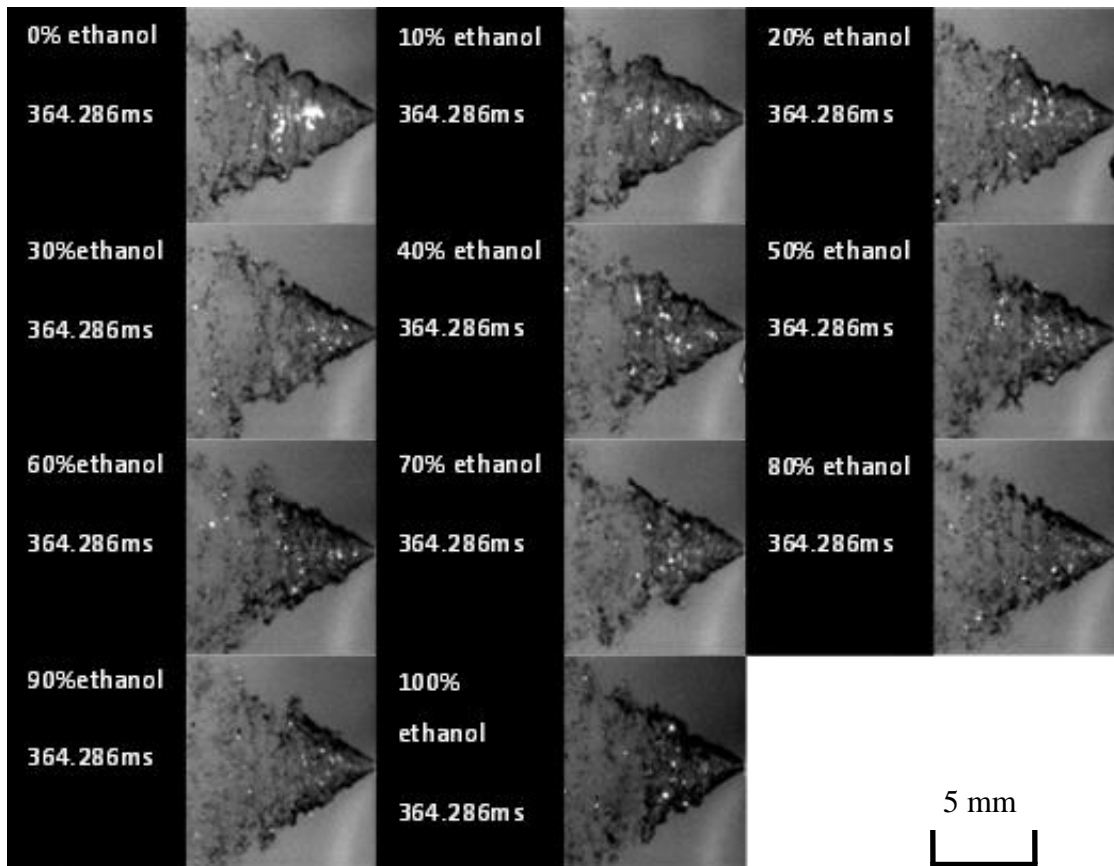


Figure 5.2 Developed stage of spray for different ethanol-water mixtures

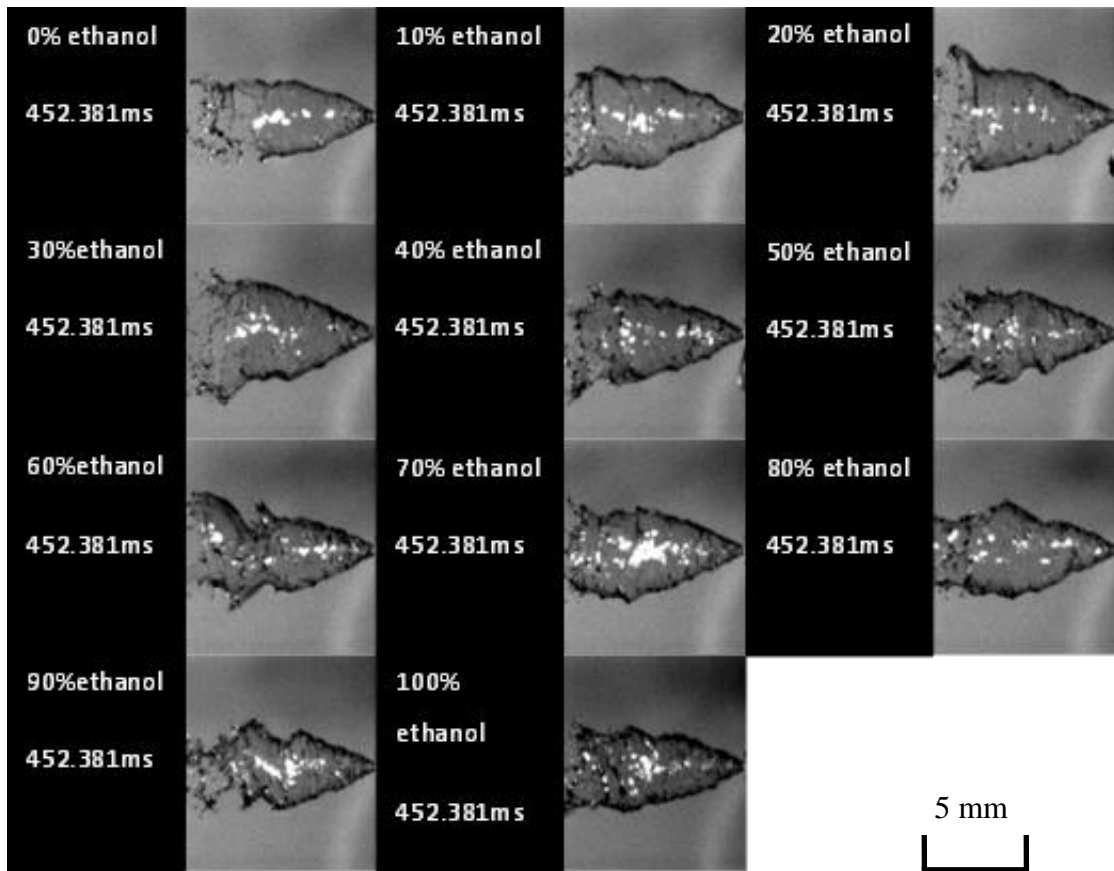


Figure 5.3 Ending stage of spray for different ethanol-water mixtures

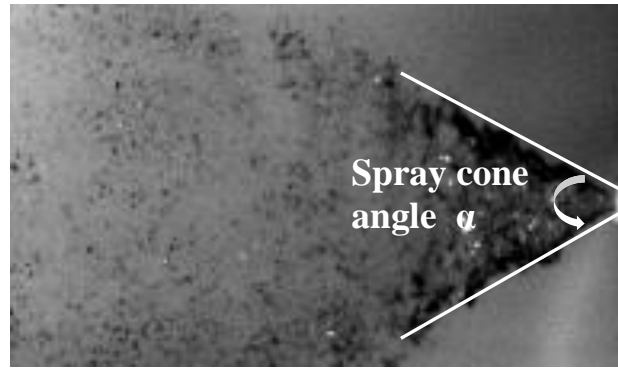


Figure 5.4 Global spray structure of spray and the calculated spray cone angle

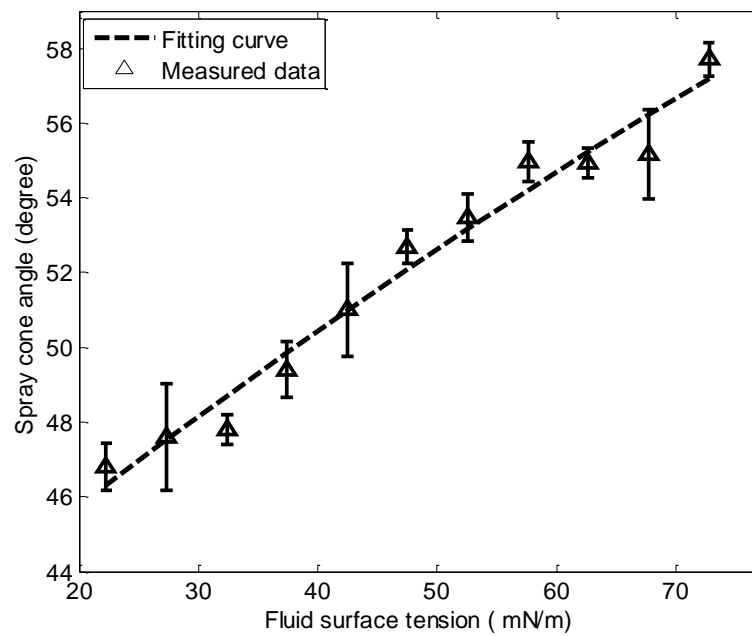


Figure 5.5 The average spray cone angle for different fluids and the error bars are based on 5 repeated runs

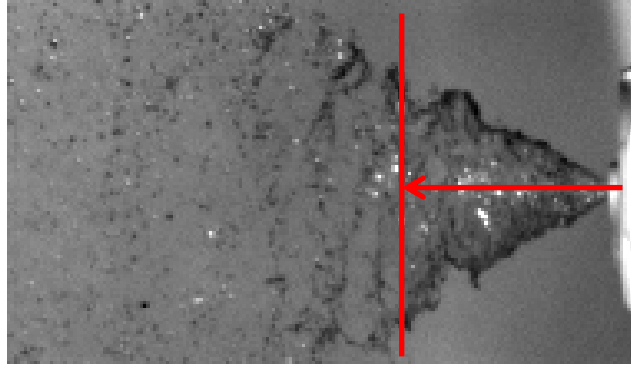


Figure 5.6 Calculation of the breakup length in a global near nozzle spray image

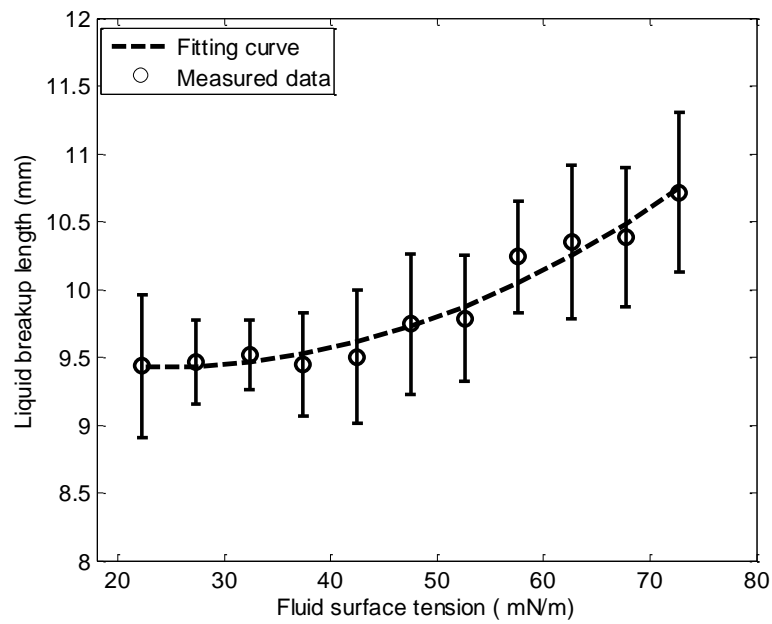
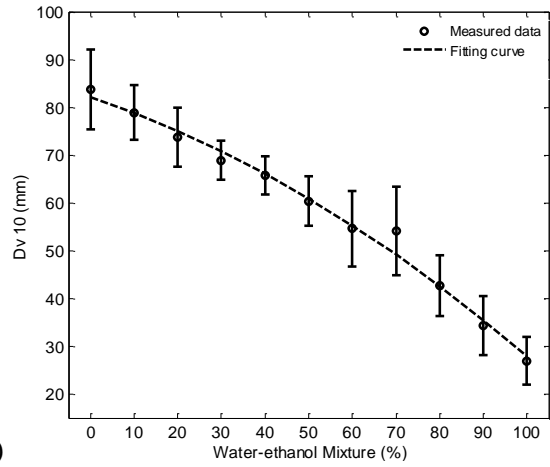
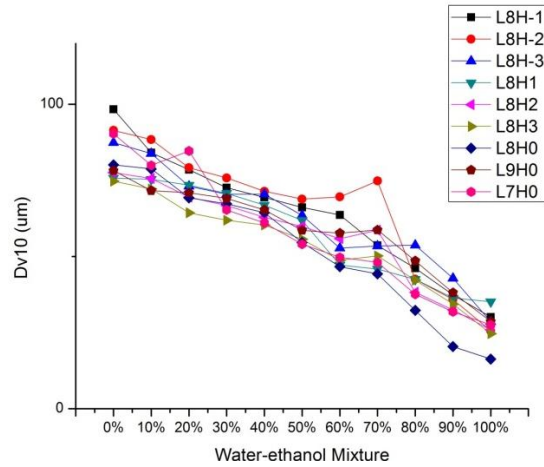
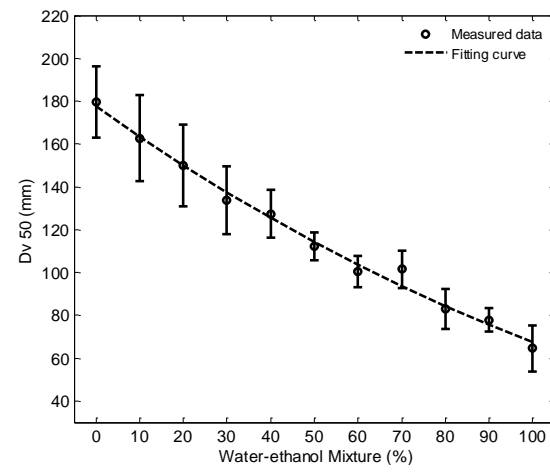
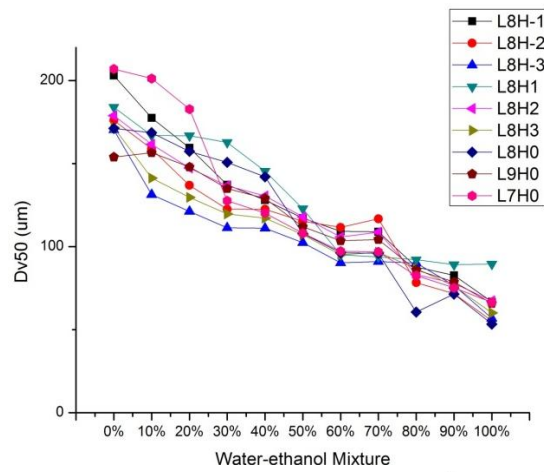


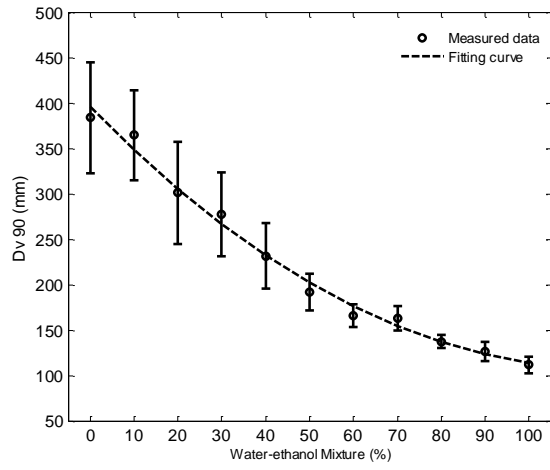
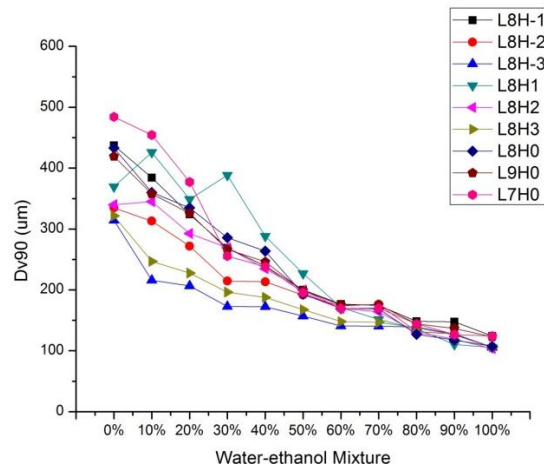
Figure 5.7 The average breakup length and the error bars for different fluids



(a)



(b)



(c)

Figure 5.8 Characteristic droplet diameters at different locations and their average values with error bars for different fluids: (a) Dv_{10} ; (b) Dv_{50} ; and (c) Dv_{90}

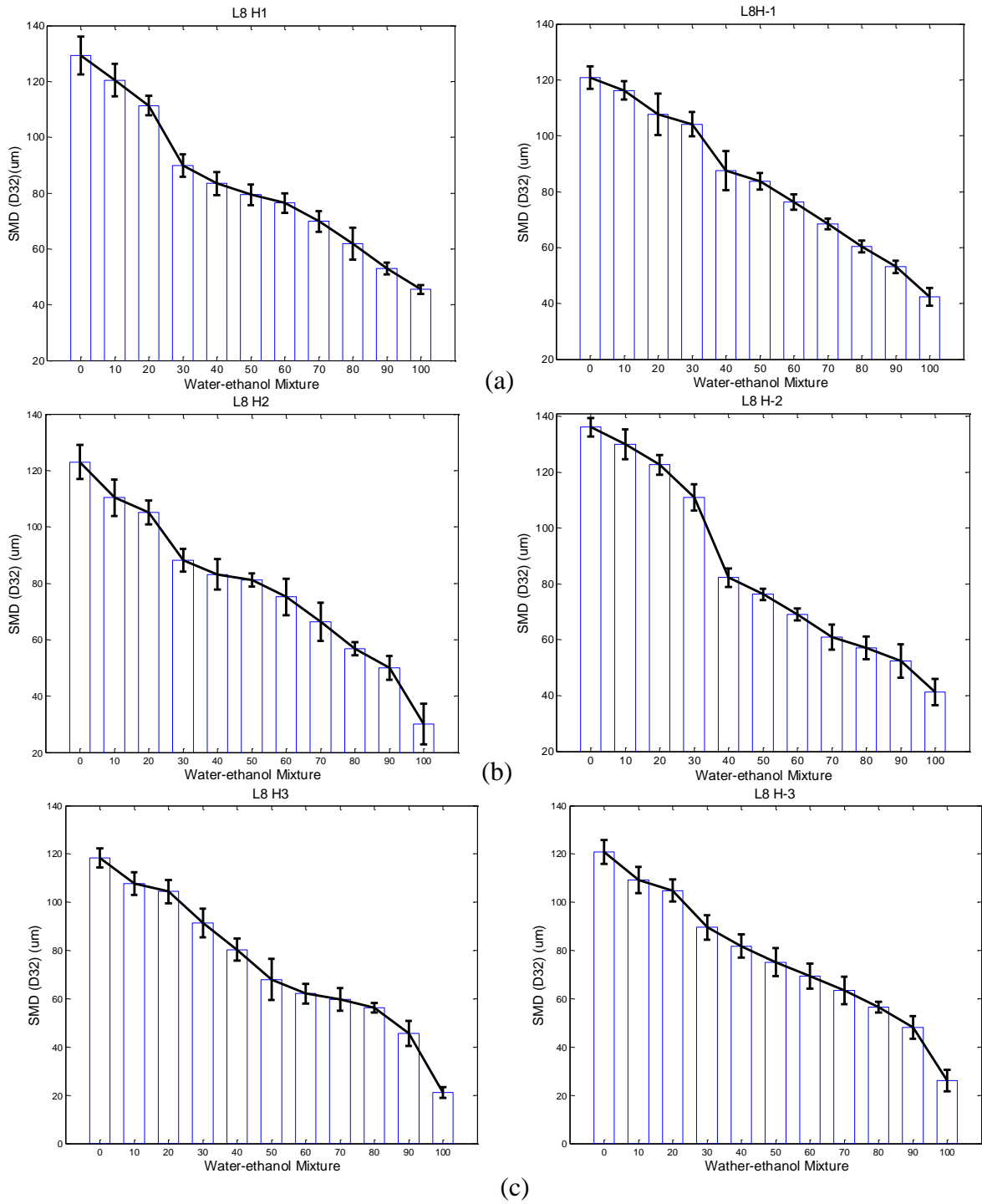


Figure 5.9 The average SMD with error bars at different vertical locations: (a) 2.54cm from the axis; (b) 5.08cm from the axis; and (c) 7.62cm from the axis

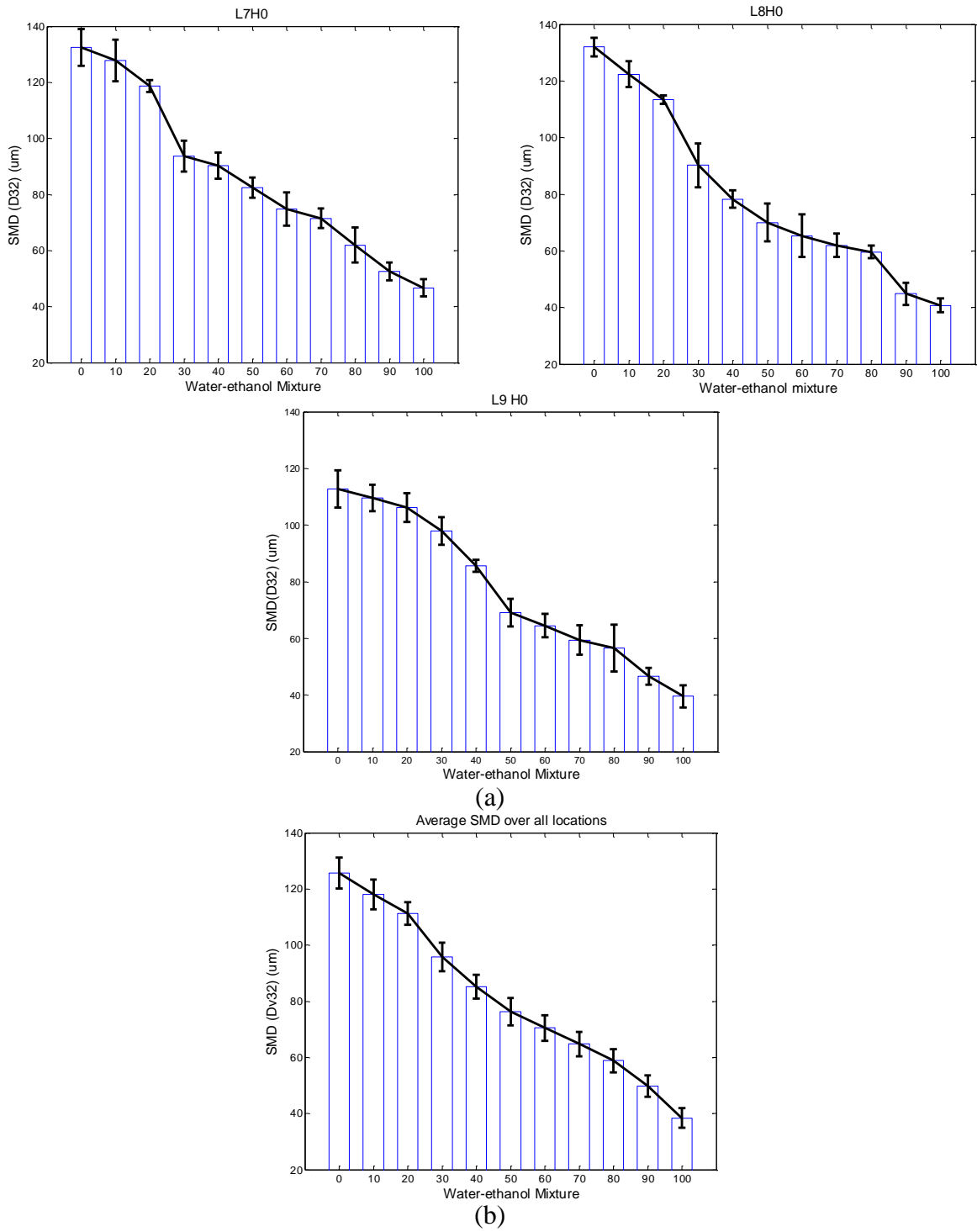


Figure 5.10 The average SMD with error bars at different horizontal locations (a) and the average SMD over all locations (b)

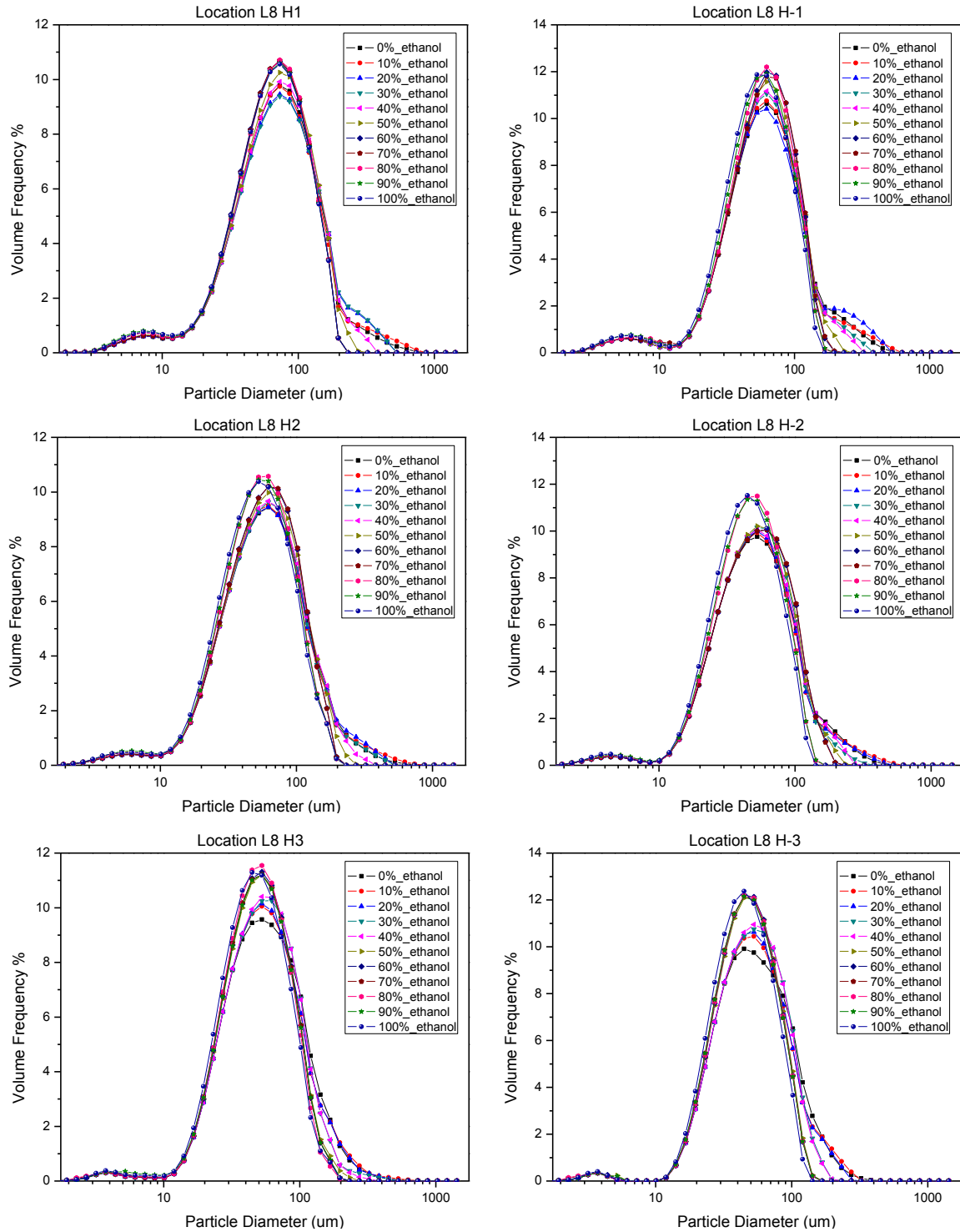
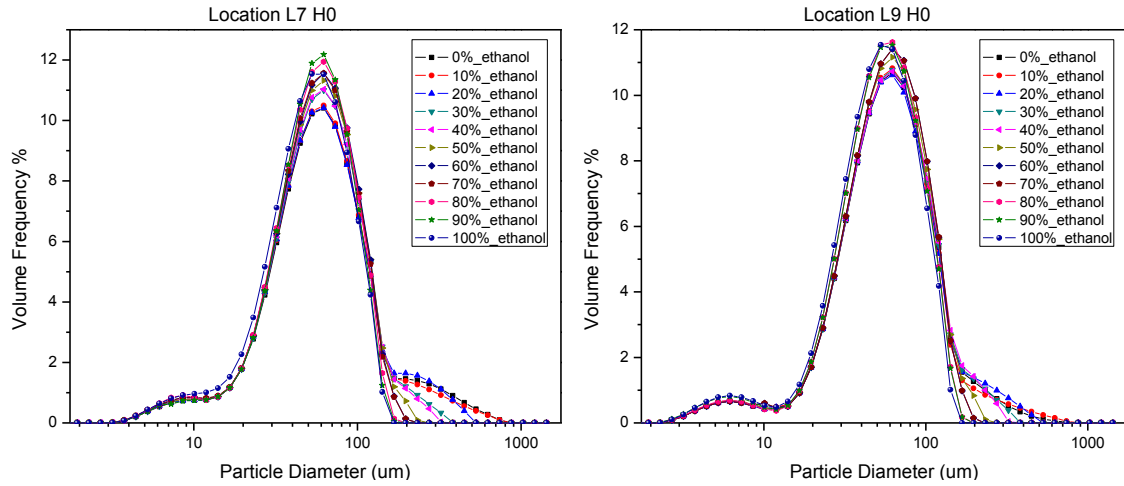
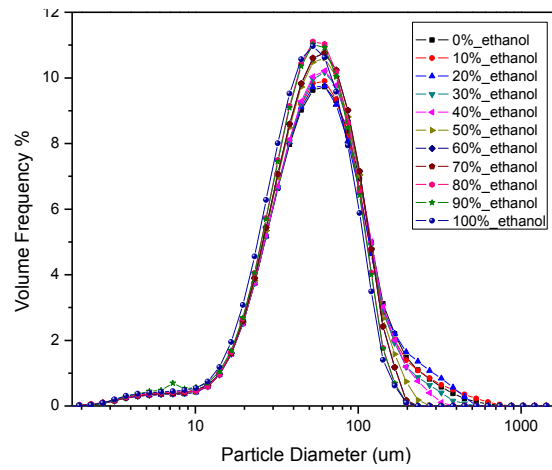


Figure 5.11 The droplet size distribution at different vertical locations



(a)



(b)

Figure 5.12. The droplet size distribution at different horizontal locations (a) and the averaged particle size distribution over all locations (b)

6. EXPERIMENT STUDY ON LIQUID FILM THICKNESS

6.1. Introduction

As illustrated in the previous chapters, the breakup of the spray sheet into droplets is a complex process. The majority of the breakup models use aerodynamics sheet instability concepts for the breakup of the sheet. In Chapter 4 and 5, the effects of fluid properties, including viscosity and surface tension on the transient spray development process and the overall spray structure from the trigger sprayer were studied. It is known that the fluid film thickness inside the swirl atomizer nozzle also plays an important role in controlling the sheet thickness and primary breakup. Therefore, accurate measurements of the liquid film thickness in swirl atomizers are of practical interest.

In pressure swirl atomizers, the liquid exits from the nozzle orifice as a thin conical sheet. The liquid sheet spreads outward radially, and breaks up into ligaments and then droplets. Many researchers have conducted extensive researches on the liquid film thickness characterization in pressure swirl atomizers. The annular liquid film formed inside the nozzle and at the orifice exit strongly influences the liquid instability and breakup. Therefore, accurate film thickness measurements in swirl atomizers are desirable because the film thickness is an important upstream controlling parameter for spray characteristics during breakup and atomization processes, such as spray angle, breakup length, droplet sizes and distributions. York et al. made a rough estimation of droplet size produced by a swirl atomizer [111]. They estimated the mean drop diameter to be a ratio of the square root of the

sheet thickness and the wavelength for the maximum growth rate. But they found that the agreement between theory and experiment was only qualitative.

The majority of the breakup models use aerodynamics sheet instability concepts for the breakup of the sheet. These models assume that small disturbances on the liquid sheet grow resulting in the breakup of the sheet. However, experiments have shown the formation of significant perforations on the sheet. The sheet and the spray have large scale periodic features. Generally, three different mechanisms interact, resulting in a complex breakup mechanism. These are aerodynamic instability, perforated sheet, and periodic fluctuations of the air core. The latter affects the swirling liquid surface inside the nozzle. For instance, studies using glass nozzles have revealed the existence of helical waves on the surface of the liquid core inside the nozzle. This results in variations in the local film thickness profiles along the sheet [112]. The sheet perforation process is not well understood. Several different causes are suggested for the onset of perforation, including impingement of small droplets on the surface of the sheet, turbulent fluctuations inside the sheet, and small bubbles in some cases, and disturbances in the air core of the nozzle [113–115]. The main approach that is currently used to model swirling sheet atomization is based on the aerodynamics instability.

This chapter focuses on the effects of the injection pressure and the fluid viscosity on liquid film thickness in a swirl atomizer operated at steady state conditions. High speed digital camera and backlight illumination were used to measure the film thickness. Film flow inside a micro scale nozzle orifice was visualized through transparent nozzles. The liquid film thickness was calculated in post image processing similar to the methodologies used in

the previous works. The effects of pressure and viscosity on the film thickness were further analyzed. The experiment results and estimated results from published equations were also compared.

6.2. Mathematical equations

The instability theories for the breakup of a liquid sheet are discussed in Chapter 2. In computational models, liquid film thickness can be obtained based on the information of air core diameter and the spray cone angle. The swirling liquid exiting a nozzle forms a liquid film, the thickness of which can be obtained based on liquid mass flow rate:

$$\dot{m} = \rho u A \quad (6-1)$$

where A is the cross section of the sheet at a certain distance from the nozzle and u is the mean velocity of the sheet at the same distance. The film thickness h is determined from conservation of mass:

$$urh = u_0 r_0 h_0 \quad (6-2)$$

where r is the radius from the injector centerline to the middle of the sheet, and the subscript 0 refers to the initial condition at the exit of the injector. The film thickness, right at the exit of the nozzle can be determined from:

$$\dot{m}_l = \pi \rho_l u h (d_0 - h) \quad (6-3)$$

And the initial velocity u_0 can be obtained based on mean flow velocity, which depends on the injection pressure [116]:

$$U = K_v \sqrt{\frac{2\Delta p}{\rho_l}} \quad (6-4)$$

K_v is an injector-specific dimensionless velocity coefficient represented by:

$$K_v = \frac{C_D}{(1-X)\cos\theta} \quad (6-5)$$

C_D is the fuel injector's coefficient of discharge and X is the ratio of the air core area at the nozzle exit to the nozzle area. If X is known then the film thickness is given by

$$h = \frac{d_0}{2}(1-X^{1/2}) \quad (6-6)$$

Schmidt et al. pointed out that K_v is about 0.7 based on the comparison with the discharge coefficient of a sharp-edge nozzle for a single fluid with a L/D ratio of 4 [117]. If the cone angle is θ , then the axial velocity u_0 at the nozzle exit is:

$$u_0 = U \cos\theta \quad (6-7)$$

6.3. Experimental setup

Figure 6.1 shows the schematic of experimental setup of the control and the circulation system of the pressure swirl atomizer. A pump draws the fluid from the tank to supply it to the sprayer at elevated pressure. A bypass valve placed after the pump is used to control the pressure in the atomizer. When the valve is fully open, all of the fluid flow returns to the tank. When the valve is partially to fully closed, the flow rate and the pressure in the atomizer increase, but the return flow rate to the tank decreases. The tank is used as both a reservoir for the water-glycerin mixture and a container to catch the spray from the swirl atomizer. The fluid then travels from the valve through the flow meter. The flow meter used

is a high pressure variable area flow meter. A Bourdon pressure gauge placed after the flow meter is used to measure the pressure of the fluid flowing through the atomizer.

6.3.1. Nozzle structure

The geometry of pressure swirl atomizer is shown in Figure 6.2. Acrylic glass was used to make the pressure swirl atomizer, because its transparency allows visualizing the flow inside the nozzle. All parts of the swirl atomizer were sealed by different sets of O-rings. The experiment was done under relatively low pressures, which does not present a challenging sealing problem for this design. Three o-rings are adopted as sealing and prevent leakage. Table 6.1 lists the specifications of the swirl atomizer. There are three tangential inlet ports in the swirl chamber with a 30 degree swirler angle.

6.3.2. Flow visualization

The film flow inside the nozzle was visualized in order to measure the liquid film thickness. Phantom v4.3 from Vision Research Inc. was used to take the digital images. It was connected to a computer for triggering camera trigger shutter and for image storage. A back-illumination technique was adopted by using a 1000W stage light source to illuminate the visualization area. A light diffuser was installed between the light and the nozzle to ensure a uniform background light. Global spray including the liquid film structure was visualized at a frame rate of 3600 frames/second with an exposure time of 6 microseconds. The resolution was set to 320×400 pixels, which correspond to a 33.7mm×42.1mm imaged region. Figure 6.3 shows the global spray structure and liquid film structure inside the nozzle. The film thickness is calculated by an image processing code using MATLAB.

6.3.3. Experimental conditions

In order to investigate the effect of injection pressure on liquid film, the injection pressure was varied from 0.07MPa to 1MPa. Under 0.07MPa, the atomizer did not generate a typical spray; only a smooth onion shaped hollow cone sheet was formed, which is not of interest to this study. On the other side, 1MPa was the upper limit due to the fact that the main objective of this work is focused on the low injection pressure. The ambient conditions were atmospheric conditions. The liquid mass flow rate was also measured. Figure 6.4 shows the experimental mass flow rate and the fitting curve for pure water. It is plotted as a function of the fluid pressure, which ranges from 16.7 g/s to 60 g/s.

The working fluids with different viscosities were prepared by mixing distilled water with glycerol in different glycerol volume ratios from 0% to 70% with a step of 10%. The experiment temperature was maintained at the room temperature ($23^{\circ}\text{C} = 296\text{ K}$). The fluid viscosity is listed in Table 4.1 for different mixtures. The surface tension of water and glycerol are relatively close at room temperature (water is 72 mN/m and glycerol is 63 mN/m), the variation of surface tension of the mixtures are less than 10%. In addition, the density of the two fluids are close (water is 1000kg/m^3 and 70% glycerol-water is 1182 kg/m^3), the density variation of the fluid mixtures are less than 12%. But the viscosity variation for the different mixtures is significant as shown in Table 4.1. Therefore, it is expected that the viscosity effect dominates the results. The properties of the glycerol-water mixtures are well documented in the literature by standard table and these values were obtained from the table and interpolated at the given room temperature and volume ratio.

6.4. Results and discussions

6.4.1. Spray characteristics under steady state

In order to systematically study the external and internal spray characteristics, Figure 6.5 illustrates the spray structure for water and 40% glycerol-water mixture. Three different pressures, 0.07Mpa, 0.345Mpa and 1.0Mpa are selected to cover a wide range of operation conditions. When the injection pressure is low, the jet first forms a closed rim sheet, and then as the pressure become higher, the spray forms an open conical sheet. When the spray sheet is fully developed, an air core is formed inside the orifice resulting in a thin film of liquid exiting the nozzle. Figure 6.6 shows the spray cone angle as a function of injection pressure. The trend is clearly observed from the figure that the spray angle becomes larger as the injection pressure increases. The impact of pressure is smaller under higher pressure conditions. The effect of fluid viscosity on spray angle is showed in Figure 6.7. Spray angle becomes smaller as fluid viscosity increasing, which is consistent with the results found in Chapter 4. The breakup length of liquid sheet is calculated from the high speed images. Figure 6.8 and Figure 6.9 illustrate the breakup length as functions of injection pressure and fluid viscosity, respectively. It can be seen that the breakup length becomes longer as the viscosity increases or the injection pressure decreases. The change on spray angle, as well as breakup length becomes smaller as the injection pressure increases. This indicates that pressure may only have a limited impact on the primary breakup process when it reaches a certain level.

6.4.2. Film thickness under different injection pressures

The measured film thickness can be overvalued due to the curving of the nozzle orifice and the difference in the refractive indices of the liquid, acrylic and air. This work uses a similar analysis method proposed by Moon et al. to compensate the curving effect [43]. The back light source used in this study is not coherent and can travel to all directions. Two different methods were applied to analyze how the light arriving at the all directions. The first method considers the light moving convergent from the liquid film to the center of the camera front lens, while the other method considers the light moving divergently. The captured liquid film images in both cases show larger liquid film thickness than the actual thickness. These two methods provide two limit cases and can cover the lights from all directions in practice.

In order to obtain a clear boundary between liquid film and air core, images were focused on the orifice region of the swirl nozzle. Figure 6.10 shows the captured liquid film images inside nozzle orifice at different injection pressures with 30% glycerol-water mixture. It can be seen that as the pressure increases, the liquid film thickness become thicker. The images in Figure 6.10 show the boundary line between the liquid film and the air core. The liquid film is detected by using an edge detection MATLAB code developed by the author. The liquid film thickness at any axial locations was obtained by calculating the distance between the nozzle outer surface and the detected edge. The mean liquid film thickness under each pressure was calculated by averaging the thickness over the whole nozzle length. Three hundred images were captured and processed to reduce the possible error from variation in time.

Figure 6.11 shows the measured film thickness obtained by image processing method and the fitting curves using power law under different injection pressures. It can be seen that the liquid film thickness becomes thinner with increased injection pressure for all working fluids. When pressure increases, there is more momentum for the liquid for the same viscosity fluid. The increasing liquid velocity at the swirl chamber inlets affects the film thickness inside the nozzle. But it can be also observed that (Figure 6.11) as the injection pressure rises its effect on liquid film thickness becomes less significant. The balance between centrifugal force generated from swirl chamber and the drag force from the liquid contributes to this trend.

6.4.3. Film thickness for different viscosity fluids

Figure 6.12 shows the captured liquid film images at 0.2MPa with different glycerol-water mixtures. It can be seen that under the same pressure, the film thickness is thinner as the fluid viscosity decreases. The same edge detection method and MATLAB code were used to process the film thickness images. The mean liquid film thickness under each viscosity value was calculated by averaging the thickness over the whole nozzle length. Three hundred images were captured and processed to reduce the possible errors.

Figure 6.13 shows the measured film thickness obtained by image processing and the fitting curves using power law under different fluid viscosities. The liquid thickness becomes larger as the viscosity increases. The change is small for fluids of low viscosity but becomes larger for fluids with higher viscosity. The balance between the centrifugal forces generated from swirl chamber and the drag forces from the liquid forms the air core. For more viscous

fluids, the drag force from the liquid is larger than the centrifugal force generated from swirl chamber, hence the air core becomes smaller and the liquid film becomes thicker.

6.4.4. Comparison between analytical equations and experiment

Several relations for the film thickness in terms of flow parameters are studied by other researchers. These works concluded that the main parameters affecting the liquid film thickness were liquid properties, injection pressure, and nozzle diameter. Table 6.2 summarizes the parameters considered as main factors affecting the liquid film thickness for each analytical equation. The first three equations considered the injection pressure as a crucial factor while the last three equations did not consider the injection pressure as a main parameter. Rizk and Lefebvre [120], Suyari and Lefebvre [39], and Kim et al. [118] all applied the equations at relatively low injection pressure conditions, which are less than 3.0MPa. These low injection pressure conditions are commonly used in aeronautic applications. Suyari and Lefebvre measured the liquid film thickness using an electrical conductance method in the discharge orifice [39]. They derived equation (6-2) by revising the constant of Rizk and Lefebvre's equation (6-1) from the experimental data. Equation (6-2) has been known to have a good agreement to some degree when the ratio between film thickness and orifice diameter is far less than 1. Based on these equations, the effect of injection pressure on liquid film thickness becomes smaller as the injection pressure increases.

$$h = \left(\frac{1560 \dot{m}_l \mu_l}{d_0 \Delta P} \frac{1+X}{(1-X)^2} \right)^{0.25} \quad (6-8)$$

$$h = 3.66 \left(\frac{d_0 \dot{m}_l \mu_l}{\rho_l \Delta P} \right)^{0.25} \quad (6-9)$$

$$h = 1.44 d_0 \left(\frac{\dot{m}_l \mu_l}{\rho_l \Delta P d_0^3} \right)^{0.25} \left(\frac{l_0}{d_0} \right)^{0.6} \quad (6-10)$$

But since X is the ratio of the air core area at the nozzle exit to the nozzle area and is dependent on the film thickness. Equation $h = \left(\frac{1560 \dot{m}_l \mu_l}{d_0 \Delta P} \frac{1+X}{(1-X)^2} \right)^{0.25}$ (6-8) involves some trial and error procedures. The measured liquid film thickness was compared to the results from the analytical equations which take into account the effect of injection pressure.

Figure 6.14 shows the comparison between the measured liquid film thickness in this work and the calculated liquid film thickness from previous empirical equations [39,118]. Film thicknesses of the 70% glycerol/water mixture are calculated under different injection pressures. The experimental results and the estimated values all indicate that a higher nozzle pressure drop produces a thinner liquid film. The pressure drop is usually attributed to the increase in liquid discharge velocity. The experimental results show that the film thicknesses are thicker than the estimated results from both equations [39, 118]. The experiments have larger film thicknesses than the estimated values. Calculated thicknesses based on Suyari and Lefebvre's study are only half of the current experimental results. Kim et al. gives a similar value at very low pressure (0.07Mpa), but the decreasing rate of film thickness is faster than the present results. The disagreement between the experimental and the estimated film

thickness from published empirical equations may be due to the high viscosity of the liquid used in this work. The liquid drag force caused by viscosity leads to a slower decrease as injection pressure increases. The interaction between these two factors controls the complex process in forming the initial liquid film. But the improvement in atomization quality can be still realized by an increase in nozzle pressure drop.

6.4.5. Effect of fluid properties

The influence of liquid viscosity is clearly a major factor that controls the atomization process. The viscous force affects the atomization process in two ways, one is by increasing the initial film thickness and the other is by resisting the disintegration of the liquid sheet into ligaments and small drops. The effect of liquid density on the liquid film thickness is quite small. Thus its influence on atomization quality should also be small. Rizk and Lefebvre [120] studied the spray characteristics of a simplex swirl atomizer and confirmed this conclusion by measuring the mean droplet size using liquid with different densities. It is also noted that surface tension does not appear in the above equations (1 to 3) for the film thickness calculation. Surface tension does play a major role in the subsequent breakup of the liquid sheet into ligaments and further breakup into small drops as shown in Chapter 5, but its effect on the film thickness is neglected based on the previous conclusions [120].

Figure 6.15 shows the comparison between the measured liquid film thickness and the estimated liquid film thickness from previous equations (6-9) and (6-10) at 0.14 Mpa. Both experimental and estimated results show the similar trends that film thickness becomes thicker as fluid viscosity increases. The experimental results showed the larger film

thickness comparing to previous results. The calculated thicknesses based on Suyari and Lefebvre's study are only half of the current experimental results for low viscosity fluid. Kim et al. gives a similar value for 70% glycerol/water mixture, which has the most viscous fluid. The increasing rate of film thickness is faster than the present results.

Quantitatively experimental results provide a useful guidance on the effect of atomizer characteristics and liquid flow properties, especially fluid viscosity on the film thickness. Frictional losses are the major consideration in the design of swirl atomizers. The frictional losses represent a wasteful dissipation of atomization energy, which reduces the effective pressure drop across the atomizer and also the discharge coefficient. Further, friction also reduces the diameter of the air core by impeding the rotating flow in the swirl chamber with low fluid velocity, thereby decreases the discharge coefficient.

6.5. Summary

As discussed in Chapter 2, many techniques have been developed to measure liquid film thickness, but most of them are not suitable for pressure swirl atomizers. This is because the nozzle orifices in swirl atomizers are usually in a small meter. This requires the measurement technique must be able to accurately determine the small amplitude and high speed disturbances of liquid film inside the nozzle in sub-micron meter scale.

The liquid film thickness inside a transparent pressure swirl nozzle orifice was measured and the measurement error was considered in order to obtain more accurate results. Both injection pressure and fluid viscosity effects on liquid film thickness were analyzed by post-processing images. It has been found that measured film thickness decreases as the

injection pressure increases. While as the injection pressure rises, the effect of the injection pressure on liquid film thickness becomes less significant. Fluid viscosity plays a crucial role in controlling the liquid film thickness. The liquid film thickness becomes larger as the viscosity increases and the change is small for low viscosity fluids and much bigger for fluids with high viscosity. But under the present experimental conditions, the effects of injection pressures are more pronounced than the fluid viscosity. It is easy to observe that there is some oscillation wave between film and air-core interface. Ideally, it would be very informative to analyze the oscillation of the liquid film inside the nozzle, therefore to compare the domain frequency from the internal to external wave (such as the work done in Chapter 4). Unfortunately, our image resolution was not high enough to capture the wave instability in micro scale, which should be a focus of future work.

6.6. Tables and figures

Table 6.1. Atomizer specifications

Nozzle parameter	
Nozzle orifice diameter (mm)	2
Nozzle orifice length (mm)	4
Swirl chamber diameter (mm)	8
Length /Diameter ratio	2
Swirler angle (degree)	30
Working fluid	Glycerol-water mixture

Table 6.2. Analytical and empirical equations for the sheet thickness

Authors	Equations
Rizk and Lefebvre [120]	$h = \left(\frac{1560 \dot{m}_l \mu_l}{d_0 \Delta P} \frac{1+X}{(1-X)^2} \right)^{0.25}$
Suyari and Lefebvre [39]	$h = 3.66 \left(\frac{d_0 \dot{m}_l \mu_l}{\rho_l \Delta P} \right)^{0.25}$
Kim et al. [118]	$h = 1.44 d_0 \left(\frac{\dot{m}_l \mu_l}{\rho_l \Delta P d_0^3} \right)^{0.25} \left(\frac{l_0}{d_0} \right)^{0.6}$
Lefebvre [103]	$\left(\frac{A_p}{2Rd_0} \right)^2 = \frac{\pi^2}{32} \frac{(1-X)^3}{X^2}$
Badami et al. [119]	$h = \left(\frac{D_0}{2} \right) (1-k) \text{ where } \theta = 2 \arctan \sqrt{\frac{k^2}{1-k^2}}$
Moon et al. [43]	$h = 0.97 A_p^{0.08} \left(\frac{\mu_l D_0}{\rho_l} \right)^{0.25} \left(\frac{l_0}{D_0} \right)^{0.76} (\tan \alpha)^{-0.12}$

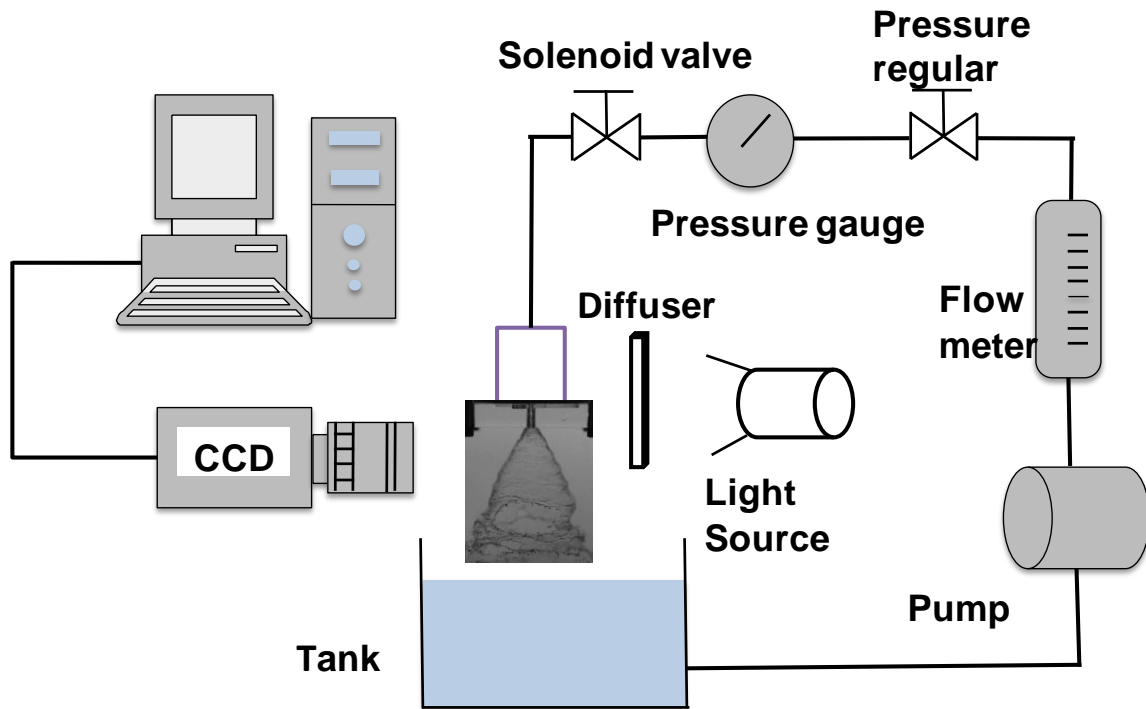


Figure 6.1. Schematic of experimental setup

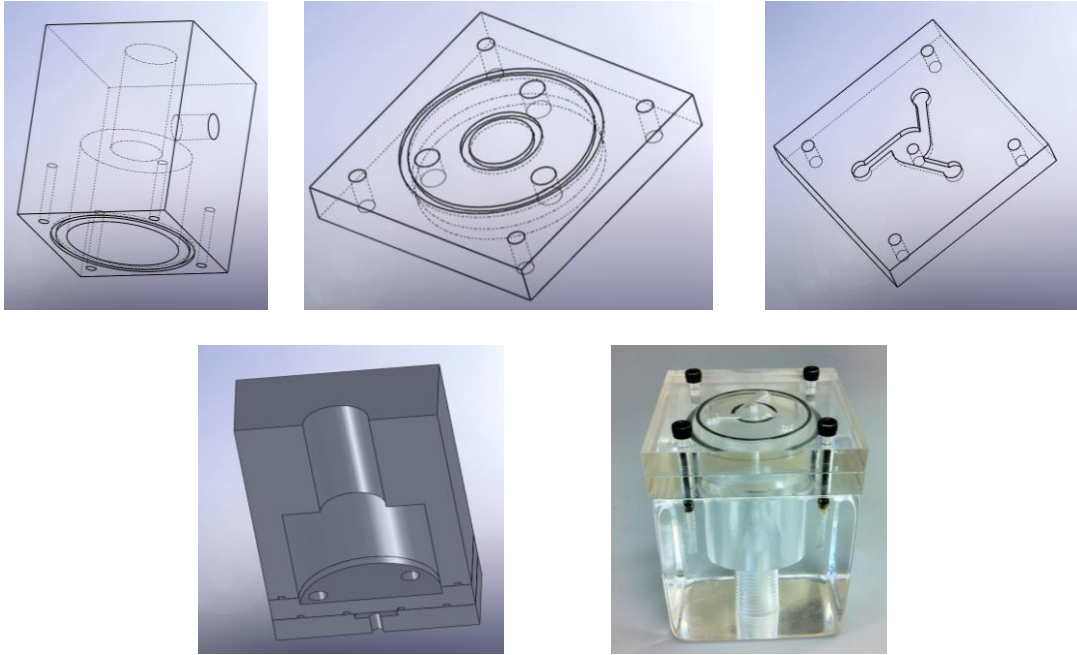


Figure 6.2 Geometry of the transparent swirl atomizer

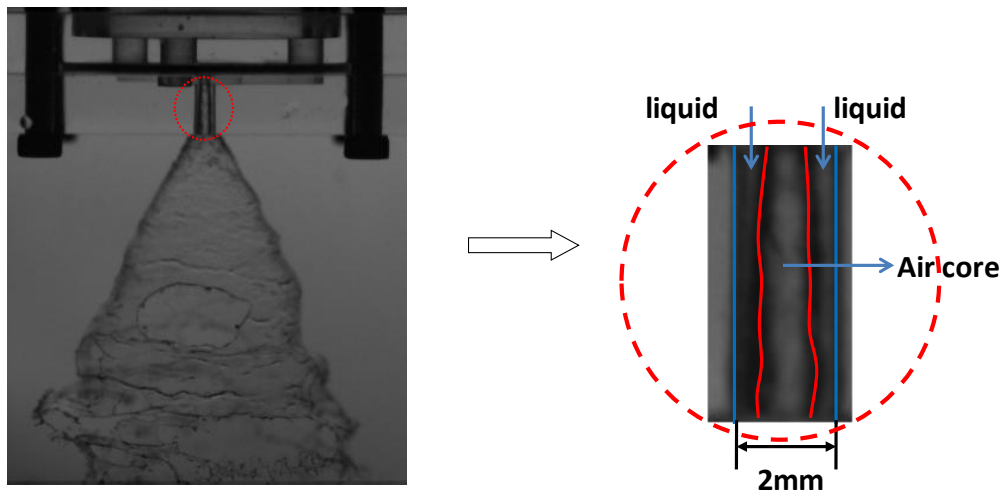


Figure 6.3 Global spray structure and liquid film structure inside the nozzle

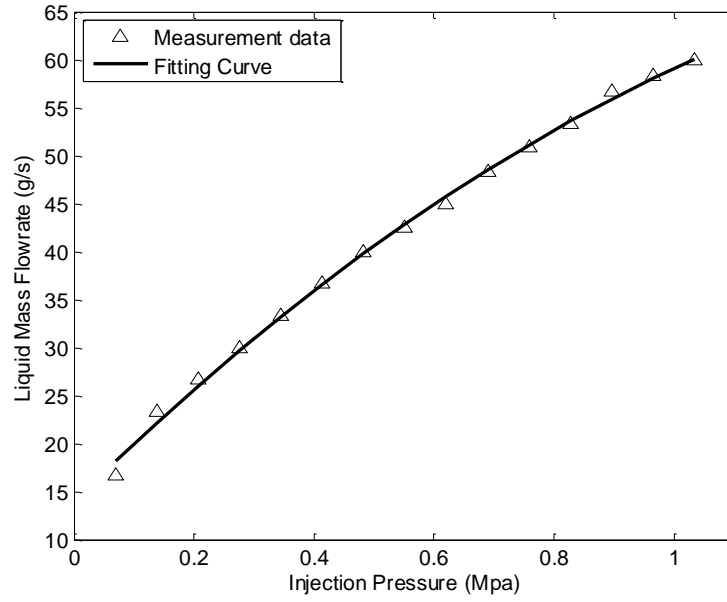


Figure 6.4 Experimental mass flow rates at different fluid pressures

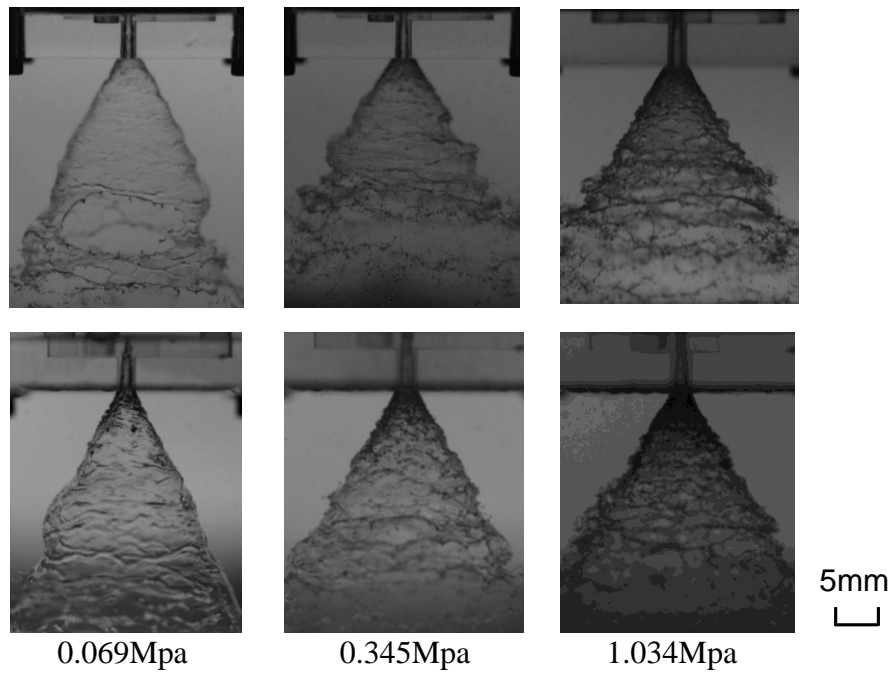


Figure 6.5 Spray structure under different pressures for water and 40% glycerol/water mixtures

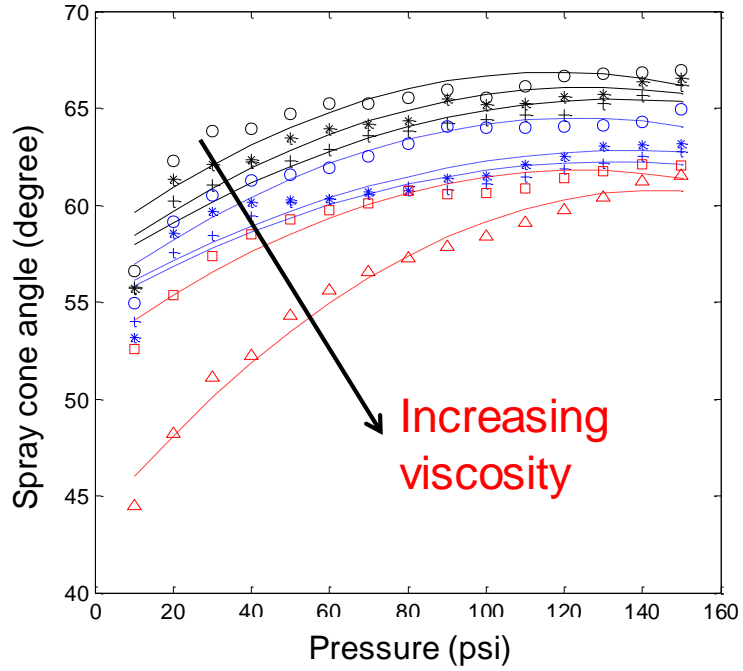


Figure 6.6 Spray cone angle under different injection pressures

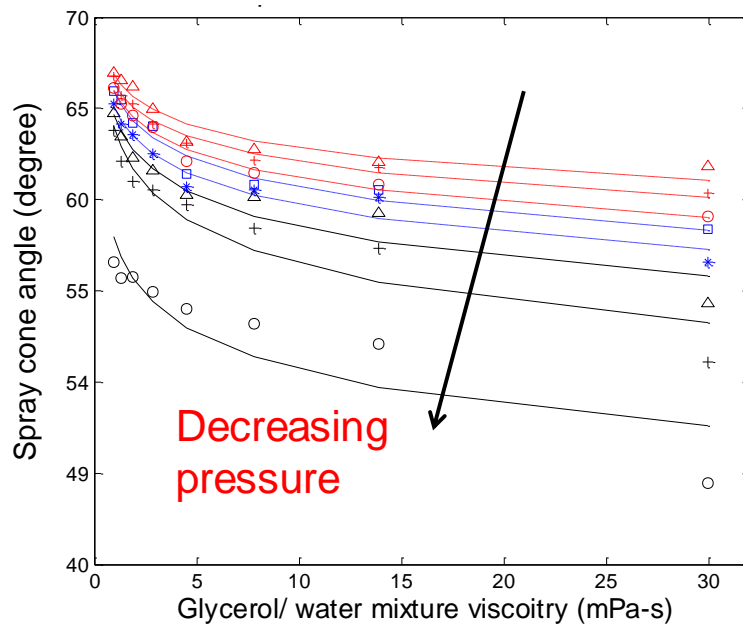


Figure 6.7 Spray cone angle for different glycerol/water mixtures

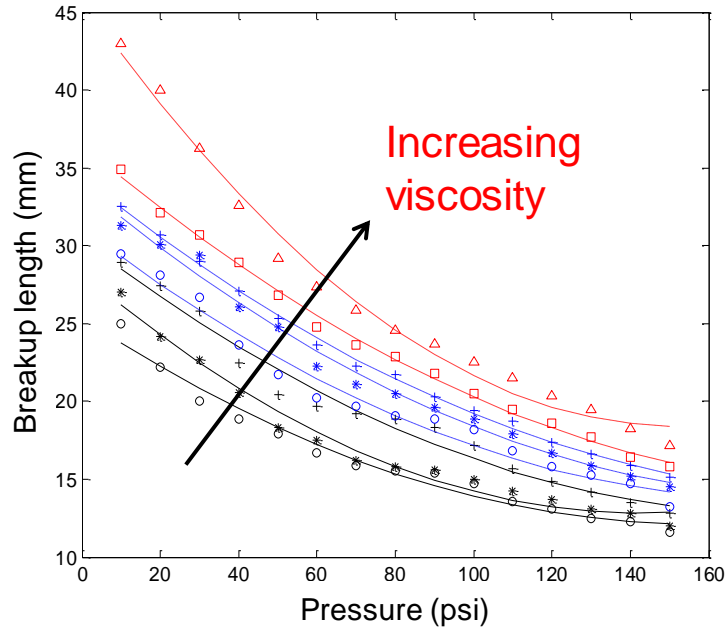


Figure 6.8 Breakup lengths under different injection pressures

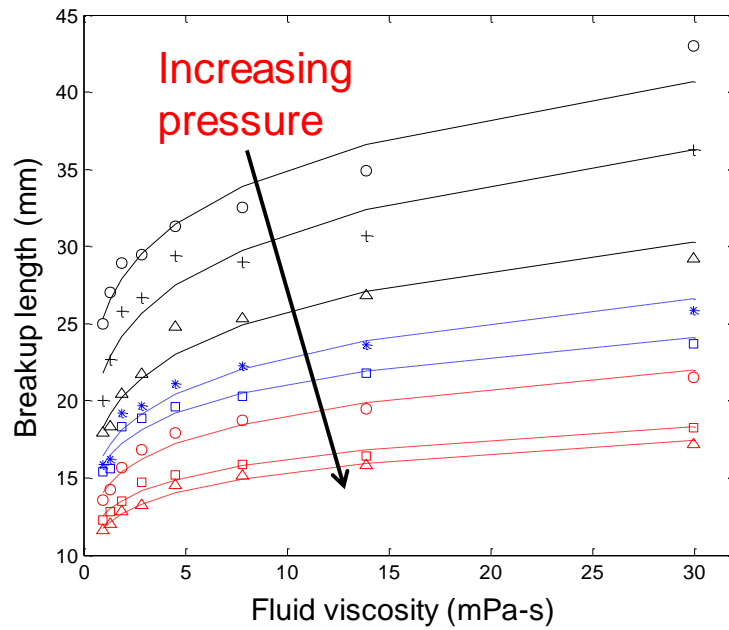


Figure 6.9 Breakup lengths for different glycerol-water mixtures

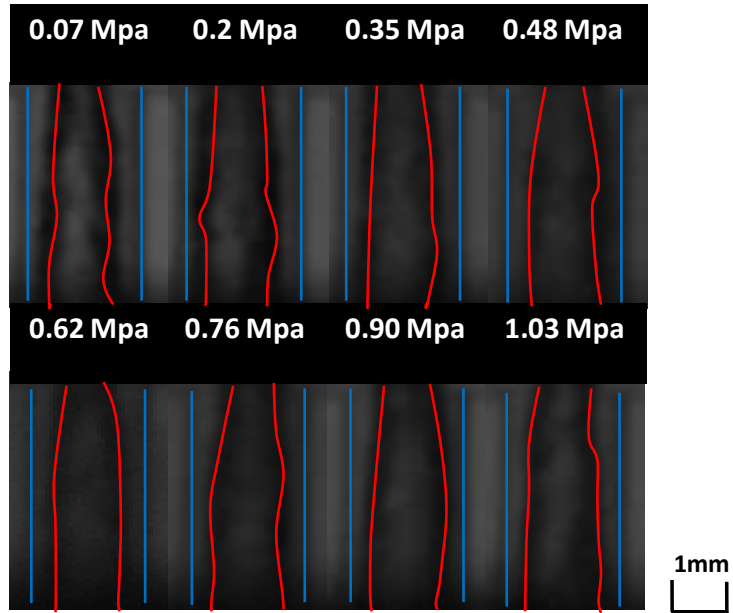


Figure 6.10 Liquid film images under different pressures for 30% glycerol/water mixture

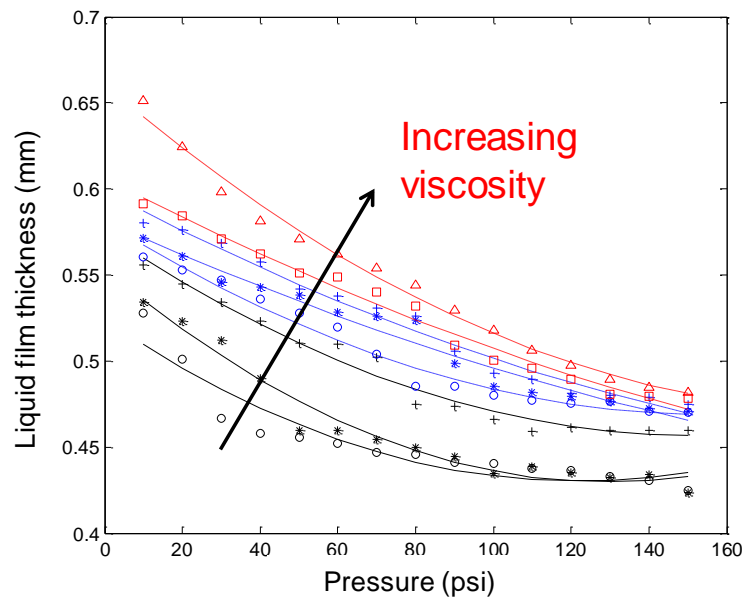


Figure 6.11 Measured film thickness and fitting curves under different injection pressures

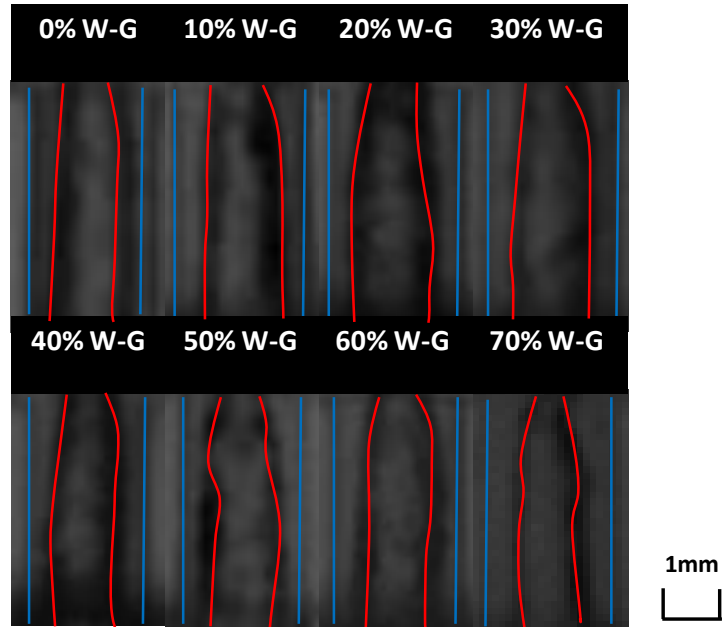


Figure 6.12 Liquid film images of liquid with different viscosity under 0.2Mpa

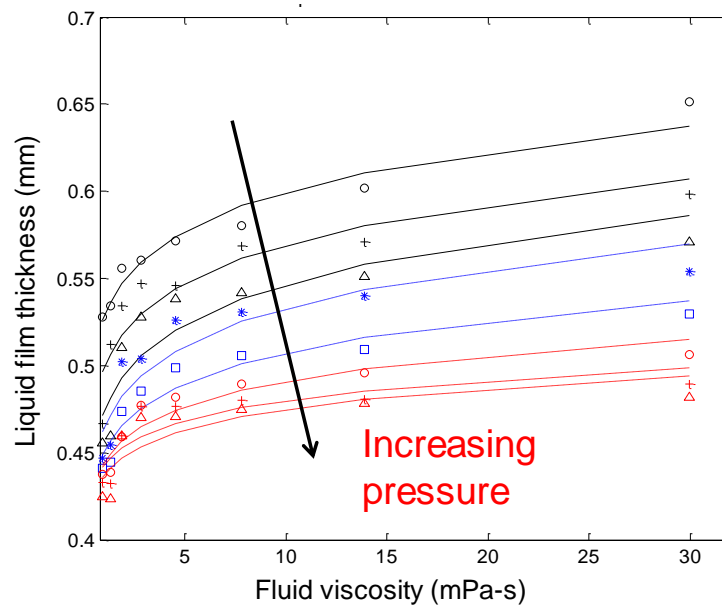


Figure 6.13 Measured film thickness and fitting curves for different glycerol-water mixtures

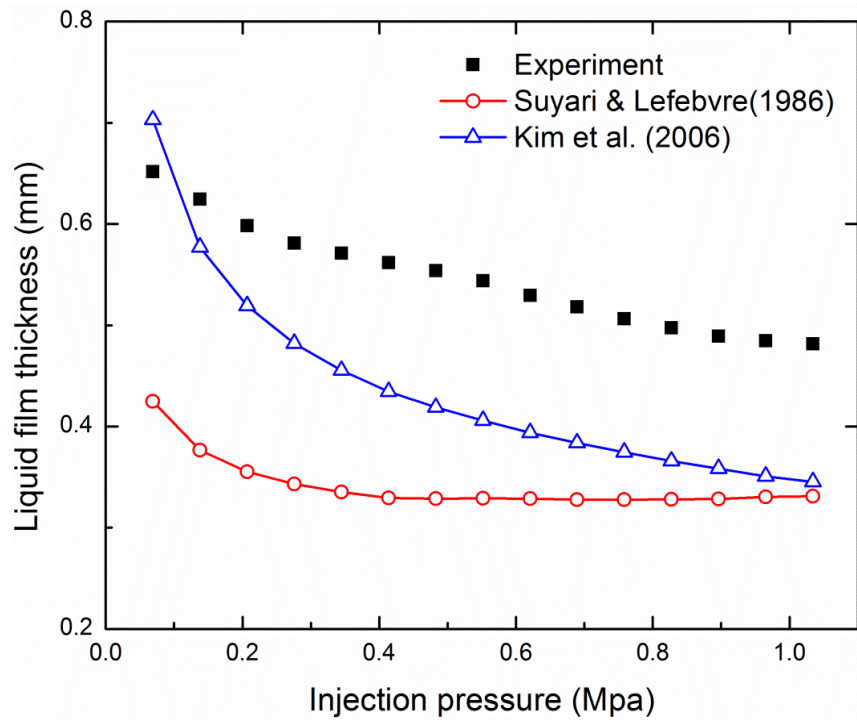


Figure 6.14 Comparison between measured liquid film thickness and estimated film thickness previous empirical equations of 70% glycerol-water mixture

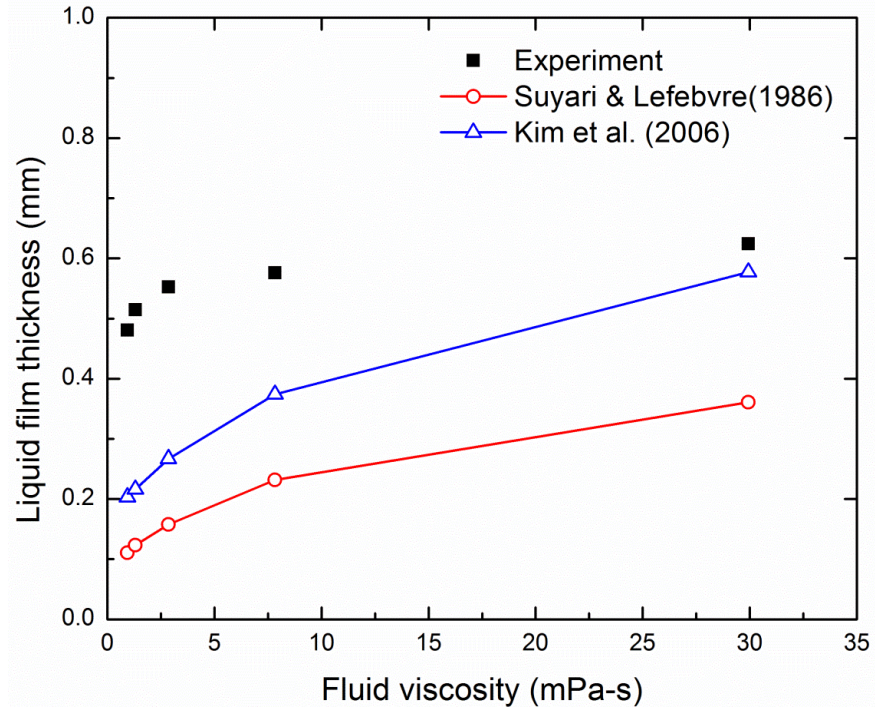


Figure 6.15 Comparison between measured liquid film thickness and estimated film thickness previous empirical equations in 0.14Mpa

7. EXPERIMENTAL STUDY ON EVAPORATION EFFECTS

7.1. Introduction

The breakup of a liquid jet is affected by a variety of disturbances, such as pressure or velocity disturbances, surface displacement, and temperature variation. Such external flow structures can be observed at different operational conditions in circular nozzles (Figure 7.1). Different jet breakup regime criteria are defined based on Weber number (Reitz's study [121]). Table 7.1 gives the classification of jet breakup regimes based on the gas Weber number. At very low velocities, the liquid exiting the orifice is substantially affected by gravitational acceleration which results in the dripping flow regime. As the jet speed increases, capillary forces dominate the atomization process in a regime typically referred to as the Rayleigh breakup regime. For both dripping and Rayleigh regimes, droplet pinching occurs in a reasonably axisymmetric fashion at the centerline of the jet thereby producing drops that are comparable in size to the orifice diameter. At higher velocities, aerodynamic interactions with the ambient gas lead to additional instability of the surface, which is termed the wind-induced regime. Within the wind-induced regime, we see the first instances of droplet pinching off at locations other than the centerline of the jet thereby providing the opportunity to form drops substantially smaller than the diameter of the orifice. At even higher velocities, the liquid jet enters the atomization regime. A collection of very small drops around a liquid core vanishes at the some distance downstream of the orifice. Visualizations of the atomization regime are challenging because the liquid core tends to be obscured by the dense droplets cloud emanating from its periphery.

There are several studies on the effect of temperature perturbations on the instability of a liquid jet [122-124]. In non-isothermal capillary jets, variation of the surface tension with temperature along the free surface of the liquid results in a tangential shear force on the surface which induces the so-called thermocapillary flow. Since liquid surface tension is strongly dependent on temperature, it can be controlled by the liquid temperature. Furlani et al. have conducted a linear analysis of a jet subject to a spatially periodic variation of surface tension imposed along its length [125]. It has been shown that as the jet approaches breakup it swells at the points of maximum surface tension, and necks at the points of minimum surface tension.

Thermocapillary effects can enhance or retard the instability depending on the particular conditions. It is generally shown that the breakup of a liquid jet may occur not only for surface amplitude disturbances with axial wavelengths larger than the circumference of the jet, but also through oscillatory temperature gradients that excite the free surface. However, in many instances a liquid jet is injected into a high temperature environment, resulting in high evaporation rates. There are very limited studies focusing on the instability of an evaporating jet. Lian and Reitz conducted a linear stability analysis for an evaporating jet [72]. The jet velocity was found to be higher than the surface depletion rate caused by evaporation. Under these conditions the breakup of the jet was dominated by the aerodynamic interaction between the liquid and the ambient air. Their mathematical model shows that the evaporation has a destabilizing effect for low-speed jets in the Rayleigh regime.

In Chapter 4 and 5, both internal and external spray characteristics were studied for pressure swirl atomizer under a room temperature. The effects of fluid viscosity and surface tension on spray performance were studied quantitatively. This chapter emphasizes on the ambient temperature effect on liquid jet breakup. High speed visualization technology was again used to capture the jet behavior under different experiment conditions. Liquid jet breakup length and wave length were calculated from high speed images. The correlation between the non-dimensional number and liquid jet characteristics was also studied.

7.2. Experimental system

7.2.1. Experimental system setup

The low pressure injection system consists of a stainless steel water tank which is used to supply water to the orifice under pressurized conditions. Compressed nitrogen gas was used to control the tank pressure and drive the liquid at constant pressure. A water filter was used to control the tank pressure and drive the liquid at constant pressure. A water filter was installed to the outlet of the supply tank to filter out any contaminants. The water flow to the orifice was controlled using a flow control valve along with a digital pressure gauge to monitor the injection pressure and pressure drops occurring in the supply system, especially in the filter. Two radiant heaters were applied to heat up the air. The heater is adjustable, which make the temperature easily to be changed. A K-type thermocouple is used to measure the ambient air temperature at different locations. An optimal backlit setup was used in this experiment [77]. Details of the experimental setup are shown in Figure 7.2. Both the nitrogen gas supply pressure and the water injection pressure were measured. The pressure drop occurred in the supply system was negligible, since no appreciable differences were noted in the two pressures gauges.

7.2.2. Nozzle Geometry

Plain orifice nozzles were designed and machined for this study. The orifice plate was installed in the orifice assembly. The orifice assembly comprises of a cylindrical chamber with 5mm in diameter and 32mm in length, which is used to deliverer the water to the orifice plate, as shown in Figure 7.3. The orifice plates were fabricated using stainless steel. The circular and non-circular orifices were machined using wire-cut electro discharge machining (EDM) process. The geometrical details of the circular and rectangular orifices are provided in Table 7.2.

7.2.3. Spray visualization

High speed visualization techniques were employed to capture the flow behavior. A high speed camera (Phantom 4.3) with a Nikon® 50mm f/1.8 lens was used. To get higher light collection efficiency, an optimal optical system for back-illuminated imaging was applied to the low pressure jet. An engineered diffuser was used to distribute an extended light source through a controlled range of angles, and a field lens was used to redirect the light to the camera. The pixel resolution was set as 32×600, which enabled revealing the details of the jet breakup regime. The captured resolution is converted to 1.78 mm×33.33 mm in physical area. For each injection pressure, water was injected 3 times. The video files in *cine* format from the high speed camera were processed to output static spray images in *png* format. Image processing was then carried out on these images and related parameters were calculated for each measurement over 2000 images. The final values of the breakup length and wave length were obtained by taking the average of the 2000 images for each measurement over 3 repeatable measurements.

7.3. Results and discussions

7.3.1. Mass flow rates measurement

The mass flow rate of the liquid jet was measured for the circular and rectangular orifices. Three repeated measurements were conducted under different pressures in room temperature. The final values were the averages of three measurements. As illustrated in Table 7.4, the increasing of mass flow rates reveals a square root relation with the increasing injection pressure for both circular and rectangular jet. This mass flow rate relationship follows the basic fluid dynamics principle and indicates the reliable experiment results. In order to study the evaporation effect on liquid jet breakup behavior, the flow rates under 5 different ambient temperatures were measured, which is from 20°C to 60°C. The mass flow rate under room temperature of 20°C was set as the baseline. The evaporation rate is calculated based on the water mass difference between the baseline and the values under higher temperatures. Figure 7.5 and Figure 7.6 show the evaporation rates for circular jet and rectangular jet separately. It can be seen that the evaporation rate changes as a function of the jet velocity. The changing rate is not linear, but higher temperature leads to higher evaporation rate for both jets.

7.3.2. Non-dimensional number

Liquid jet breakup and spray characteristics often depend on the fluid flow conditions, which can be well represented by different non-dimensional numbers. Based on the mass flow rate, the liquid jet exit velocity was obtained as follows:

$$\dot{m}_l = \rho_l A_0 v \quad (7-1)$$

where A_0 is the orifice area and v_0 is the exit velocity of the liquid jet. The same jet exit velocity is used for calculating the non-dimensional numbers such as Reynolds number and Weber number in order to characterize the flow conditions at different injection pressures and temperatures. Reynolds number (Re) is a dimensionless ratio of the inertial force of the jet to the viscous force of the fluid:

$$\text{Re} = \frac{\rho_l D v}{\mu} \quad (7-2)$$

where ρ_l is the fluid density, D is the hydraulic diameter of the orifice, and μ is the dynamic viscosity of the fluid. The variation of the Reynolds number for the flow from circular and rectangular orifices at varying pressure conditions is presented in Figure 7.7. It can be noted that rectangular shaped orifice has larger Reynolds number than circular orifices under lower injection pressures.

The other important parameter for characterizing the jet breakup is the Weber number (We), which gives the ratio between the fluid inertia and the surface tension force. It is defined as:

$$\text{We} = \frac{\rho_l D v^2}{\sigma} \quad (7-3)$$

where, ρ_l is the fluid density, D is the hydraulic diameter of the orifice, and σ is the fluid surface tension. The hydraulic diameter of rectangular orifices can be calculated as:

$$D_H = \frac{4A}{P} \quad (7-4)$$

where A is the cross sectional area and P is the wetted perimeter of the cross-section. With the variation in jet exit velocity, the Weber number for the jet liquid as well as the ambient gas changes. As mentioned earlier, the criteria of different jet breakup regime are defined based on the value of air Weber number only, in which the liquid density in Equation (7-5) is replaced with gas density. The variation in We_g are shown in Figure 7.8 and Figure 7.9 for the circular and rectangular orifices. It can be seen that higher temperature leads to higher Weber numbers, but only a slight change is found under different temperatures.

The detailed values of Reynolds number (Re) and Weber number (We) are illustrated in Table 7.5 to Table 7.6. It can be seen that the maximum Weber numbers for both nozzles are less than the critical value defined for the atomization region, so all the present studies are located in the Rayleigh breakup and wind-induced regimes. The corresponding value of the air Weber number is below 0.4 for pressures up to 10psi. Thus, until 10psi the circular jet is within Rayleigh breakup regime. For rectangular jet, the Rayleigh breakup regime occurs under 15psi.

7.3.3. Breakup length analysis

Liquid jet behavior was recorded using the high speed camera. The *cine* format files were processed using the Image Processing Toolbox of MATLAB. Each frame of the *cine* format files was converted into a static image in *png* format. A background image without liquid jet was also recorded. After removing the background noise and adjust the contrast between the background and liquid jet, the liquid jet images were then subjected to edge detection using Canny edge detection algorithm. The binary images were obtained for the

calculation of the jet breakup length. The image was analyzed along its length and the first location of jet detachment was marked as the breakup point. The jet breakup length was finally converted to the real scale based on the pixel to length (mm) ratio.

In order to compare the evaporation effect on liquid jet breakup, the images of the circular jets at different ambient temperature are shown in Figure 7.10 to Figure 7.14. At lower velocities the jet surface behaves similarly for both non-evaporating and evaporating jet. The liquid jet structure is smooth and its breakup is well controlled by Rayleigh instability. However, a small increase of the jet velocity causes the surface to become wavy and unstable. These characteristic surface waves start at the very beginning of the jet at higher velocities. The breakup length of liquid jet also changes as the results of this small disturbance. Figure 7.15 illustrates the variation on the breakup length of the circular jet under different experimental conditions. At room temperature (20°C), the general shape of the breakup length-jet velocity curve is similar to the previous study [103]. The results clearly show that a small temperature disturbance can quickly induce a surface disturbance which eventually causes the breakup of the jet. Such temperature disturbance is readily available in most natural processes, because upon exiting from the nozzle the liquid temperature is usually slightly different than the ambient temperature. In other words, the initial thermal disturbance only induces a small surface disturbance which basically governs the instability of the jet under low jet velocity condition. As the jet velocity increases, the temperature disturbance on liquid jet breakup becomes smaller.

Figure 7.16 to Figure 7.20 show the images of rectangular jets at different ambient

temperatures. Due to the aspect ratio effect in rectangular orifice, the surface wave is generated from the nozzle exits. In Rayleigh breakup regime, a smooth wave is formed on the jet surface. As the jet velocity increases, the interaction between the surface tension force and aerodynamic force becomes stronger. The fluctuations on surface wave are observed in wind-induced regimes. As the ambient temperature increases, the surface disturbance is occurred early as shown in the figures. The breakup length was calculated based on the average value of 2000 images. For low ambient temperature condition, the breakup length of the rectangular orifice has the same trend with the circular one as indicated in Figure 7.21. At high ambient temperatures, the breakup length increases linearly with jet velocity. This indicates the influence of ambient temperature becomes weaker as the jet velocity increases.

7.3.4. Wave length analysis

As seen in Figure 7.16 to Figure 7.20, regular surface waves are found for the rectangular orifice nozzle. The surface wave structures were obtained by applying edge detection to the jet images. Canny edge detection algorithm was applied based on different thresholds to provide the accurate results of surface wave structure. Regular surface wave was obtained under low jet velocity and low ambient temperature as discussed earlier. In order to obtain a correlation for all the experimental conditions, different image processing steps were applied. Breakup length was calculated based on each frame. The final value was the average of all frames. The advantage of this process is to show the transient change of these characteristics. For the maximum wavelength calculation, it is really difficult to obtain the structure under high velocity and high ambient temperature conditions. Therefore, the

averaged images were used to process these variables. Each image is the average of 2000 individual ones as showed in Figure 7.22. This enables the visualization of the regular surface structure for high jet velocity. The maximum wavelength is considered as the distance between two peak values of surface wave profile and is converted into the real scale based on different pixel to length (mm) ratio.

Figure 7.23 illustrates the maximum wavelength of rectangular jet under different ambient temperatures. It is seen that a higher ambient temperature leads to a larger wave length at low jet velocity. As the velocity increases, the difference in wavelengths becomes close. The maximum wavelength is found varying linearly with the jet velocity. The high R square value (0.998) indicates that the jet velocity correlates with the maximum wavelength of the rectangular jet very well.

7.4. Summary

Plain-orifice nozzles were designed and applied in this study in order to investigate the effect of evaporation on liquid jet breakup. Circular and rectangular shaped orifice nozzles were both studied. The mass flow rate was measured for both nozzles under different injection pressures. The evaporation rate was also measured under different ambient temperatures. Both injection pressure and ambient temperature effects on liquid jet breakup length were analyzed by post-processing the jet images. Liquid jet behavior was compared for ten different injection pressures and five ambient temperatures.

The effect of the ambient temperature on liquid jet breakup length was found to have

a significant influence under low jet velocity condition (Rayleigh breakup regime). The linear relationship between jet velocity and breakup length was found for both nozzles under high ambient temperature. The correlation between non-dimensional number and jet characteristics were also studied.

Regular surface wave was found on rectangular jet surface. The maximum wave length was calculated for all experimental conditions. Averaged images were used to get the surface for image processing for high ambient temperature and high velocity jets. A linear relationship was obtained between the jet velocity and maximum wave length for rectangular jet.

7.5. Table and figures

Table 7.1 Classification of jet breakup regimes

Regime	Rectangular orifice
Rayleigh breakup	$We_G < 0.4$
First wind-induced breakup	$0.4 < We_G < 13$
Second wind-induced breakup	$13 < We_G < 40.3$
Atomization	$We_G > 40.3$

Table 7.2 Geometrical details of the orifices

Nozzle parameter	Circular orifice	Rectangular orifice
Nozzle orifice hydraulic diameter (mm)	0.296	0.215 (0.13x0.56)
Nozzle orifice length (mm)	1.27	1.27
Length /Diameter ratio	4.3	5.9

Table 7.3 Physical properties under different temperatures

Temperature (oC)	20	30	40	50	60
Density of water (kg/m ³)	998.23	995.68	992.25	988.07	983.24
Density of Air (kg/m ³)	1.204	1.153	1.137	1.105	1.057
Viscosity (mPa-s)	1.002	0.798	0.653	0.547	0.467
Surface Tension (mN/m)	72.86	71.2	69.6	67.9	66.2

Table 7.4 Reynolds number for different flow conditions

Pressure (psi)	1	2	3	4	5
Circular	987.9	1288.8	1587.4	1739.8	1990.9
Rectangular	659.2	859.9	1059.2	1160.9	1328.5
Pressure (psi)	10	15	20	25	30
Circular	2840.7	3552.4	4030.0	4382.3	4820.7
Rectangular	1895.4	2370.3	2689.0	2924.0	3216.6

Table 7.5 Weber number of liquid for different flow conditions

Pressure (psi)	1	2	3	4	5
Circular	45.4	77.3	117.3	140.8	184.4
Rectangular	27.7	47.1	71.5	85.9	112.4
Pressure (psi)	10	15	20	25	30
Circular	375.5	587.2	755.7	893.6	1081.3
Rectangular	228.9	358.0	460.7	544.8	659.2

Table 7.6 Weber number of air for different flow conditions

Pressure (psi)	1	2	3	4	5
Circular	0.0547	0.0930	0.1411	0.1695	0.2990
Rectangular	0.0004	0.0567	0.0860	0.1034	0.1353
Pressure (psi)	10	15	20	25	30
Circular	0.7592	1.4276	2.1467	2.9040	3.9567
Rectangular	0.2755	0.4309	0.5545	0.6557	0.7935

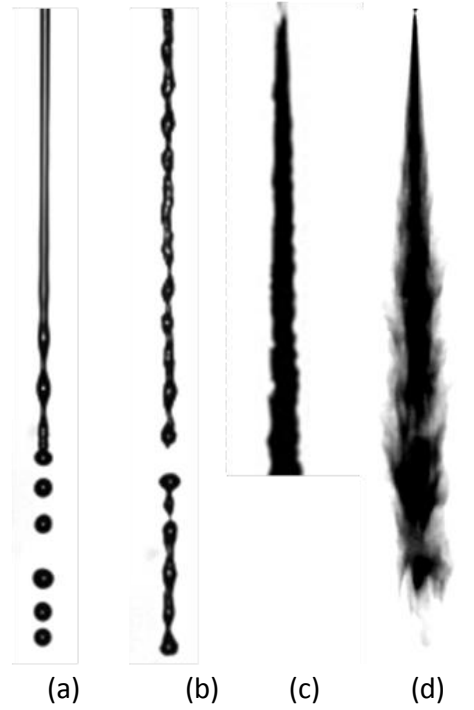


Figure 7.1 External flow structure of circular jet in different breakup regimes: (a) Rayleigh breakup regime. (b) First wind-induced breakup regime. (c) Second wind-induced breakup regime. (d) Atomization regime.

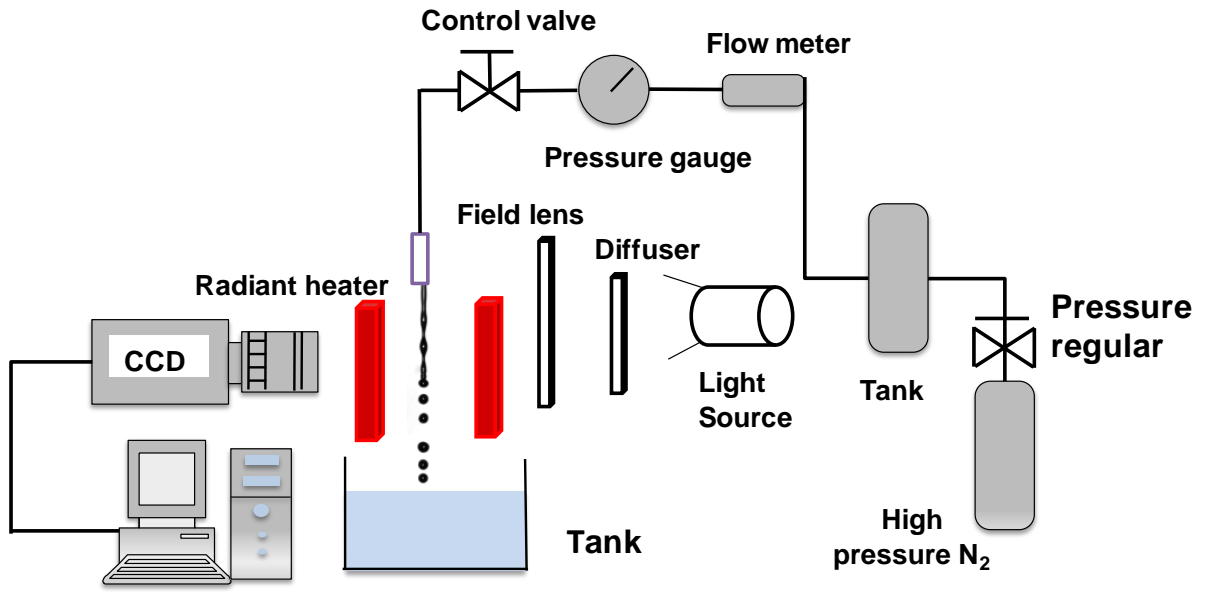


Figure 7.2 Experiment setup of pressure injection system

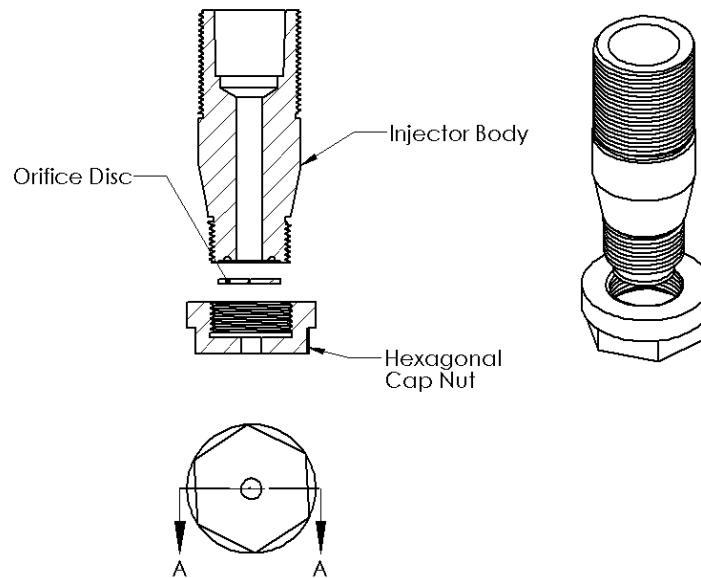


Figure 7.3 Details of the plain-orifice nozzle

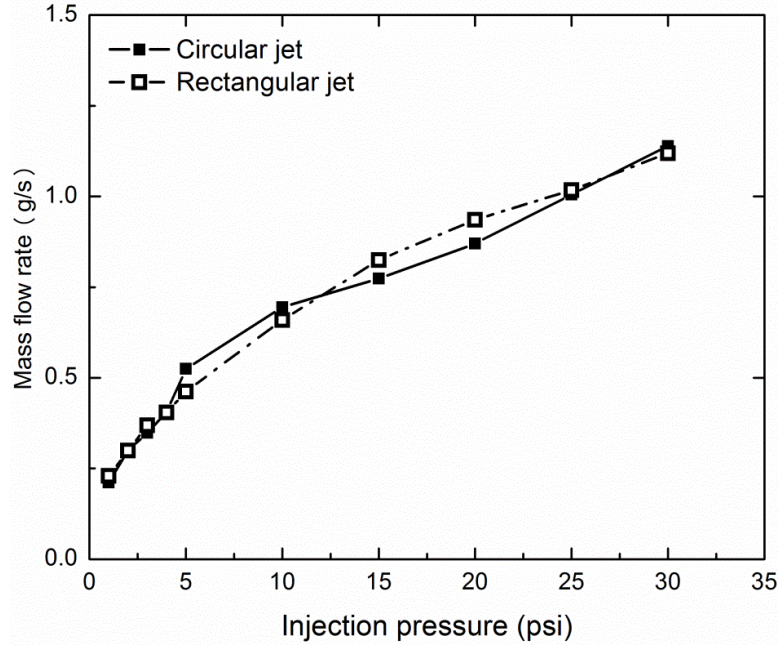


Figure 7.4 Mass flow rates of two liquid jets under different injection pressures

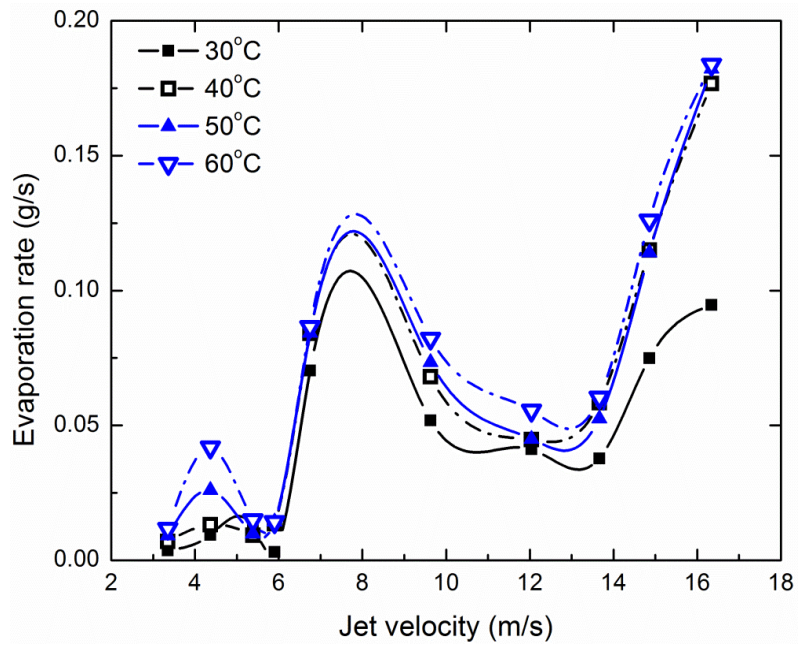


Figure 7.5 Evaporation rate for circular orifice nozzle

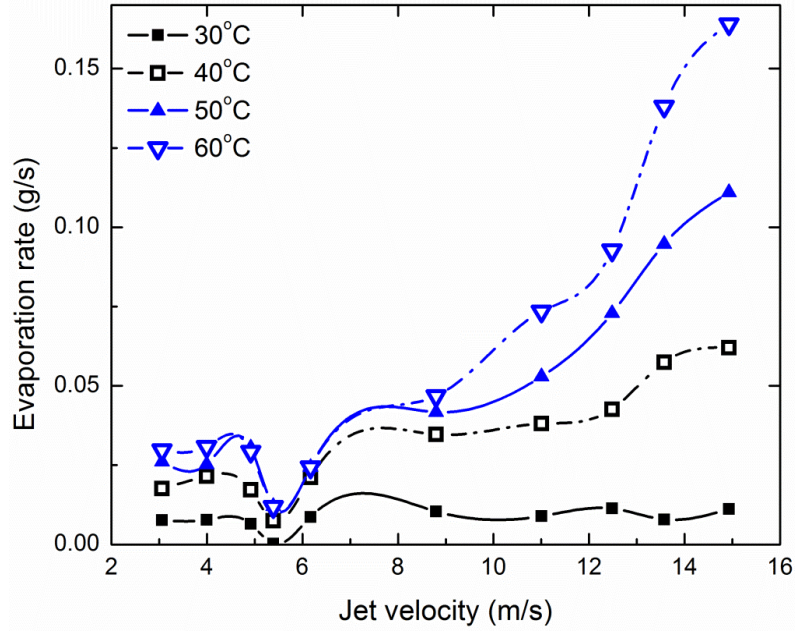


Figure 7.6 Evaporation rate for rectangular orifice nozzle

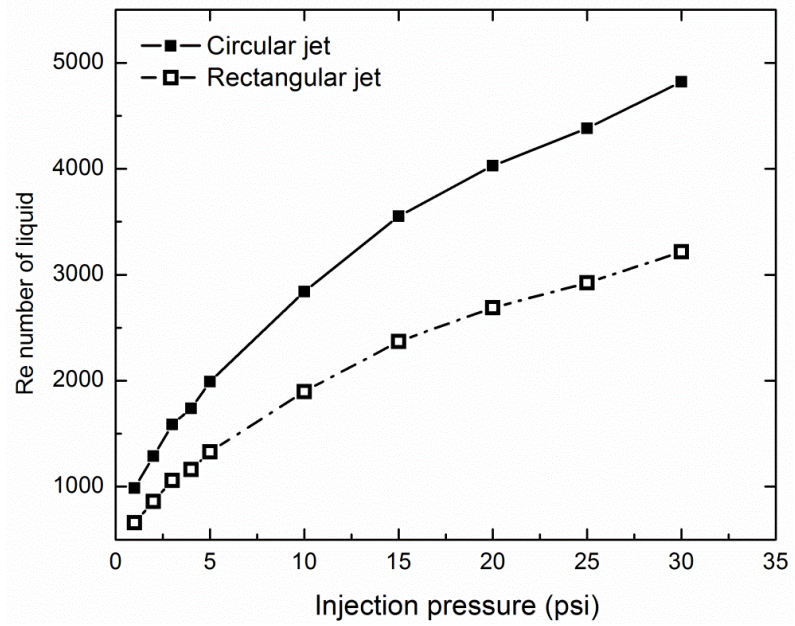


Figure 7.7 Reynolds number of liquid under different injection pressures

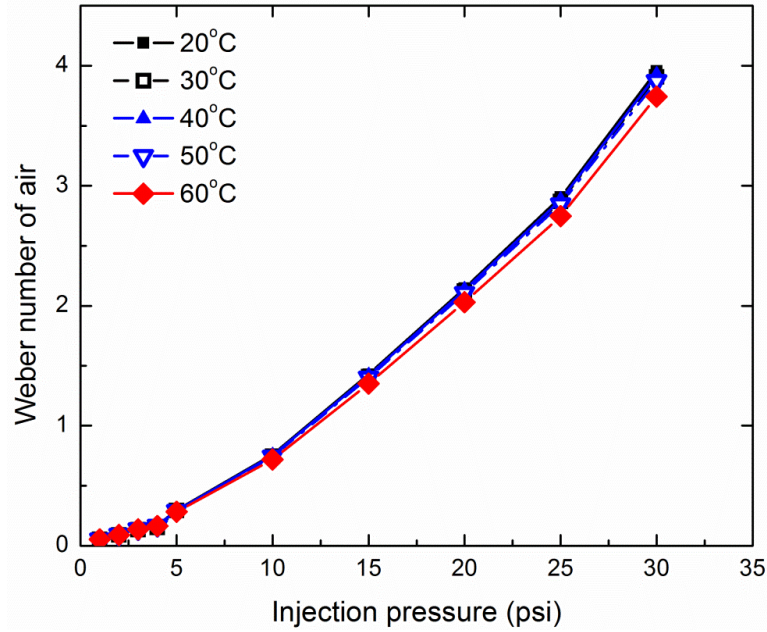


Figure 7.8 Weber number of air under different temperatures for circular jet

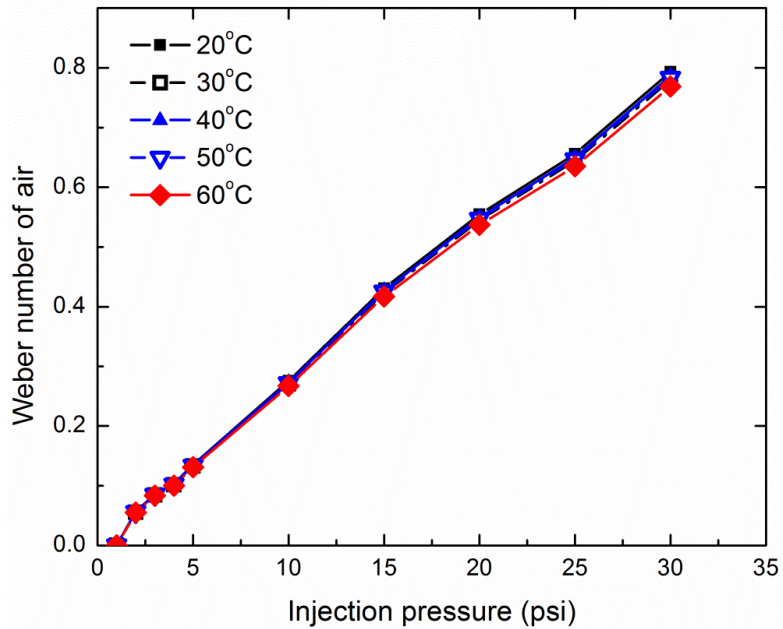
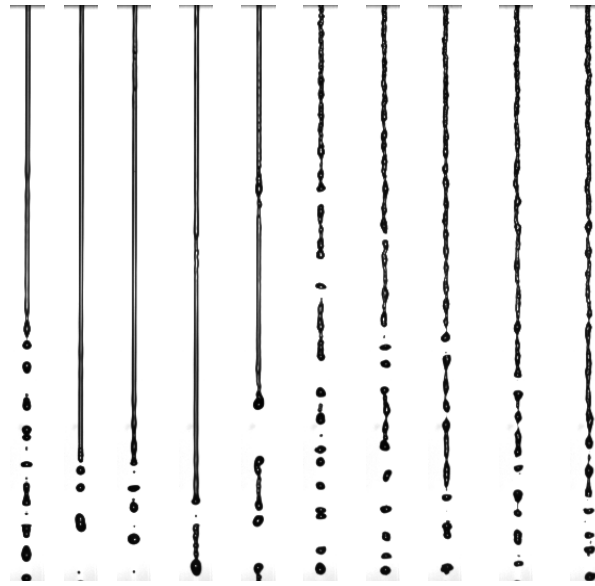
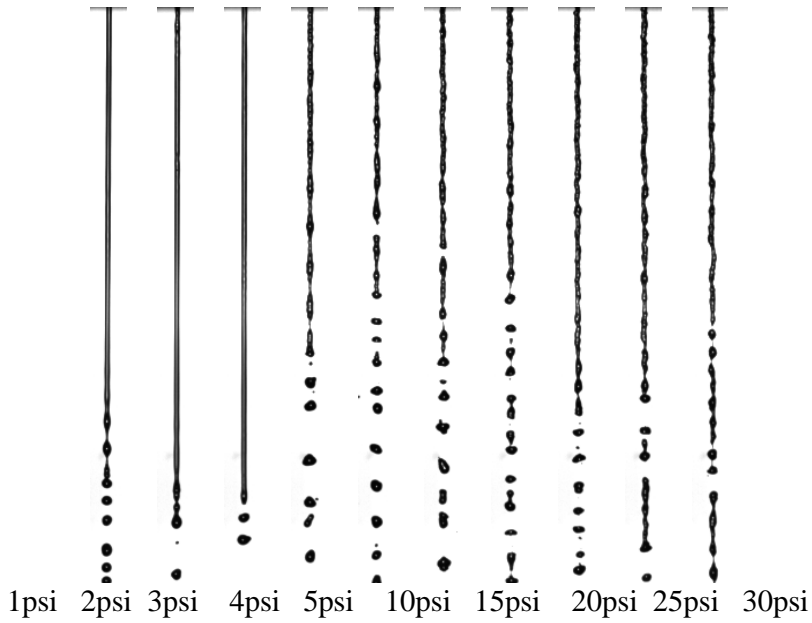


Figure 7.9 Weber number of air under different temperatures for rectangular jet



1psi 2psi 3psi 4psi 5psi 10psi 15psi 20psi 25psi 30psi

Figure 7.10 Transient images of circular jet under different pressures at 20°C



1psi 2psi 3psi 4psi 5psi 10psi 15psi 20psi 25psi 30psi

Figure 7.11 Transient images of circular jet under different pressures at 30°C

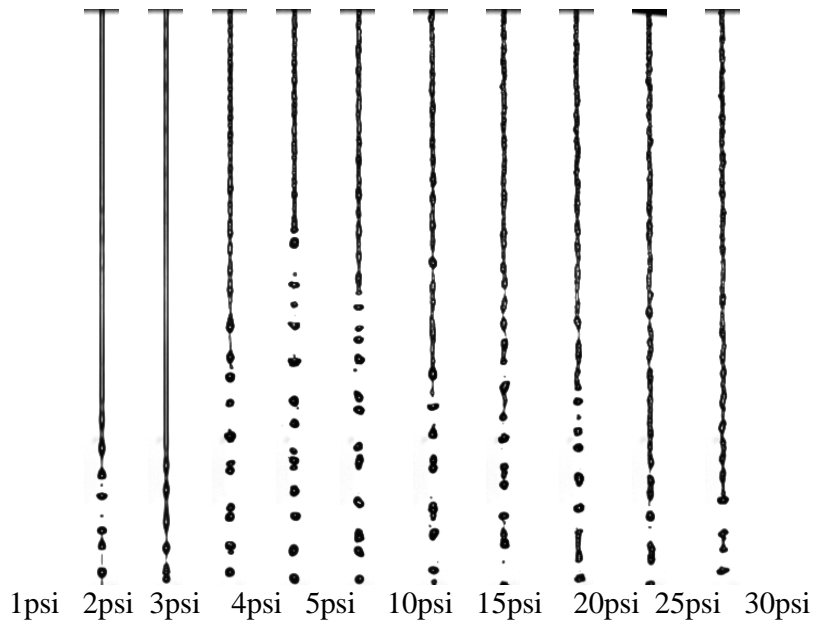


Figure 7.12 Transient images of circular jet under different pressures at 40°C

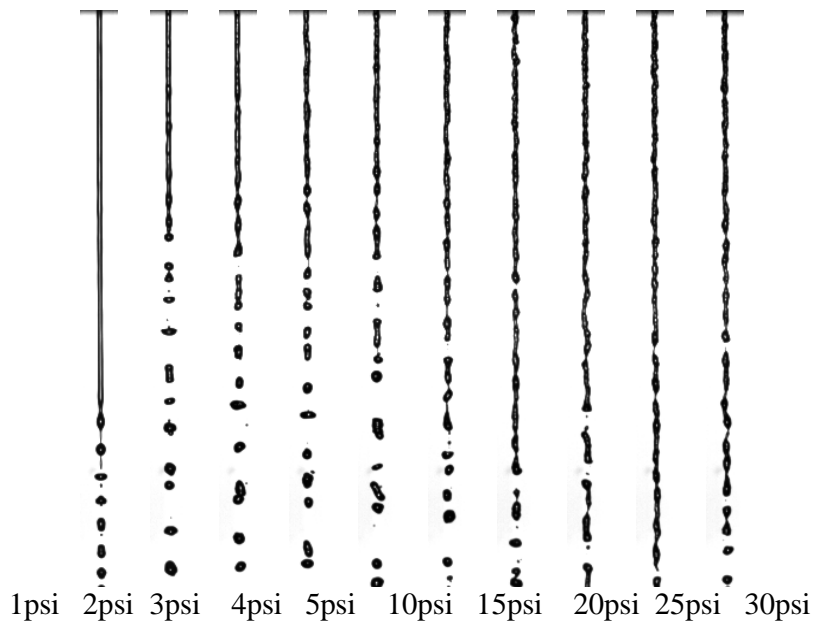


Figure 7.13 Transient images of circular jet under different pressures at 50°C

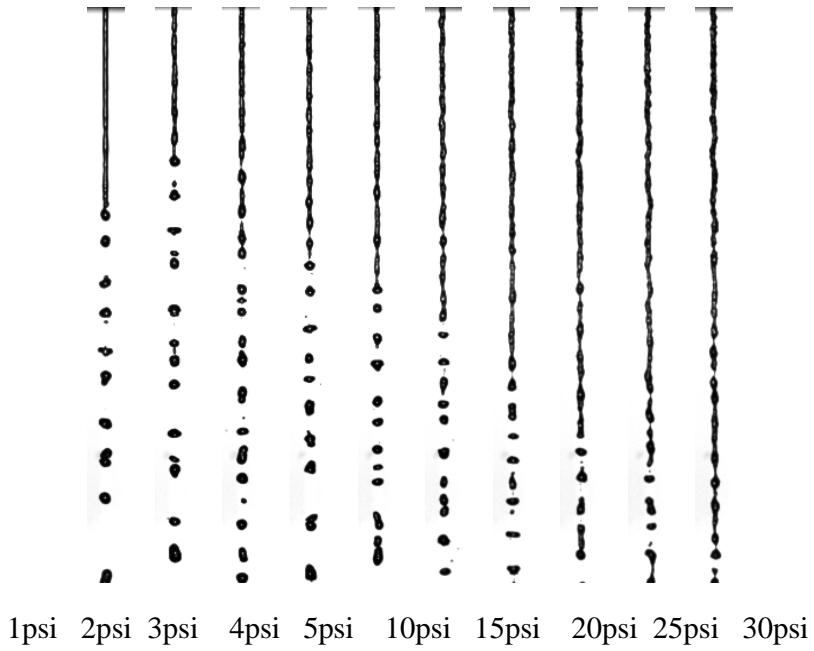


Figure 7.14 Transient images of circular jet under different pressures at 60°C

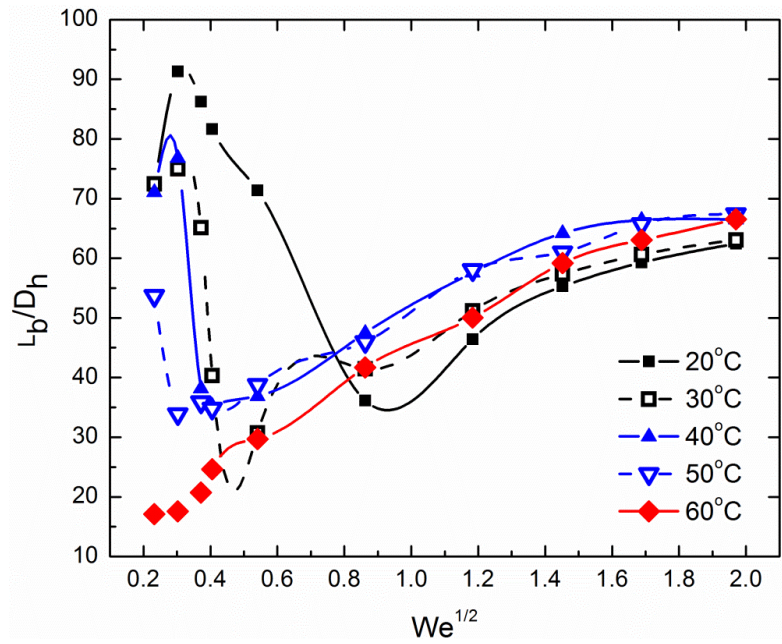


Figure 7.15 Breakup lengths under different temperatures for circular orifice nozzle

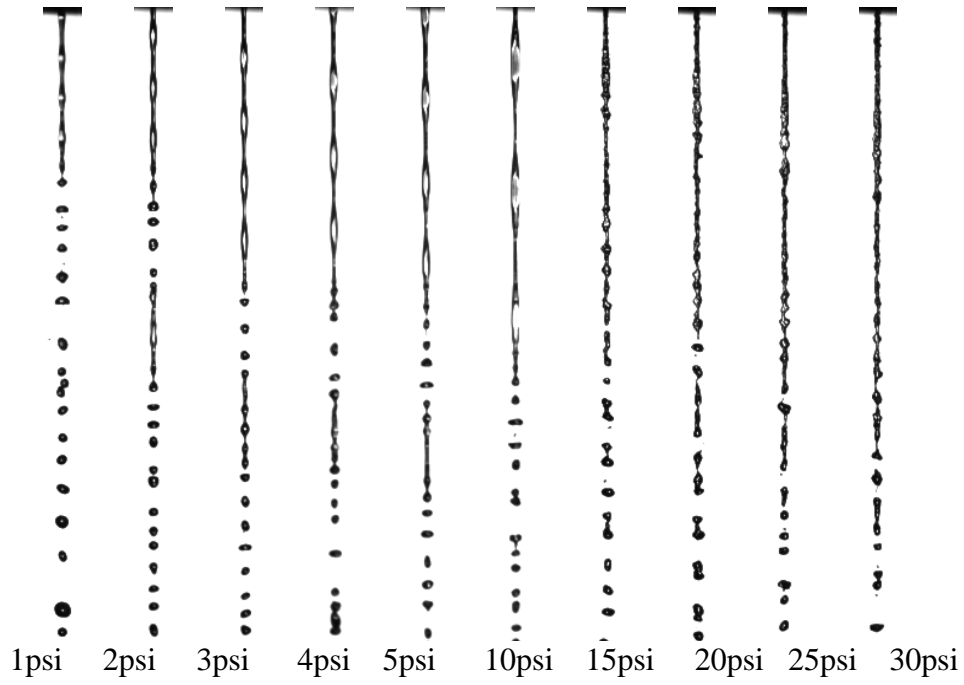


Figure 7.16 Transient images of rectangular jet under different pressures at 20°C

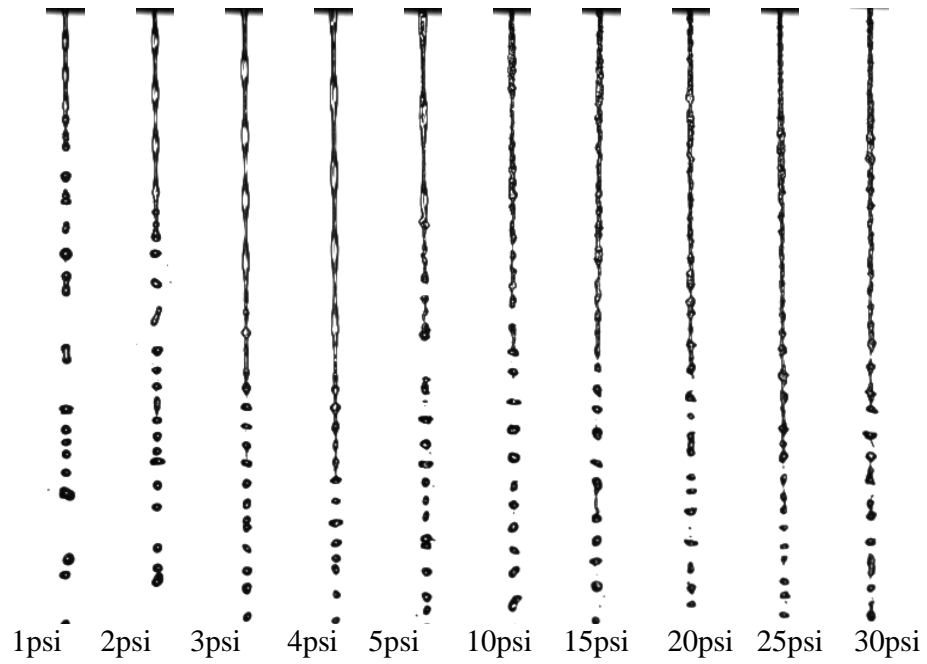


Figure 7.17 Transient images of rectangular jet under different pressures at 30°C

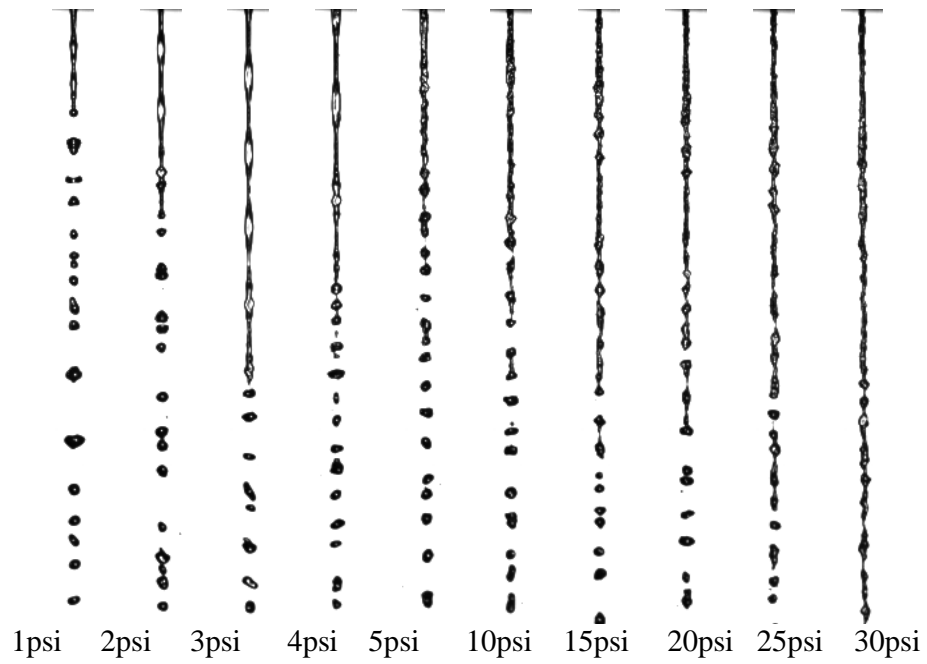


Figure 7.18 Transient images of rectangular jet under different pressures at 40°C

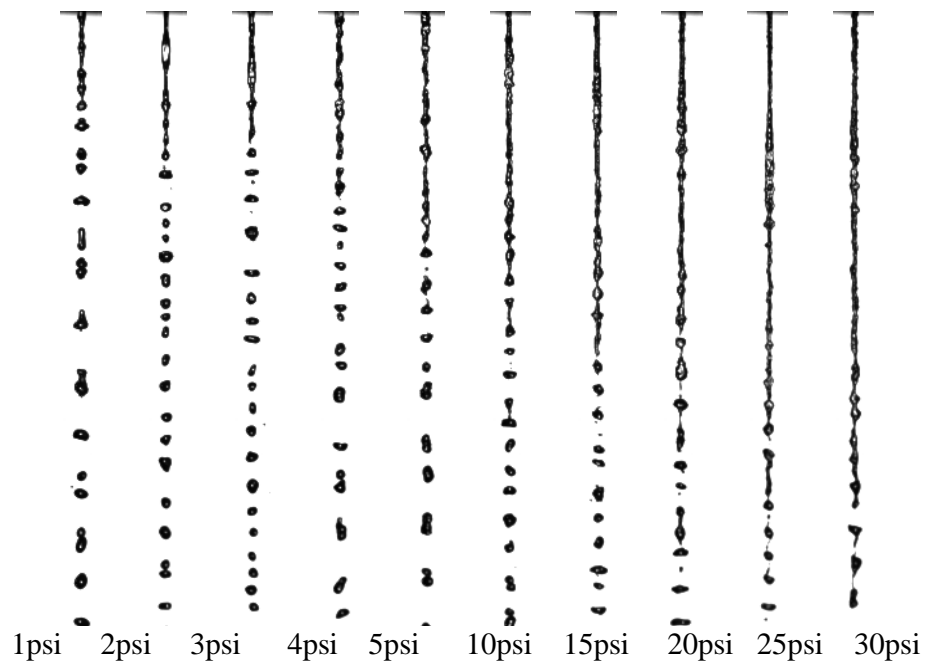


Figure 7.19 Transient images of rectangular jet under different pressures at 50°C

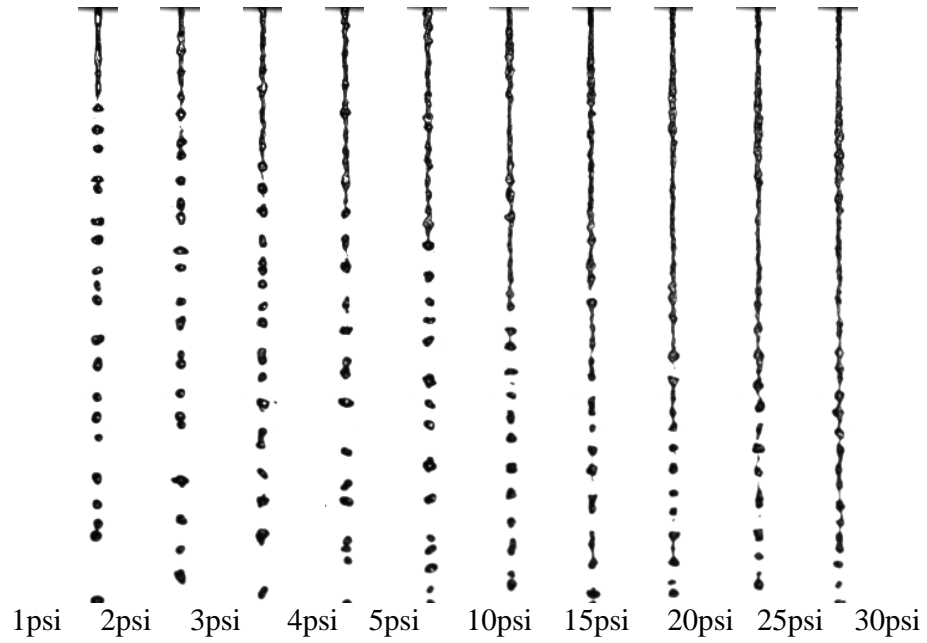


Figure 7.20 Transient images of rectangular jet under different pressures at 50°C

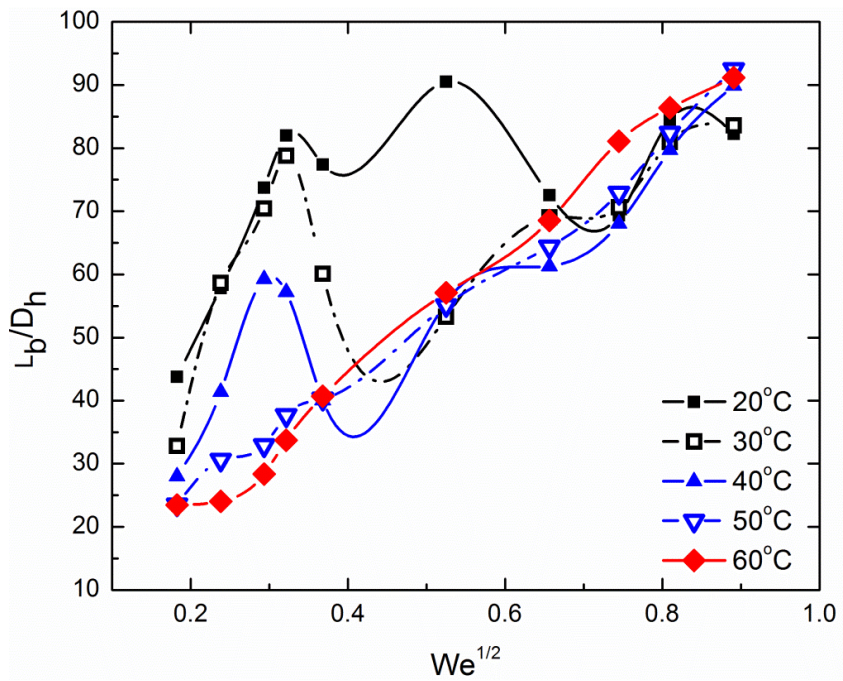


Figure 7.21 Breakup length change for rectangular orifice nozzle

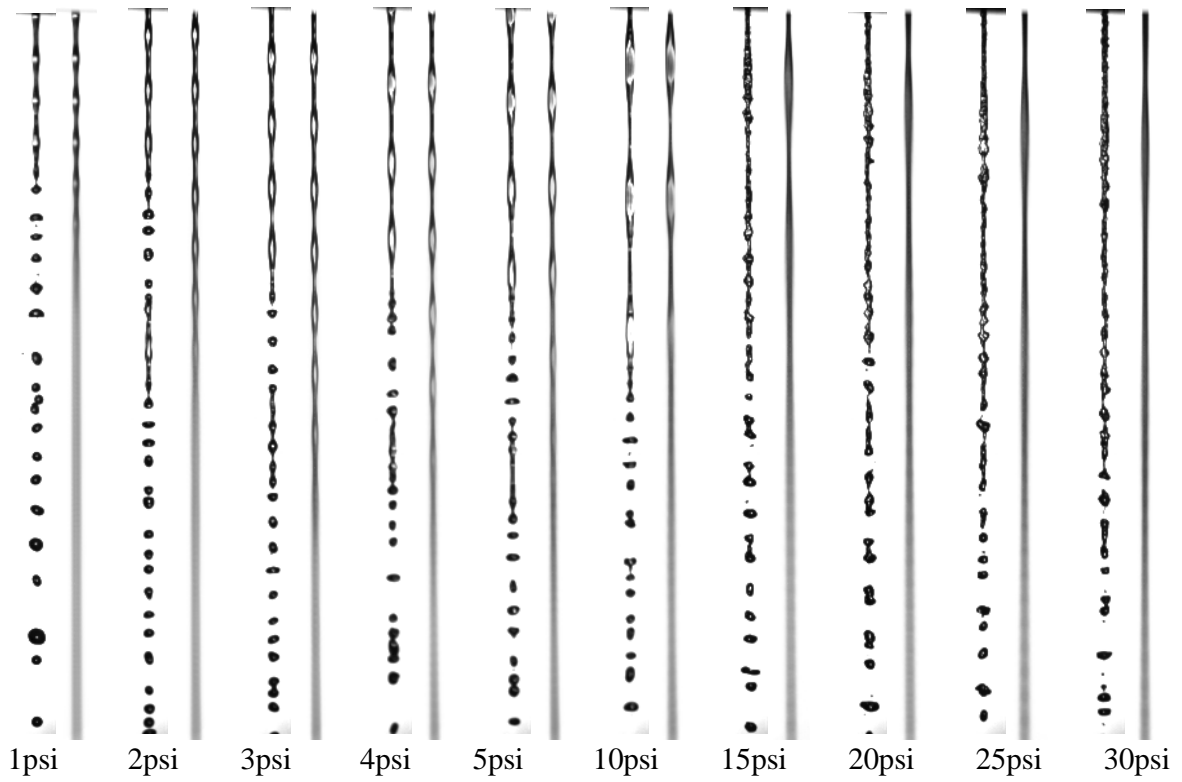


Figure 7.22 Transient and averaged images of rectangular jet at 20 °C

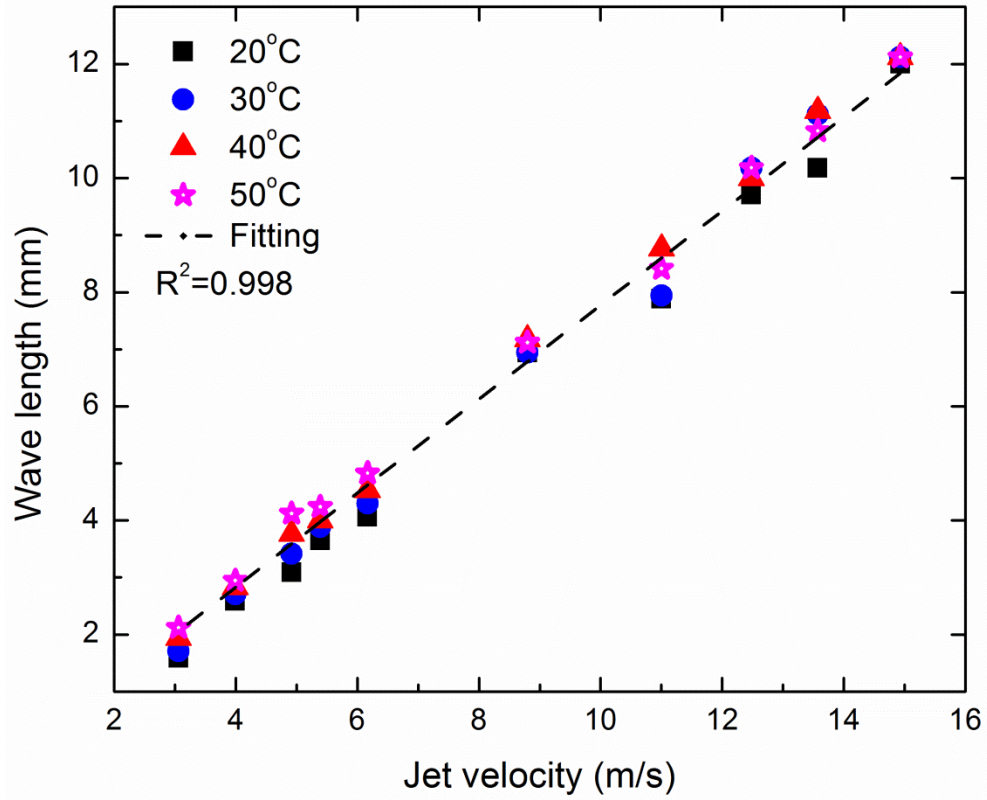


Figure 7.23 Maximum wave length of rectangular orifice nozzle

8. CONCLUSIONS

8.1. Conclusions

As stated in the beginning of this thesis, spray systems have found many applications in industrial processes. The spray characteristics usually affect the performance of these applications. Although there have been many studies on spray systems, investigations on spray structures and instabilities in swirling atomizers are still lacking, especially quantitative measurements. One main subject of this work was to design an experimental bench to allow spray characterization with small uncertainties. It was found that a carefully controlled experimental environment and high quality image processing are very important to achieve this goal. The first application of the designed experimental system and analytic tools was to study the effect of fluid viscosity on spray development, including the global spray structure, breakup process, droplet size and distribution.

The liquid mixtures by blending water and glycerol in different ratios were used to simulate fluids with drastically different viscosities. Compared to the changes in liquid viscosity, the changes in density and surface tension for the blended mixtures are relatively small. So, studies on the glycerol-water mixtures can represent primarily the effect of liquid viscosity. In the experiments, the near nozzle region of the liquid spray from a swirl atomizer was visualized using a high speed camera with strong background luminescence. By monitoring the displacement sensor data, it was found the fluid viscosity has a large impact on the movement of the dispensing piston in the swirl atomizer during the transient liquid dispensing process. From the obtained high speed images, the spray cone angle was

calculated for 0% to 80% glycerol-water mixtures, and it is confirmed that liquid viscosity has a significant effect on spray cone angle and breakup in swirl atomizers. Higher viscosity prevents fluid from forming a large cone, which results in smaller angles in the liquid cone formation. The breakup of high viscous fluid was found to be more difficult as compared to the less viscous fluid. Performing Fast Fourier Transform (FFT) analysis to the spatial images at fixed locations in time sequence allows converting the spatial information into temporal information. In this way, the frequencies of the temporal waves on the surface of the spray can be calculated. It was found that the wave frequency does not depend on the location on the liquid cone and the frequency decreases with time for all the fluids. The measurements on droplet size and distribution revealed that fluid viscosity has some impacts on spray downstream droplet formation, but compared to the effect on spray global structure and primary breakup, such effect is relatively small.

Another important fluid physical property that can significantly affect spray development is fluid surface tension. Therefore, the second research focus was specifically designed to study the effect of fluid surface tension on spray characteristics. The employed methods are the same methods used in the first study. The fluid mixtures were blended using water and ethanol. This allows a large variation of liquid surface tension with different ethanol volume ratios, but the liquid viscosity and density remain relatively constant. It was found that fluids with different surface tensions do not have a major impact on spray cone angle and breakup length in swirl atomizers in the near nozzle region. Spray cone angle slightly decreases with increasing ethanol volume ratio (decreasing surface tension). The

breakup length is found to decrease slightly as ethanol volume ratio increases. But compared to the results obtained in the first study for liquid viscosity, these changes are relatively small. However, it was found that the liquid surface tension has a significant effect on the droplet size. The results show that the droplet size decreases with the increase of ethanol volume ratio rapidly. In addition, the location for size measurement also influences droplet size. Smaller droplet size was found at the locations away from the nozzle axis in the vertical direction. In the horizontal direction, larger droplets were found at the locations closer to the nozzle exit. Different from the first study, FFT analysis was not performed because the current camera speed is not high enough to capture images in a short time period required to resolve the high surface frequency by using the water-ethanol mixtures. This should be a subject of the future work. Together with the observations in the first study, it is concluded that liquid surface tension has a crucial effect on secondary spray breakup, but liquid viscosity has a major effect on the primary breakup.

With the main liquid physical properties being studied on the spray characteristics in the outside region of swirl atomizers, the third research focus shifted the focus to the in-nozzle flow. In order to visualize the in-nozzle flow in swirl atomizers, transparent swirl atomizers with different nozzle orifice sizes were designed and installed in the experimental bench. Both injection pressure and fluid viscosity effects on liquid film thickness were analyzed by post-processing images. It was found that the measured film thickness decreases as injection pressure increases. As the injection pressure rises, the effect of the injection pressure on liquid film thickness becomes less significant indicating a non-linear effect of the

injection pressure. Fluid viscosity plays a crucial role in controlling the liquid film thickness. The liquid film thickness becomes larger as the viscosity increases and the change is small for low viscosity fluid and much bigger for high viscous fluid. But under the present experimental conditions, the effect of injection pressure is more pronounced than the fluid viscosity.

The last research task was designed to study the effect of evaporation on the primary breakup of steady state liquid sprays. Plain-orifice nozzles were designed and applied in this study. Circular and rectangular shaped orifice nozzles were both studied. The mass flow rate and the evaporation rate were measured under different ambient temperatures for both nozzles. The injection pressure and ambient temperature effects on liquid jet breakup length were analyzed by post-processing the jet images. Liquid jet behavior was compared for ten different injection pressures and five ambient temperatures. The effect of the ambient temperature on liquid jet breakup length was found to have a significant influence under low jet velocity condition (Rayleigh breakup regime). The correlations between non-dimensional number and jet characteristics were also studied. Regular surface waves were found on the rectangular jet surface. The maximum wave length was calculated from the averaged jet images. A good linear relationship was obtained between the jet velocity and maximum wave length for the rectangular jet.

8.2. Future work

Liquid spray and atomization are classical but very complex phenomena. This work focuses on revealing fundamentally important parameters that affect the performance of

liquid spray breakup and atomization. Other than the research tasks conducted by the author in this study, the following areas can be further explored to better understand the physical processes of liquid breakup and atomization on top of the discoveries found in this dissertation.

Pressure jet and swirl atomizer were selected to study the basic processes of spray breakup and atomization. In practice, there are many other types of atomizers, such as air-assist atomizer, airblast atomizer, rotary atomizer, electrostatic atomizer, and so on. The experimental methodologies employed in this study and the image processing techniques developed by the authors can be extended to study these atomizers of different geometries.

High speed imaging was the major experiment method applied in this dissertation. The frame rate of current hardware restricted the analysis on temporal wave frequency of highly viscous fluids. The resolution of the camera also limited the possibility to study the air core oscillation in the pressure swirl atomizer. The small disturbance on the internal liquid film is found to play an important role on the surface wave growth and propagation. But such detailed information is still lacking. It will make a significant contribution if the instabilities on internal and external flow surfaces can be simultaneously measured using a camera with higher speed and better resolution.

Droplet size and distribution were measured using laser diffraction technology. However, the droplet velocity information is still lacking which relies on PIV and PDPA measurements, as reviewed in Chapter 2. Supplemented by droplet velocity information, the current study can provide more valuable information to spray modeling studies and validations.

The experiment setup of the low pressure jet can be further improved. The ambient air can reach to higher temperature and make the evaporation rate larger by conducting in a closed area. Theoretical and analytic work will help to understand the flow behavior and physical process on the heating effect of evaporation on liquid jet breakup.

REFERENCES

1. Huntington, D.H. (2004). "The influence of the spray drying process on product properties," *Dry. Technol.*, 22, 1261–1287.
2. Nasr, G.G., R.A. Sharief and A.J. Yule (2006). "High pressure spray cooling of a moving surface," *J. Heat Transfer*, 12(8),752–760.
3. Li, B.Q., T. Cader, J. Schwarzkopf, K. Okamoto and B. Ramaprian (2006). "Spray angle effect during spray cooling of microelectronics: experimental measurements and comparison with inverse calculations," *Appl. Therm. Eng.*, 26, 1788–1795.
4. Zhao, F., M.C. Lai and D.L. Harrington (1999). "Automotive spark ignited direct injection gasoline engines," *Prog. Energy Combust. Sci.*, 25, 437–562.
5. Nouri, J.M. and J.H. Whitelaw (2001). "Spray characteristics of a gasoline direct injector with short durations of injection," *Exp. Fluids*, 31, 377–383.
6. Rontondi, R. and G. Bella (2006). "Gasoline direct injection spray simulation," *Int. J. Therm. Sci.*, 45, 168–179.
7. Abdelkarim, N.B.H., S.S. Ibrahim, A.R. Masri and G. Wigley (2007). "Gasoline sprays injected at different back pressures: calculations using two atomization models," *Atomization Sprays*, 17, 233–265.
8. Singh, A., M. Mehregany, S.M. Phillips, R.J. Harvey and M. Benjamin (1998). "Micromachined silicon fuel atomizers for gas turbine engines," *Atomization Sprays*, 8, 405–418.
9. Alkabie, H. (2000). "Design methods of the ABB ALSTOM POWER gas turbine dry low emission combustion system," *Proc. Inst. Mech. Eng.*, 214, 293–315.
10. Zhao, F., M.C. Lai and D.L. Harrington (1999). "Automotive spark-ignited direct-injection gasoline engines," *Prog. Energy Combust. Sci.* 25, 4–8.
11. Zhao, F., D.L. Harrington and M. Lai (2003). "Automotive Gasoline Direct- Injection Engines," Society of Automotive Engineers.
12. Lefebvre, A.H. (1989). "Atomization and Sprays," Hemisphere Publishing Corporation.
13. Han, Z., L. Fan and R.D. Reitz (1997). "Multidimensional modeling of spray atomization and air-fuel mixing in a direct-injection spark-ignition engine," *SAE Trans.* 106, 1423–1441.

14. Halder, M.R., S.K. Dash and S.K. Som (2002). "Initiation of air core in a simplex nozzle and the effects of operation and geometrical parameters on its shape and size," *Exp. Therm. Fluid Sci.* 26, 871–878.
15. Gavaises, M., C. Arcoumanis (2001). "Modelling of sprays from high- pressure swirl atomizers," *Int. J. Engine Res.* 12, 95–117.
16. Hagerty, W.W., and J.F. Shea (1955). "A study of the stability of plane fluid sheets," *J. Appl. Mech.* 22, 509–514.
17. Squire, H.B. (1953). "Investigation of the instability of a moving liquid film," *Brit. J. Appl. Phys.* 4, 167–169.
18. Cohen, J. M., and T. J. Rosfjord (1991). "Spray Patternation at High Pressure," *Journal of Propulsion and Power*, 7 (4), 481–487.
19. Santolaya, J. L., L. A. Aisa, J. A. Garcia, J. I. Palacin and E. Calvo (2003). "Drop Sizes and Mass Fluxes Development in a Pressure Swirl Hollow Cone Spray," Proceedings of the 9th ICLASS 2003.
20. Santolaya, J. L., L. A. Aisa, E. Calvo, J. A. Garcia and L. M. Cerecedo (2007). "Experimental Study of Near-Field Flow Structure in Hollow Cone Pressure Swirl Atomizers," *Journal of Propulsion and Power*, 23(2), 382–389.
21. Chen, S. K., A. H. Lefebvre and J. Rollbuhler (1992). "Factors Influencing the Effective Spray Cone Angle of Pressure Swirl Atomizers," *Journal of Engineering for Gas Turbines and Power*, 114, 97– 103.
22. Ramamurthi, K., and T. J. Tharakan (1995). "Experimental Studies of Liquid Sheets Formed in Coaxial Swirl Injectors," *Journal of Propulsion and Power*, 11(6), 1103–1109.
23. Jeng, S. M., M. A. Jog and M. A. Benjamin (1998). "Computational and experimental study of liquid sheet emanating from simplex fuel nozzle," *AIAA J.* 36 (2), 201.
24. Arai, T. and H. Hashimoto (1985). "Disintegration of a thin liquid sheet in a concurrent gas stream," Proceeding of the 3rd ICLASS, London, 1-7.
25. Kim, D., J. Im, H. Koh and Y. Yoon (2007) "Effects of Ambient gas density on spray characteristics of swirling liquid sheet," *Journal of Propulsion and Power*, 23(3), 603-611.
26. Rizk, N. K. and A.H. Lefebvre (1985). "Internal flow characteristics of simplex swirl atomizers," *Journal of Propulsion and Power*, 1(3), 193-199.

27. Brown, R. C., P. Andreussi, and S. Zanelli (1978). "Use of wire probes for the measurement of liquid film thickness in a gas-liquid flow," *Can. J. Chem. Eng.* 56,754.
28. Salazar, R. P. and E. Marschall (1975). "Thickness measurement in liquid film flow by laser scattering," *Rev. Sci. Instrum.* 46, 1539–41.
29. Zhang, J. T., B. X. Wang and X. F. Peng (2000). "Falling liquid film thickness measurement by an optical-electronic method," *Rev. Sci. Instrum.* 71, 1883–6.
30. Shedda, T. A. and T. A. Newell (2011). "Automated optical liquid film thickness measurement method," *Meas. Sci. Technol.* 22, 125403.
31. Smart, A. E. and R. A. J. Ford (1974). "Measurement of thin liquid films by a fluorescence technique," *Wear.* 29(1), 41–71974.
32. Makarytchev, S. V., T. A. G. Langrish and R. G. H. Prince (2001). "Thickness and velocity of wavy liquid films on rotating conical surfaces," *Chemical Engineering Science*, 56(1), 77–87.
33. Schubring, D., T.A. Shedd and E.T. Hurlburt (2010). "Planar laser-induced fluorescence (PLIF) measurements of liquid film thickness in annular flow," *International Journal of Multiphase Flow*, 36(10), 815–824.
34. Chang, J. S., Y. Ichikawa, G. A. Irons (1982). "Flow Regime Characterization and Liquid Film Thickness Measurement in Horizontal Gas-Liquid Two-Phase Flow by an Ultrasonic Method," AIAA/ASME Joint Plasma Thermophys. Heat Transfer Conf., St. Louis, Mo.
35. Lu, Q., N. V. Suryanarayana and C. Christodoulou (1993). "Film thickness measurement with an ultrasonic transducer," *Exp. Thermal Fluid Sci.*, 7, 354–361.
36. Chen, Z. Q., J. C. Hermanson, M. A. Shear and P. C. Pedersen (2005). "Ultrasonic monitoring of interfacial motion of condensing and non-condensing liquid film," *Flow Meas. Instrum.* 16, 353–364.
37. Klausner, J. F., L. Z. Zeng and D.M. Bernhard (1992). "Development of a film thickness probe using capacitance for asymmetrical two-phase flow with heat addition," *Rev. Sci. Instrum.*, 63, 3147–52.
38. Thorncroft, G. E. and J. F. Klausner (1997). "A capacitance sensor for two-phase liquid film thickness in a square duct," *Trans. ASME, J. Fluids Eng.*, 119, 164–9.
39. Suyari, M. and A. H. Lefebvre (1986). "Film Thickness Measurements in a Simplex Swirl Atomizer," *Journal of Propulsion and Power*, 2, 528–533.

40. Kim, S., T. Khil, D. Kim and Y. Yoon (2009). "Effect of geometric parameters on the liquid film thickness and air core formation in a swirl injector," *Meas. Sci. Technol.* 20, 015403.
41. Moon, S., C. Bae, E.F. Abo-Serie and J. Choi (2007). "Internal and near nozzle flow of a pressure-swirl atomizer under varied fuel temperature," *Atomization and Sprays*, 17, 529–550.
42. Halder, M.R., S.K. Dash and S.K. Som (2002). "Initiation of air core in a simplex nozzle and the effects of operating and geometrical parameters on its shape and size," *Exp. Thermal and Fluid Sci*, 26, 871–878.
43. Moon, S., E.F. Abo-Serie and C. Bae (2010). "Liquid film thickness inside the high pressure swirl injectors: Real scale measurement and evaluation of analytical equations," *Exp. Thermal Fluid Sci*, 34, 113–121.
44. Kutty, S., M.Narasimhan and K. Narayanaswamy (1978). "Design and Prediction of Discharge Rate, Cone Angle, and Air Core Diameter of Swirl Chamber Atomizers," *First International Conference on Liquid Atomization and Spray Systems*, Tokyo, Japan, Aug, 93-100.
45. Gardiner, J. A (1964). *Instrum. Pract.*, 18, 353.
46. Bachalo, W.D. (1980). "Method for measuring the size and velocity of spheres by dual-beam light scatter interferometry," *Appl. Opt.*, 19(3), 363-370.
47. Dobbins, R. A., L. Crocco and I. Glassman (1963). "Measurement of mean particle sizes of sprays from diffractively scattered light," *AIAA J.*, 1(8), 1882-1886
48. Mugele, R., and H. D. Evans (1951). "Droplet size distributions in sprays," *Ind. Eng. Chem.*, 43(6), 1317-1324.
49. Rayleigh, W. S (1878). "On the instability of jets," *Proc. London Math. Soc.* 4, 10.
50. Grant, R.P. and S. Middleman (1966). "Newtonian jet stability," *AIChE J.* 12, 669–678.
51. Haenlein, A. (1932). "On the disruption of a liquid jet)," *NACA TM Report*. 659.
52. Reitz, R. D. and F. V. Bracco (1982). "Mechanism of atomization of a liquid jet," *Phys. Fluids*. 25,1730–42.
53. Dombrowski, N. and R. P. Fraser (1954). "A photographic investigation into the disintegration of liquid sheets," *Phil. Trans.* 247(924), 101–130.

54. Dombrowski, N., D. Hasson and D.E. Ward (1960). "Some aspects of liquid flow through fan spray nozzles," *Chem. Eng. Sci.* 12, 35–50.
55. Fraser, R. P., P. Eisenklam, N. Dombrowski and D. Hasson (1962). "Drop formation from rapidly moving sheets," *AIChE J* 8(5), 672–680.
56. Dombrowski, N. and W. R. Johns (1963). "The aerodynamic instability and disintegration of viscous liquid sheets," *Chem, Eng. Sci.* 18, 203–214.
57. Senecal, P. K., D. P. Schmidt, I. Nouar, C. J. Ruthland, R. D. Reitz and M. L. Corradini (1999). "Modeling high speed viscous liquid sheet atomization, *Int. J. Multiphase Flows*," 25,1073–1097.
58. Rangel, R. H. and W. A. Sirignano (1999). "The linear and nonlinear shear instability of a fluid sheet," *Phys. Fluids A*, 3(10), 2392–2400.
59. Squire, H. B. (1953). "Investigation of the instability of a moving liquid film," *Brit. J. Appl. Phys.*, 4, 167–169.
60. Hagerty, W. W. and J. F. Shea (1955). "A study of the stability of plane fluid sheets," *J. Appl. Mech.*, 22, 509–514.
61. Sirignano, W. A. and C. Mehring (2000). "Review of theory of distortion and disintegration of liquid streams," *Prog. Energy Combust. Sci.*, 26, 609–655.
62. Ibrahim, E. A. and E. T. Akpan (1996). "Three-dimensional instability of viscous liquid sheets," *Atom. Sprays* 6, 649–665.
63. Sirignano, W. A. (1999). "Fluid Dynamics and Transport of Droplets and Sprays," Cambridge University Press, New York.
64. Crowe, C. T., M. Sommerfeld and Y. Tsuji (1998). "Multiphase Flows With Droplets and Particles," CRC Press, New York.
65. Sazhin, S. S. (2006). "Advanced models of fuel droplet heating and evaporation," *Progress in Energy and Combustion Science*, 32,162–214.
66. Rayleigh, W. S. (1882). "Further observations upon liquid jets," *Proc. London Math. Soc.*, 34, 130–145.
67. Nayfeh, A. H. (1970). "Non-linear stability of a liquid jet," *Phys. Fluids* 13, 841–847.
68. Ier, J. B. K., S. I. Rubinow and Y. O. Tu (1973). "Spatial instability of a jet," *Phys. Fluids*, 16, 2052–2055.

69. Sultan, E., A. Boudaoud and M. Amar (2005). "Evaporation of a thin film: diffusion of the vapor and Marangoni instabilities," *J. Fluid Mech.*, 543, 183–202,
70. Prosperetti, A. and M. Plesset (1984). "The stability of an evaporating liquid surface," *Phys. Fluids* 27, 1590-1603.
71. Higuera, F. J. (1987). "The hydrodynamic stability of an evaporating liquid," *Phys Fluids* 30, 679- 693.
72. Lian, Z. W. and R. D. Reitz (1993). "The Effect of Vaporization and Gas Compressibility on Liquid Jet Atomization," *Atomization Sprays* 3, 249–264.
73. Lin, S. P. and Z. W. Lian (1990). "Mechanism of the breakup of liquid jets," *AIAA Journal* 28, 120- 132.
74. Saroka, M., Y. Guo, and N. Ashgriz (2001). "Nonlinear Instability of an Evaporating Capillary Jet," *AIAA J.* 39, 1728–1734.
75. Kowalewski, T. A, and W. J. Hiller (1991). "Unsteady Droplet Evaporation," *Proceedings of 11th ABCM Mechanical Engineering Conference, Brasil.*
76. Kowalewski, T. A. and W. J. Hiller (1993). "An experimental study of evaporating small diameter jets," *Phys. Fluids A* 5, 8.
77. Ghandhi, J. B. and D. M. Heim (2009). "An optimized optical system for backlit imaging," *Rev. Sci. Instrum.* 80, 056105.
78. Inamura, T., H. Tamura and H. Sakamoto (2003). "Characteristics of Liquid Film and Spray Injected from Swirl Coaxial Injector," *J. Propul Power.* 19. 632–639. doi: 10.2514/2.6151
79. Yule, A. J. and J. J. Chinn (2000). "The Internal Flow and Exit Conditions of Pressure Swirl Atomizers," *Atomization Sprays*, 10, 121–146.
80. Katharina, K. H. and J. B. Jeffries (2002). "Applied Combustion Diagnostics, Combustion: An International Series," Taylor and Francis, London.
81. Kurosawa, R., K. Hishida and M. Maeda (2002). "Combined Measurement of LIF and ILIDS for Vapor Concentration and Droplets Size and Velocity in a Spray," 11th International Symposium on Applications of Laser Techniques to Fluid Mechanics.
82. Melton, L. A. (1983). "Spectrally Separated Fluorescence Emissions for Diesel Fuel Droplets and Vapor," *Appl. Opt.*, 22, 2224–2226.

83. Melton, L. and A. J. F. Verdieck (1985). "Vapor/Liquid Visualization for Fuel Sprays," *Combust Sci. Technol.*, 42, 217–222.
84. Yeh, C. N., H. Kosaka and T. Kamimoto (1993). "Fluorescence/Scattering Imaging Technique for Instantaneous 2-D Measurement of Particle Size Distribution in a Transient Spray," 3rd International Congress on Optical Particle Sizing.
85. Albrecht, H., E. M. Borys, N. Damaschke and C. Tropea (2003). "Laser Doppler and Phase Doppler Measurement Techniques," Springer, New York.
86. Chang, K. C., M. R. Wang, W.J. Wu and C. H. Hong (1993). "Experimental and Theoretical Study on Hollow-Cone Spray," *J. Propul Power.* 9, 28–34.
87. Khavkin, Y. (2001). "About Swirl Atomizer Mean Droplet Size," *Atomization Sprays*, 6, 160–178.
88. Rottenkolber, G., R. Meier, O. Schafer, S. Wächter, K. and Düllenkopf, S. (2000). "Witting, Combined PDA and LDV Measurements: Phase Discrimination Inside a Spray Using Fluorescence Seeding Particles," 10th International Symposium on Applications of Laser Techniques to Fluid Mechanics.
89. Zhang, Z. and S. Ziada (2000). "PDA Measurements of Droplet Size and Mass Flux in the Three-Dimensional Atomisation Region of Water Jet in Air-Cross Flow," *Exp. Fluids.*, 28, 29–35. doi: 10.1007/s003480050004
90. Feikema, D. A., R. Eskridge and J. J. Hutt (1997). "Structure of a Non Evaporating Swirl Injector Spray," *Atomization Sprays*. 7, 77–95.
91. Gal, P. L., N. Farrugia and D. A. Greenhalgh (1998). "Development of Laser Sheet Drop Sizing for Spray Characterization," *ILASS-Europe Proceedings*, 469–474.
92. Kawahara, N., D. Kasahara and M. Sumida (2004). "Liquid Sheet Break-up of High-Pressure Swirl Injector for DISI Engine," *Proceedings of the 6th International Symposium on Diagnostics and Modeling of Combustion in Internal Combustion Engines*, 303–310.
93. Takahasahi, F. and W. J. Shmoll (1995). "Characteristics of a Velocity- Modulated Pressure Swirl Atomizing Spray," *J. Propul Power.*, 11, 995–963.
94. Bayrel, L. and Z. Orzechowski (1993). "Liquid Atomization, Combustion: An International Series," Taylor and Francis, London.
95. Han, Z., S. Parrish, P. V. Farrell and R. D. Reitz (1997). "Modeling Atomization Processes of Pressure-Swirl Hollow-Cone Fuels Sprays," *Atomization Sprays.*, 7, 663–684.

96. Shraiber, A. A., A. M. Podvysotsky, V. V. Dubrovsky (1996). "Deformation and Breakup of Drops by Aerodynamic Forces," *Atomization Sprays*, 6, 667–692.
97. Squire, H.B. (1953). "Investigation of the stability of a moving liquid film," *Brit. J. Appl. Phys.* 4,167-169.
98. Ponstein, J. (1959). "Instability of rotating cylindrical jets," *Appl. Sci. Res.*, 8, 425-465.
99. Taylor, G.I. (1948). "The mechanics of swirl atomizers," 7th Int. Cong. Appl. Mech. 1, 280–285.
100. Levich, V. G. *Physicochemical Hydrodynamics*, Prentice Hall, 1962, pp 639– 646
101. Sterling, A. M. and C. A. Sleicher (1975). "Stability of Capillary Jets," *J. Fluid Mech.* 68, 477-495. doi:10.1017/S0022112075001772
102. Reitz, R.D. and F.V. Bracco (1986). "Mechanisms of Breakup of Round Liquid Jets," *The Encyclopedia of Fluid Mechanics*. 3, 223- 249.
103. Lefebvre, A. H. (1989). *Atomization and Sprays*, Hemisphere, New York.
104. Chung, I. P. and C. Presser (2001). "Fluid Property Effects on Sheet Disintegration of a Simplex Pressure-Swirl Atomizer," *J. Propul Power.*, 17, 212–216. doi: 10.2514/2.5730
105. Ramamurthi, K. and T. J. Tharakan (1998). "Flow Transition in Swirled Liquid Sheets," *AIAA Journal.*, 36, 420–427. doi: 10.2514/2.380
106. Liao, Y., A. T. Sakman, S. M. Jeng, M. A. Jog and M. A. Benjamin (1999). "A Comprehensive Model to Predict Simplex Atomizer Performance," *J. Eng Gas Turbines Power.*, 121, 285-294. doi:10.1115/1.2817119
107. Dombrowski, N. and D. Hassan, "The flow characteristics of swirl centrifugal spray pressure nozzles with low viscosity liquids," *AIChE J.* 15,404 (1969).
108. Chinn, J. J. (2008). "The numeric of the swirl atomizer," ILASS, Como Lake, Italy.
109. Dorfner, V., J. Domnick, F. Durst and R. Kohler (1995). "Viscosity and surface tension effects in pressure swirl atomization," *Atomization Sprays*, 5, 261–285.
110. Yao, S., J. Zhang and T. Fang (2012). "Effect of viscosities on structure and instability of sprays from a swirl atomizer," *Experimental Thermal and Fluid Science*, 39, 158-166.
111. York, J.L. H.F.Stubbs and M.R. Tek, The mechanism of disintegration of liquid sheets, *Trans. ASME*, Vol. 75,1953, pp. 1279-1286

112. Donjat, D., J. Estivalezes, M. Michau and G. Lavergne (2003). "Phenomenological study of the pressure swirl atomizer internal flow," Proceedings of the 9th ICLASS, Sorrento, Italy, 12–19.
113. Dombrowski, N., R. P. Fraser (1954). "A photographic investigation into the disintegration of liquid sheets," *Phil. Trans. Roy. Soc. London A*, 247(924), 101–130.
114. Fraser, R. P., P. Eisenklam, N. Dombrowski, and D. Hasson (1962). "Drop Formation from Rapidly Moving Liquid Sheets," *AIChE J.* 8(5), 672–680.
115. Taylor, G. (1959). "The dynamics of thin sheets of fluid. III. Disintegration of fluid sheets," *Proc. Roy. Soc. London A*, 253(1274), 313–321.
116. Han, Z., L. Fan, and R. D. Reitz (1997). "Multidimensional modeling of spray atomization and air-fuel mixing in a direct-injection spark-ignition engine," SAE Technical Paper 970884, Society of Automotive Engineers, Warrendale.
117. Schmidt, D. P., I. Nouar, P. K. Senecal, C. J. Rutland, J. K. Martin, R. D. Reitz and J. A. Hoffman (1999). "Pressure-Swirl Atomization in the Near Field," SAE Technical Paper 1999-01-0496, Society of Automotive Engineers, Warrendale.
118. Kim, S., D. Kim and D. Y. Yoon (2006). "Liquid film thickness measurement for swirl injector," *J. Korean Soc. Propuls. Eng.*, 10, 70–77.
119. Badami, M., V. Bevilacqua, F. Millo, M. Chiodi and M. Bargende (2004). "GDI swirl injector spray simulation: Combined phenomenological-CFD approach," SAE Paper, 2004-01-3005.
120. Rizk, N. K. and A.H. Lefebvre (1985). "Spray characteristics of simplex swirl atomizers," *Prog. Aeronaut. Astronaut*, 95, 563–580.
121. Reitz, R.D. (1978). Atomization and other breakup regimes of a liquid jet. Ph.D thesis, Princeton University.
122. Xu, J. J. and S. H. Davis (1985). "Instability of capillary jets with thermocapillarity," *J. Fluid Mech.*, 161, 1–26.
123. Dijkstra, H. A. and P. H. Steen (1991). "Thermocapillary stabilization of the capillary breakup of an annular film of liquid," *J. Fluid Mech.*, 229, 205–228.
124. Mashayek, F. and N. Ashgriz (1995). "Nonlinear instability of liquid jets with thermocapillarity," *J. Fluid Mech.*, 283, 97–123.
125. Fulnari, E. P. (2005). "Temporal instability of viscous liquid microjets with spatially varying surfacetension," *J. Phys. A: Math. Gen.*, 38, 263–276.